CARBON MOLECULAR SIEVE MEMBRANES FOR NITROGEN/METHANE SEPARATION

A Dissertation
Presented to
The Academic Faculty

by

Xue Ning

In Partial Fulfillment
of the Requirements for the Degree
Doctor of Philosophy in the
School of Chemical and Biomolecular Engineering

Georgia Institute of Technology
August 2014

CARBON MOLECULAR SIEVE MEMBRANES FOR NITROGEN/METHANE SEPARATION

Approved by:

Dr. William J. Koros, Advisor
School of Chemical & Biomolecular Engineering
Georgia Institute of Technology

Dr. Dennis Hess
School of Chemical & Biomolecular Engineering
Georgia Institute of Technology

Dr. Pradeep Agrawal
School of Chemical & Biomolecular Engineering
Georgia Institute of Technology

Dr. Krista Walton
School of Chemical & Biomolecular Engineering
Georgia Institute of Technology

Dr. Anselm Griffin
School of Materials Science & Engineering
Georgia Institute of Technology

Date Approved: April 16, 2014

ACKNOWLEDGEMENTS

My graduate school experience at Georgia Tech has been truly memorable. There are many people that have made my stay here exciting and meaningful. First and foremost, I would like to express my most sincere gratitude to my advisor Dr. William J. Koros for his continuous support, encouragement and guidance throughout my PhD study. His enthusiasm, unrivaled dedication and strong work ethic have been and will continue to be a great inspiration for me.

I would also like to thank my committee members, Dr. Dennis Hess, Dr. Pradeep Agrawal, Dr. Krista Walton, and Dr. Anselm Griffin for their constructive feedback and valuable inputs. The funding support from King Abdullah University of Science and Technology is also greatly appreciated.

All of my colleagues in the Koros Research Group, past and present, have been a great pleasure to work with. In particular, I would like to recognize Dr. J.R. Johnson, Dr. Oguz Karvan, Dr. Junqiang Liu, Dr. Mayumi Kiyono, Dr. Liren Xu and Dr. Mayumi Kiyono for teaching me valuable lessons around the lab. I would also like to thank Dr. Ying Labreche, Dr. Wulin Qiu, Dr. Chen Zhang, Dr. Nitesh Bhuwania, Dr. Carine Achoundong, Dr. Brian Kraftschik and Steven Burgess for the valuable discussions and technical communication during my research work.

I must also thank others who have played a critical role throughout my PhD experience. I am extremely grateful to my dearest parents for their unconditional love and support. My significant other, Jiaojun Jiang, has been my best friend and a constant source of happiness during the past few years. I feel so blessed to have him around. All

the friends I made in Atlanta have brought so much happiness to me. Thanks go out especially to Ying Labreche, Yang Cai, and Chen Zhang, who have stood by me through thick and thin.

TABLE OF CONTENTS

LIST OF TABLES

LIST OF FIGURES

SUMMARY

Membrane separation is an attractive alternative to traditional cryogenic distillation and pressure swing adsorption processes for nitrogen removal from natural gas. The main challenge to separate nitrogen and methane using membrane technology is the small size difference between the two gas molecules and the competing effect between diffusion and sorption, which lead to unattractive selecitivity in traditional polymer membrane materials. Carbon Molecular Sieve (CMS) membranes can overcome these problems by providing a hyper-rigid structure and distinctive bimodal pore size distribution. The nitrogen-selective CMS membranes developed in this work showed an attractive combination of permeability and selecitivity. As nitrogen permeates faster through the membrane, the majority of methane will be enriched in the high pressure retentate stream, significantly reducing the recompression cost.

Effects of pyrolysis conditions including pyrolysis temperature protocol and pyrolysis atmosphere were studied for Matrimid® and 6FDA:BPDA-DAM precursors. It was revealed that high pyrolysis temperature is essential to achieve attractive nitrogen/methane selectivity due to the subtle size difference between the two gas penetrants. Detailed study on one of the best performing CMS membranes showed that diffusion selection, more specifically, the entropic factor responsible for diffusion selection provides a significant contribution to the high selectivity. The effect of precursor was also studied by considering nine carefully selected polymers. The structures and properties of these polymer precursors were compared and correlated with the separation performance of resulting CMS membranes.

The translation of intrinsic CMS transport properties into the hollow fiber morphology was also explored. Substructure collapse and asymmetry lost during pyrolysis were observed, which resulted in significant increases of separation layer thickness and decreases in permeance. Vinyltrimethoxy silane (VTMS)-treatment was applied to polymer hollow fiber before pyrolysis to overcome the problem of substructure collapse. The effects of VTMS-treatment on both the substructure and skin layer are discussed.

CHAPTER 1

INTRODUCTION

1.1 Natural Gas Processing

The world total energy consumption is expected to grow by 56%, from 524 quadrillion BTU in the year 2010 to 820 quadrillion BTU by the year 2040 [1]. This rapid increase in energy demand is mostly due to the long-term economic growth in developing countries. Compared to other energy sources, natural gas will be the fastest-growing fossil fuel in the next several decades (Figure 1.1). It is estimated that world natural gas consumption will increase by 64%, from 113 trillion cubic feet in 2010 to 185 trillion cubic feet in 2040 [1]. Natural gas has lower carbon intensity than coal and oil, which makes it attractive under government policies that require reduction in greenhouse gas emissions. In addition, natural gas is attractive for new power plants because of its low capital cost and high thermal efficiency. With the depletion of easily accessible conventional natural gas reserves, a significant portion of future natural gas supplies will rely on the exploration of unconventional gas reserves – tight gas, shale gas, and coalbed methane (Figure 1.2) [1]. The development of these unconventional gas reserves, ensured by non-traditional production processes such as hydraulic fracturing and horizontal drilling, not only greatly expands the worldwide energy supply, but also provides other benefits. For example, the utilization of coalbed methane helps to improve coal mining safety and decrease the emission of methane, which is 20 times more potent as a greenhouse gas than carbon dioxide [2, 3].

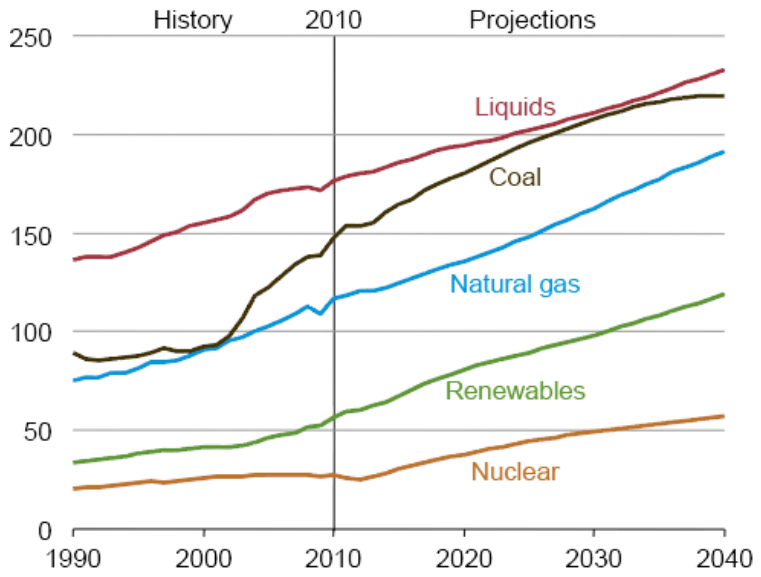

Figure 1.1: World energy consumption (in quadrillion BTU) by fuel type from 1990 to 2040 [1].

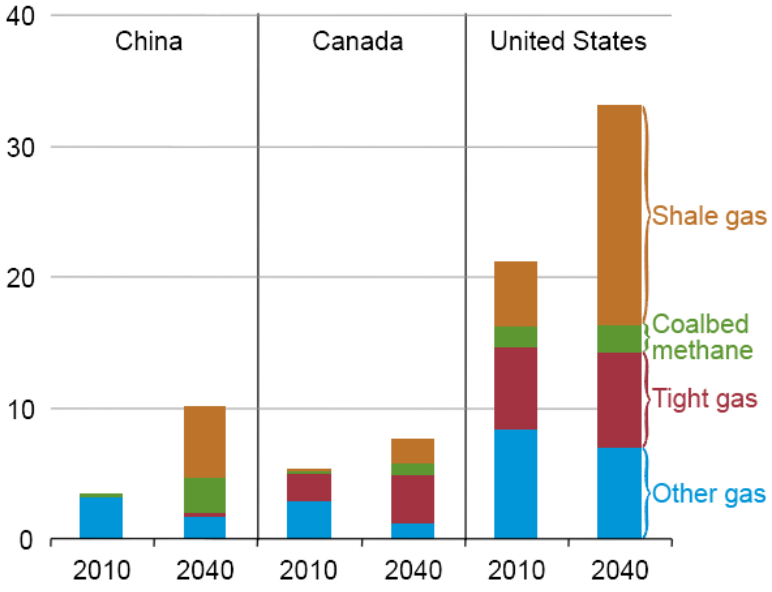

Figure 1.2: Natural gas production (in trillion cubic feet) in different geological locations in China, Canada, and the United State, 2010 and 2040 [1].

Apart from the main content methane (CH_4), impurities including carbon dioxide (CO_2), hydrogen sulfide (H_2S), nitrogen (N_2), water (H_2O), and heavier hydrocarbons (C_{2+}) are present in raw natural gas [4]. The composition of these contents varies significantly from site to site. However, the composition of gas delivered to commercial pipelines is strictly regulated. Typical natural gas pipeline specifications for the United States are shown in Table 1.1. According to the report of Gas Research Institute (currently Gas Technology Institute) in 1996, about 41% of proven raw reserves were subquality due to the high content of N_2 (>4%), CO_2 (>2%), and H_2S (>4 ppm) [5]. Thus, almost half of all natural gas requires upgrading process before transporting to end-users. A typical natural gas processing diagram is shown in Figure 1.3.

It was estimated in 2000 that 16% of the total proven reserves were highly contaminated by N_2 with composition from 5% to 40% [5, 6]. However, in recent years, enhanced gas recovery and nitrogen fracturing aggravate the nitrogen contamination in natural gas reserves. In such cases, N_2 is injected into gas reservoirs to increase pressure and fracture rock. Although the gas yield is largely improved, these processes can lead to nitrogen contamination as high as 50% [7]. While N_2 is inert and does not corrode pipelines like CO_2, H_2S and H_2O, the removal of N_2 is still important to ensure required heating value and reduce the costs of transportation and compression.

Table 1.1: Typical natural gas pipeline specifications in US [8].

Component	Specification
CO_2	< 2%
H_2S	< 4 ppm
H_2O	< 120 ppm
C_{3+}	950-1050 BTU/scf; Dew Point: -20 ˚C
Inert Gases (N_2, He)	< 4%

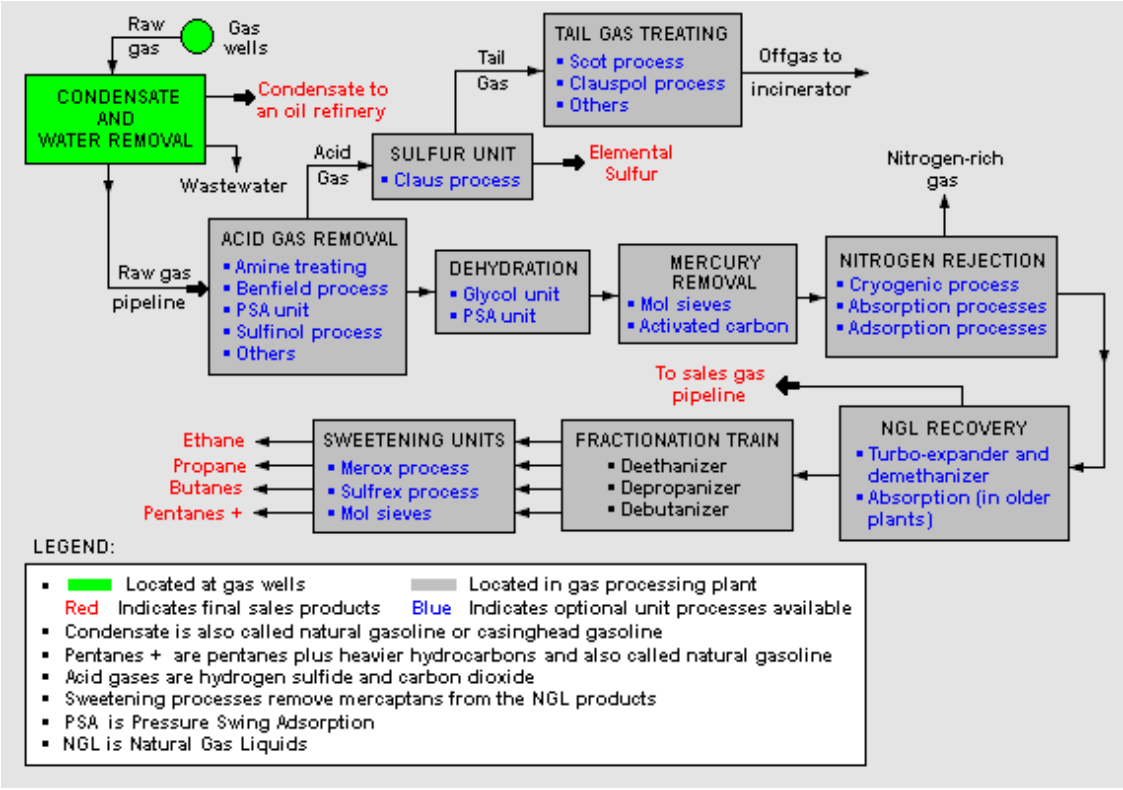

Figure 1.3: A schematic flow diagram of a typical large natural gas processing plant [9].

1.2 Overview of Nitrogen Rejection Technologies

Nitrogen removal from natural gas is a difficult and expensive process. It is estimated that nitrogen removal requires 7 to 10.8 times capital of carbon dioxide removal [10]. In many cases, nitrogen-contaminated natural gas reserves are untapped due to the lack of suitable nitrogen rejection technology [11]. Currently available nitrogen rejection technologies include cryogenic distillation, pressure swing adsorption, lean oil absorption, and membrane separation.

Cryogenic distillation is the only nitrogen rejection technology that has been used on a significant scale. The feed mixed gas stream is first liquefied by a series of heat exchangers and then flashed to vent a nitrogen-rich stream, leaving methane-rich stream. It can achieve the highest methane recovery at 98%. However, the complexity of pretreatment, high capital and energy intensity, and relative large footprint make it less attractive, especially for small and remote sites. To achieve economies of scale, cryogenic plants are usually on a large scale, with processing capacity above 75 MMscfd [11]. One example of cryogenic distillation technology for nitrogen rejection is Nitech™ developed by BCCK Engineering Inc [2].

Pressure swing adsorption (PSA) utilizes either nitrogen-selective or methane-selective adsorbents to adsorb nitrogen or methane under higher pressure [2, 12]. When the adsorbent bed is saturated, the pressure is reduced to desorb the adsorbed gas and thus the bed is ready for the next adsorption cycle. Porous materials including activated carbon, silica gel, alumina, and zeolite are selected as adsorbents for PSA systems. One example of PSA for nitrogen rejection is Molecular Gate® developed by Engelhard Co.

The adsorbent used in this technology is molecular sieve ETS-4, the pore opening of which can be adjusted at 0.1 Å intervals by irreversible dehydration. When the pore opening is controlled at 3.7 Å, N_2 can be selectively adsorbed while CH_4 is excluded [2, 13]. PSA processes are better suited for throughputs less than 10 MMscfd [14, 15]. However, the capital and operating costs of these systems are relatively high due to the multiple beds and complicated switching controls between beds [11].

In lean oil absorption, feed raw gas stream is fed concurrently with cold liquid hydrocarbons which selectively absorb methane, leaving nitrogen unabsorbed. Then the methane rich stream is flashed at lower pressure to release methane and the lean solvent is ready for the next cycle [2]. Similar to PSA, lean oil absorption is more suited to small throughputs and is relatively capital intensive [11].

Membrane separation for nitrogen rejection is achieved by using a membrane material that can selectively pass either N_2 or CH_4. Rubbery polymer membrane has flexible polymer chains which cannot effectively distinguish the size difference between N_2 and CH_4. As a result, the more condensable CH_4 permeates faster under the sorption selection effect. Although the CH_4-selective membrane can provide relatively high flux, the CH_4/N_2 selectivity is limited at 2~4 at ambient temperature [11]. One example of a commercial CH_4-selective membrane separation technology is the NitroSep^{TM} process developed by MTR, Inc. This process uses either single-stage or two-stage membrane unit to enrich CH_4. As the CH_4-enriched permeate stream loses the high pressure from wellhead, recompression process is required after the membrane unit. The CH_4-selective membrane separation is better suited for low N_2 feed streams. It can achieve 90% CH_4 recovery when the nitrogen composition in feed stream is lower than 12%. If N_2 is more

than 30% in feed stream, this process is not economically feasible to produce pipeline quality gas [7]. Although N_2-selective membranes have been reported in literature, this type of membrane has not been commercially developed. The N_2-selective membranes utilize the relatively rigid structure in glassy polymers or molecular sieves to provide dominating diffusion selection effect over sorption effect. While the smaller N_2 diffuses faster into the permeate stream, CH_4 can be enriched in the retentate stream which keeps the high pressure from wellhead.

1.3 Overview of Membrane Technology for Gas Separation

Membranes can separate mixed gas feed stream into a fast gas-enriched permeate stream and a slow-gas enriched retentate stream. It is an attractive alternative to traditional gas separating processes by virtue of its high adaptability, high reliability, low energy consumption, small footprint, low weight, reduced adverse environmental impact, and low capital cost in installation, operation and maintenance. In many cases, it can utilize the high wellhead pressure as a "free driving force" to perform the separation. Membrane units are modular and usually skid-mounted, making it especially attractive for small and remote sites.

Since the first H_2-separating membrane Prism® was commercialized in 1980, membrane gas separation has grown to be an attractive technology in many industrial applications, including air separation, hydrogen separation, natural gas treatment, and petrochemical areas. Figure 1.4 shows the predicted growth of membrane market in different applications between the years 2000 and 2020.

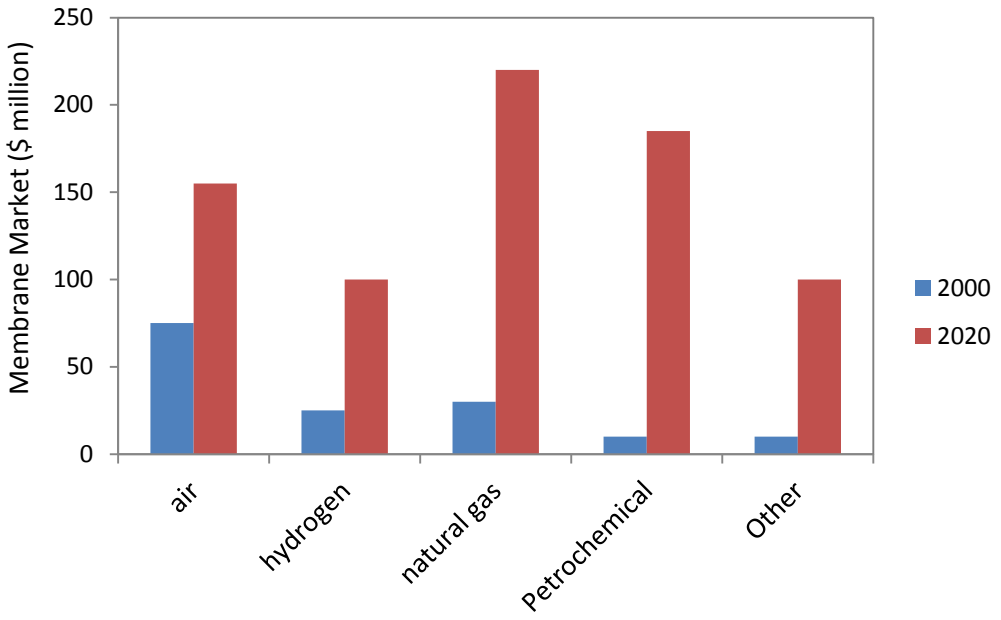

Figure 1.4: Breakdown of market for membrane-based gas separations in the years 2000 and 2020 (shown in $ million, 2000 dollars) [16].

Four key elements are identified for the advancement of membrane technology: (1) the development of high-efficiency modules with high separation area/volume ratio, (2) the creation of advanced materials with high separation performance, (3) the development of capability to control micro-morphology within a membrane cross-section, and (4) the development of manufacturing methods to link the above three factors into economical and defect-free devices [17].

Most researchers have been focused on the creation of advanced materials, especially for the less investigated separations. The study of advanced materials is the first key step to enable a new membrane separation application. In commercial modules, polymer is the dominant membrane material, which can be processed into different morphologies, including plate in frame, spiral wound, and hollow fiber. Asymmetric

hollow fibers are tubular with a thin separation layer on the shell side and a highly porous supporting substructure comprising the majority of the fiber wall on the bore side. It is the most promising morphology since it can provide high flux and high separation area to module volume ratio.

Conventional polymeric membranes are limited by a trade-off effect between the productivity (permeability) and efficiency (selectivity) – selectivity usually decreases as permeability increases, and vice versa [18]. The polymeric membrane upper bound of permeability vs. selectivity for N_2/CH_4 cannot provide efficient separation for this gas pair. In addition, polymeric membrane's stability at high temperature and under aggressive and highly condensable hydrocarbon feeds can be an issue. High polar or condensable gases such as CO_2 can swell (plasticize) polymer chains, resulting in radical increase in the flux of all gas penetrants and a corresponding selectivity loss. While this is not a major issue for N_2 removal from natural gas, it is still a concern for raw gases with coexisting high content of N_2, CO_2, and H_2S.

Molecular sieving inorganic materials like zeolite, metal-organic frameworks, and carbon molecular sieve membranes with rigid and more precisely-controlled pore structures have shown potential to overcome the polymeric upper-bound of permeability vs. selectivity. The pore structure in these materials can more effectively distinguish the subtle differences in the size and shape of gas penetrants. However, all these relatively new membrane materials face challenges in the fabrication process.

1.4 Membrane Development Strategy for N_2/CH_4 Separation

Compared to other major gas pairs, N_2/CH_4 membrane separation is a relatively difficult process which has not been extensively investigated. The competing effect between diffusion and sorption terms poses a challenge for this gas pair. Diffusion selectivity comes from the ability of membrane material to function as size and shape selective media for the gas penetrants. Larger differences in the size and shape of the two gas components lead to higher diffusion selectivity. Also, narrow-distributed transient gaps or fixed ultramicropores of a membrane material centered between the sizes of two gas molecules will largely increase the diffusion selectivity. Kinetic diameters of N_2 and CH_4 are 3.64 Å and 3.80 Å, respectively. With this small size difference, diffusion selectivity slightly favors N_2 to permeate faster through the membrane. In the absence of groups in the membrane that chemically attract gas molecules, the sorption selectivity is determined largely by condensability of gas penetrants. Condensability is well reflected by critical temperature – the higher critical temperature, the higher condensability. The critical temperatures for N_2 and CH_4 are 126 K and 191 K, respectively. Clearly, CH_4 is more condensable than N_2. Without certain groups that can strongly interact with N_2, sorption favors CH_4 to permeate faster through the membrane. For various polymers, the sorption selectivity of N_2 vs. CH_4 is usually within the range of 0.2-0.4 [19]. These properties make N_2 permeate faster than CH_4 in membranes with stronger diffusion selection abilities, while CH_4 permeates faster in membranes with stronger sorption selection effect.

Most rubbery polymeric membranes are slightly CH_4-selective, since the broad distribution of segmental motions and transient intersegmental gap sizes provide very small N_2/CH_4 diffusion selectivity; therefore CH_4/N_2 solubility selectivity dominates permselectivity. The highest CH_4/N_2 permselectivity of CH_4-selective membranes has been achieved around 3~4 at ambient temperature [7]. Although the flux is high for this membrane system, the loss of high well-head pressure of the permeate stream imposes an additional cost for recompression.

In 1987, Kim and Koros et al. identified polyimides with "reverse selectivity", i.e., N_2 permeates preferentially rather than CH_4 [19]. For glassy polymers, limited mobility of polymer segments leads to a relatively narrow distribution of effective transient intersegmental gap sizes and better distinguishability of gas molecule size. Thus diffusion selectivity can dominate permselectivity and N_2 permeates faster through the membrane. This kind of membrane is called N_2-selective. With CH_4 rejected to the high pressure retentate stream, the advantage of saving recompression cost is significant. Unfortunately, the best performing N_2-selective glassy polymer membranes with acceptable N_2 permeability only provide a N_2/CH_4 permselectivity ~3, which is marginal for economical separations.

Robeson identified that the best combinations of permeability and selectivity of polymer membranes follow a relationship expressed by $P_A = k\alpha_{A/B}^n$ [18]. This relationship is shown as a linear upper bound line in the log-log plot of selectivity vs. fast gas permeability for each gas pair. Membrane materials approaching or over passing the upper bound line are considered to be superior. The upper bound correlation of polymer materials for N_2/CH_4 is shown in Figure 1.5.

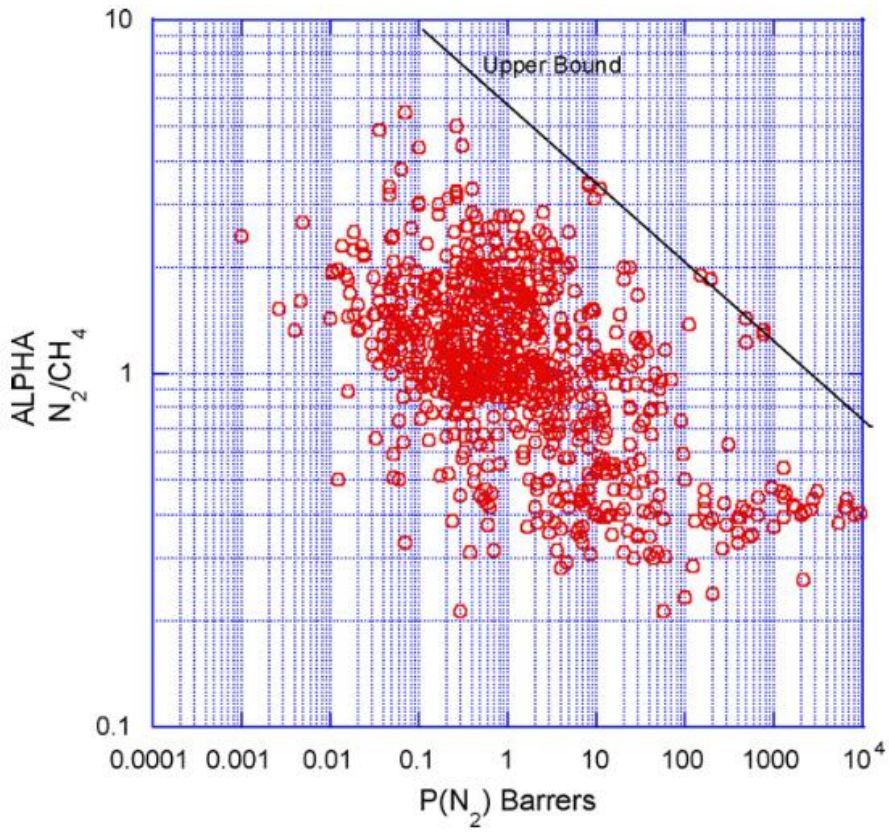

Figure 1.5: Upper bound correlation for N_2/CH_4 separation using polymeric gas separation membranes [18].

Due to the recompression cost consideration, this study focuses on the N_2-selective membranes. Since the permeation of gas penetrants through membrane is composed of two processes – the sorption and the diffusion, improving either the diffusion selectivity or sorption selectivity would help to enhance the overall permselectivity.

The physical sorption of N_2 in membrane material can be hardly improved due to the limited condensability of N_2. Thus chemical compounds that can chemically attract N_2 need to be used to improve the N_2/CH_4 sorption selectivity. It has been shown that

iron-phosphine complex dissolved in polar solvent can reversibly bind N_2 to improve the liquid absorption of N_2 [20, 21]. However, initial study of applying such compound into polymer matrix showed problems of instability of the iron-phosphine. Without solvent, this metal-organic compound quickly decomposed and changed color at ambient environment. The incorporation of this compound into polymer matrix was also found difficult due to the incompatibility between the two materials. More details of applying metal organic complex into polymer membrane will be presented in Appendix A.

The other way to improve N_2/CH_4 permselectivity is to enhance the diffusion selectivity, which requires the use of rigid membrane structure with appropriate pore size and shape. Zeolite, metal-organic framework (MOF), and carbon molecular sieves have potentials to effectively discriminate the subtle size and shape differences between N_2 and CH_4. In the case of zeolite/polymer mixed-matrix membrane, the interface morphology between the inorganic zeolite and organic polymer is complicated to control, resulting in difficulties to obtain expected performance [22]. MOF has shown good compatibility with polymers [23]. However, the flexible pore structure in MOF cannot provide sufficient diffusion selection effect for the small size difference between N_2 and CH_4. The N_2/CH_4 permselectivity of MOF/polymer mixed matrix membranes is shown to be below 3 according to current literature [24-28].

Carbon molecular sieve (CMS) membranes have shown superior separation performance based on its bimodal distribution of pore sizes – ultramicropores offer high selectivity by molecular sieving mechanism and micropores offer high permeability by providing sorption cavities and promoting larger average diffusional jumps [29]. Attractive separation performance has been achieved by CMS membranes for several gas

pairs, including O_2/N_2, CO_2/CH_4, C_2H_4/C_2H_6 and C_3H_6/C_3H_8 [30-33]. CMS membranes are also proved to be thermally stable and do not exhibit compaction or swelling problems at high pressures up to 1000 psi [29, 34, 35]. With these merits, CMS membranes show high potential in N_2-selective N_2/CH_4 separation.

However, only a few researchers have reported N_2/CH_4 permeation data of CMS membranes [36-41], and most of them did not focus on N_2/CH_4 separation, but rather on O_2/N_2 and CO_2/CH_4 separation. The reported data for these CMS membranes showed N_2/CH_4 permselectivity in the range of 1 to 4 but two cases had higher permselectivity. Steel et al. prepared Matrimid® derived CMS membrane at 800 ℃ under vacuum and achieved N_2/CH_4 permselectivity of 5.89 with N_2 permeability of 1.86 Barrers [37]. Hosseini et al. fabricated CMS membrane pyrolyzed from PBI/Matrimid® (25/75 wt.%) blend polymers (vacuum, 800 ℃) and achieved N_2/CH_4 permselectivity of 7.99 with N_2 permeability of 3.78 Barrers [41].

1.5 Research Objectives

This research focuses on developing CMS membranes for N_2/CH_4 separation and the principles to guide the development of high-performing CMS membranes for such 'size-similar' gas pair. The objectives of this dissertation are as follows:

1. Analyze the effects of pyrolysis conditions to achieve high-performing CMS membranes for N_2/CH_4 separation.

Carbon molecular sieve (CMS) membranes are pyrolyzed from polymer precursors under controlled condition. The pore structure of CMS may be tailored to obtain desired properties for specific separations by controlling several parameters during the pyrolysis process. In this study, the effects of heating protocol and pyrolysis atmosphere on the separation performance were investigated for three precursors, Matrimid® 5218, 6FDA:BPDA-DAM, and 6FDA-DAM. The best performing 800 ℃ pyrolyzed Matrimid® CMS membrane was studied in more details to interpret the strong molecular sieving effect. The temperature effect on CMS transport was studied at temperatures between 25-50 ˚C. The deconvolution of sorption and diffusion terms from permeation, and the deconvolution of energetic and entropic factors from diffusion selectivity explained the basis for the superior performance of CMS membranes vs. polymeric membranes. The application of transition state theory elucidated the highly effective size and shape selection effect provided by the 'slit-shaped' pore structure in CMS membranes.

2. Analyze different polymers as precursors to CMS dense film membranes for N_2/CH_4 separation

The intrinsic properties of polymer precursors can significantly affect the separating performance of CMS membranes. Several polymer precursors were pyrolyzed under the same pyrolysis condition, and resulting CMS dense films were tested for

transport properties. The correlation between several polymer properties and resulting CMS membrane performance was analyzed. Hypotheses regarding precursor selection for N_2/CH_4 separation were developed.

3. Extend the high performance obtained from CMS dense films to CMS hollow fiber morphology for N_2/CH_4 separation.

Asymmetric hollow fiber is the most desirable morphology for real applications due to its high flux, compact and robust nature. However, there are significant challenges to transform high-performing CMS dense films to CMS hollow fibers. One of the issues is to maintain the asymmetric cross-sectional structure after pyrolysis. As polymer precursors go through their glassy transition temperature during pyrolysis, the porous supporting structure in the fiber might densify to increase the thickness of separation layer, resulting in reduced flux. Not being a primary objective, several efforts were made to address this problem.

1.6 Dissertation Organization

Following this introductory chapter, there are six additional chapters. Chapter 2 provides an overview of essential theory and background to facilitate understanding of the work in this dissertation. Chapter 3 describes the materials, experimental procedures, equipment and characterization techniques used throughout this research. Chapter 4-6 form the main chapters of this thesis to present and discuss the results of this work,

corresponding to the three research objectives described in the previous section. Chapter 7 summarizes the major findings contained within this dissertation and presents recommendations for future work in this field. Finally, appendices are provided for supplemental information.

1.7 References

[1] International energy outlook 2013. Washington, D.C.: Energy Information Administration, 2013 DOE/EIA-0484(2013).

[2] Upgrading drained coal mine methane to pipeline quality: A report on the commercial status of system suppliers. United States Environmental Protection Agency, 2008 EPA-430-R08-004.

[3] Coalbed methane: Principles and practices. Halliburton, 2008.

[4] Alvarado DB, Asaro MF, Bomben JL, Damle AS, Bhown AS. Nitrogen removal from low quality natural gas. SRI International, 1997.

[5] Meyer H. Volume and distribution of subquality natural gas in the united states. GasTIPS (February 2000) 2000.

[6] Tannehill CC. Nitrogen removal requirements from natural gas. Gas Research Institute, 1999.

[7] Jariwala A, Lokhandwala KA. Nitrogen-rejecting membranes to increase gas heating value and recover pipeline natural gas: A simple wellhead process approach. 12th Annual International Petroleum Environmental Conference. Houston, TX2005.

[8] Baker RW, Lokhandwala K. Natural gas processing with membranes: An overview. Ind Eng Chem Res 2008;47(7):2109-21.

[9] Beychok M. Natural gas processing2011. Available from: http://www.eoearth.org/view/article/170032/.

[10] Technical and economic assessment of potential to upgrade gob gas to pipeline quality. United States Environmental Protection Agency, Radiation Aa; 1997 December. Report No.: Contract No.: 430-R-97-012.

[11] Lokhandwala KA, Ringer M, Wijmans H, Baker RW. Nitrogen removal from natural gas using membranes. Membrane Technology and Research, Inc., 1996.

[12] Changela M, Mckee R, Heshan H, Pathak V, Quinlan M, Strickland J. Evaluation of natural gas process technology. LW August 1996;7.

[13] Kuznicki SM, Bell VA, Nair S, Hillhouse HW, Jacubinas RM, Braunbarth CM, et al. A titanosilicate molecular sieve with adjustable pores for size-selective adsorption of molecules. Nature 2001;412(6848):720-4.

[14] Kaaeid A. Lokhandwala MR, Hans Wijmans, Richard W. Baker,. Nitrogen removal from natural gas using membranes. Membrane Technology and Research, Inc.

[15] Mitariten M. Molecular gate® adsorption system for the removal of carbon dioxide and / or nitrogen from coalbed and coal mine methane. Western States Coal Mine Methane Recovery and Use Workshop: Guild Associates, Inc., 2005.

[16] Baker RW. Future directions of membrane gas separation technology. Ind Eng Chem Res 2002;41(6):1393-411.

[17] Koros WJ. Evolving beyond the thermal age of separation processes: Membranes can lead the way. AIChE J 2004;50(10):2326-34.

[18] Robeson LM. The upper bound revisited. J Membr Sci 2008;320(1-2):390-400.

[19] Kim TH, Koros WJ, Husk GR, O'brien KC. "Reverse permselectivity" of n2 over ch4 in aromatic polyimides. J Appl Polym Sci 1987;34(4):1767-71.

[20] Friesen DT, Babcock WC, Edlund DJ, Lyon DK, Miller WK, inventors; Liquid absorbent solutions for separating nitrogen from natural gas patent US 6,077,457. 2000.

[21] Friesen DT, Babcock WC, Edlund DJ, Miller WK, inventors; Nitrogen sorption patent US 5,225,174. 1993.

[22] Chung T-S, Jiang LY, Li Y, Kulprathipanja S. Mixed matrix membranes (mmms) comprising organic polymers with dispersed inorganic fillers for gas separation. Prog Polym Sci 2007;32(4):483-507.

[23] Zhang C, Dai Y, Johnson JR, Karvan O, Koros WJ. High performance zif-8/6fda-dam mixed matrix membrane for propylene/propane separations. J Membr Sci 2012;389:34-42.

[24] Basu S, Cano-Odena A, Vankelecom IFJ. Asymmetric matrimid®/[cu3(btc)2] mixed-matrix membranes for gas separations. J Membr Sci 2010;362(1–2):478-87.

[25] Keskin S, Sholl DS. Assessment of a metal− organic framework membrane for gas separations using atomically detailed calculations: Co2, ch4, n2, h2 mixtures in mof-5. Ind Eng Chem Res 2008;48(2):914-22.

[26] Ordoñez MJC, Balkus Jr KJ, Ferraris JP, Musselman IH. Molecular sieving realized with zif-8/matrimid® mixed-matrix membranes. J Membr Sci 2010;361(1–2):28-37.

[27] Zhang Y, Musselman IH, Ferraris JP, Balkus Jr KJ. Gas permeability properties of matrimid® membranes containing the metal-organic framework cu–bpy–hfs. J Membr Sci 2008;313(1–2):170-81.

[28] Adams R, Carson C, Ward J, Tannenbaum R, Koros W. Metal organic framework mixed matrix membranes for gas separations. Microporous Mesoporous Mater 2010;131(1–3):13-20.

[29] Vu DQ, Koros WJ, Miller SJ. High pressure co2/ch4 separation using carbon molecular sieve hollow fiber membranes. Ind Eng Chem Res 2002;41(3):367-80.

[30] Steel KM, Koros WJ. Investigation of porosity of carbon materials and related effects on gas separation properties. Carbon 2003;41(2):253-66.

[31] Kiyono M, Williams PJ, Koros WJ. Effect of pyrolysis atmosphere on separation performance of carbon molecular sieve membranes. J Membr Sci 2010;359(1–2):2-10.

[32] Saufi SM, Ismail AF. Fabrication of carbon membranes for gas separation—a review. Carbon 2004;42(2):241-59.

[33] Rungta M, Xu L, Koros WJ. Carbon molecular sieve dense film membranes derived from matrimid® for ethylene/ethane separation. Carbon 2012;50(4):1488-502.

[34] Xu L, Rungta M, Brayden MK, Martinez MV, Stears BA, Barbay GA, et al. Olefins-selective asymmetric carbon molecular sieve hollow fiber membranes for hybrid membrane-distillation processes for olefin/paraffin separations. J Membr Sci;423-424(15):314-23.

[35] Ismail AF, David L. A review on the latest development of carbon membranes for gas separation. J Membr Sci 2001;193(1):1-18.

[36] Lie JA, Hägg M-B. Carbon membranes from cellulose: Synthesis, performance and regeneration. J Membr Sci 2006;284(1–2):79-86.

[37] Steel KM, Koros WJ. An investigation of the effects of pyrolysis parameters on gas separation properties of carbon materials. Carbon 2005;43(9):1843-56.

[38] Zhou J, Jin J, Haldeman AT, Wagener EH, Husson SM. Formation and characterization of perfluorocyclobutyl polymer thin films. J Appl Polym Sci 2013;129(6):3226-36.

[39] Yoshimune M, Haraya K. Flexible carbon hollow fiber membranes derived from sulfonated poly(phenylene oxide). Sep Purif Technol 2010;75(2):193-7.

[40] Tin PS, Chung T-S. Novel approach to fabricate carbon molecular-sieve membranes based on consideration of interpenetrating networks. Macromol Rapid Commun 2004;25(13):1247-50.

[41] Hosseini SS, Chung TS. Carbon membranes from blends of pbi and polyimides for n2/ch4 and co2/ch4 separation and hydrogen purification. J Membr Sci 2009;328(1–2):174-85.

CHAPTER 2

THEORY AND BACKGROUND

2.1 Overview

This chapter provides essential theory and background information relevant to the focus of this dissertation. Section 2.2 gives a brief background of the structure of carbon molecular sieve (CMS) membranes. Section 2.3 gives a review of the formation of CMS membranes and factors in the membrane fabrication process that affect transport properties. Finally, Section 2.4 provides fundamental gas transport theory of permeation, sorption and diffusion in polymeric and CMS membranes.

2.2 Structure of Carbon Molecular Sieve Membranes

When polymers are heated in an inert atmosphere, carbonization takes place and results in evolved small molecules and a residual material of coke or char [1]. If the polymer precursor goes through a liquid state during pyrolysis, the chains will collapse to form aromatic lamellae stacking above each other and result in crystalline anisotropic coke. If the polymer precursor does not go through a liquid state during pyrolysis, non-graphitizable "hard" char will form [1, 2].

Coke can be converted to graphite at temperatures between 2500 to 3000 ℃. Graphite consists of graphene sheets stacked in a hexagonal ABA sequence as shown in

Figure 2.1 [1]. The distance between two neighboring carbon atoms within the sheet is 1.42 Å, and the interlayer spacing between graphene sheets is 3.354 Å [1, 2]. The C-C bonding within the layer is sp^2-hybridezed – each carbon is bonded with 3 other carbon atoms by σ bond, and delocalized π bond exist within the layers. There is no chemical bond between graphene layers, as they are connected by van der Waals force. The density of graphite is ~2.25 g/cm^3 at 300K [2].

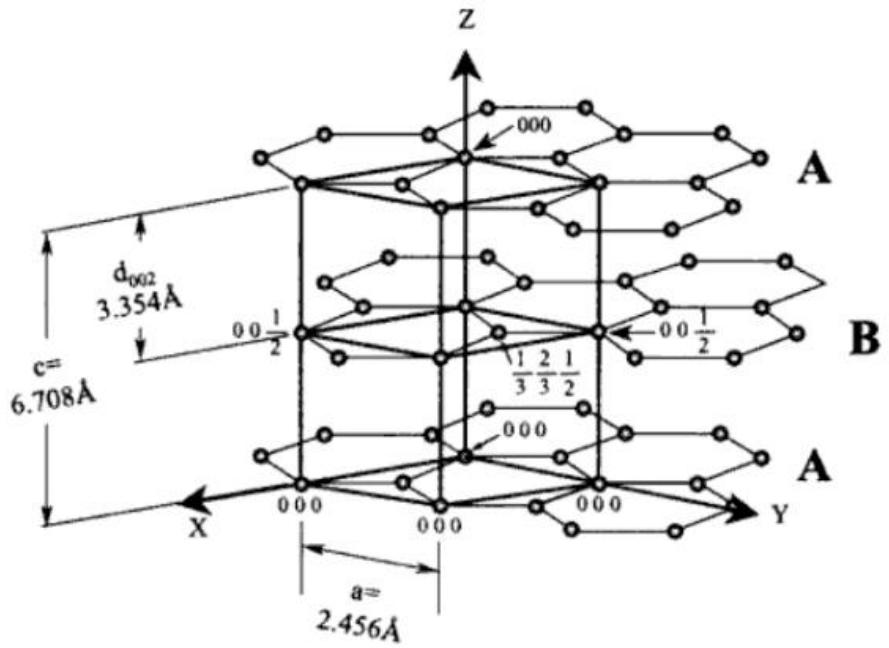

Figure 2.1: Atomic structure of a perfect graphite crystal with ABA stacking [2].

Char is not graphitizable and remains an amorphous structure [2]. During the carbonization process, linear conjugated carbon-carbon systems are first formed with the release of oxygen, nitrogen, halogen, etc. Then with the elimination of hydrogen, highly aromatic structures comprised of disordered sp^2-hybridized carbon sheets are formed [1, 2].

CMS membranes are derived from pyrolysis of polymer membrane precursors under vacuum or inert gas purge. During pyrolysis, scission and reorganization of polymer chains occur, with small gas molecules released and free radicals formed. The free radicals then form interchain or intrachain crosslinking, giving rise to conjugated aromatic 3-D network with graphene-like structure [1-3]. As the pyrolysis temperature increases, sp^2-hybridized carbon sheets begin to align somewhat parallel to each other forming ordered structures on a short range, shown as Figure 2.2(a). On the long range, these carbon sheets show turbostratic structure with little order and are essentially considered isotropic or amorphous, shown as Figure 2.2(b) [4]. The overall structure consists of aromatic sheets and strips, resembling a mixture of wood shavings or crumpled paper as shown in Figure 2.2(c) [5].

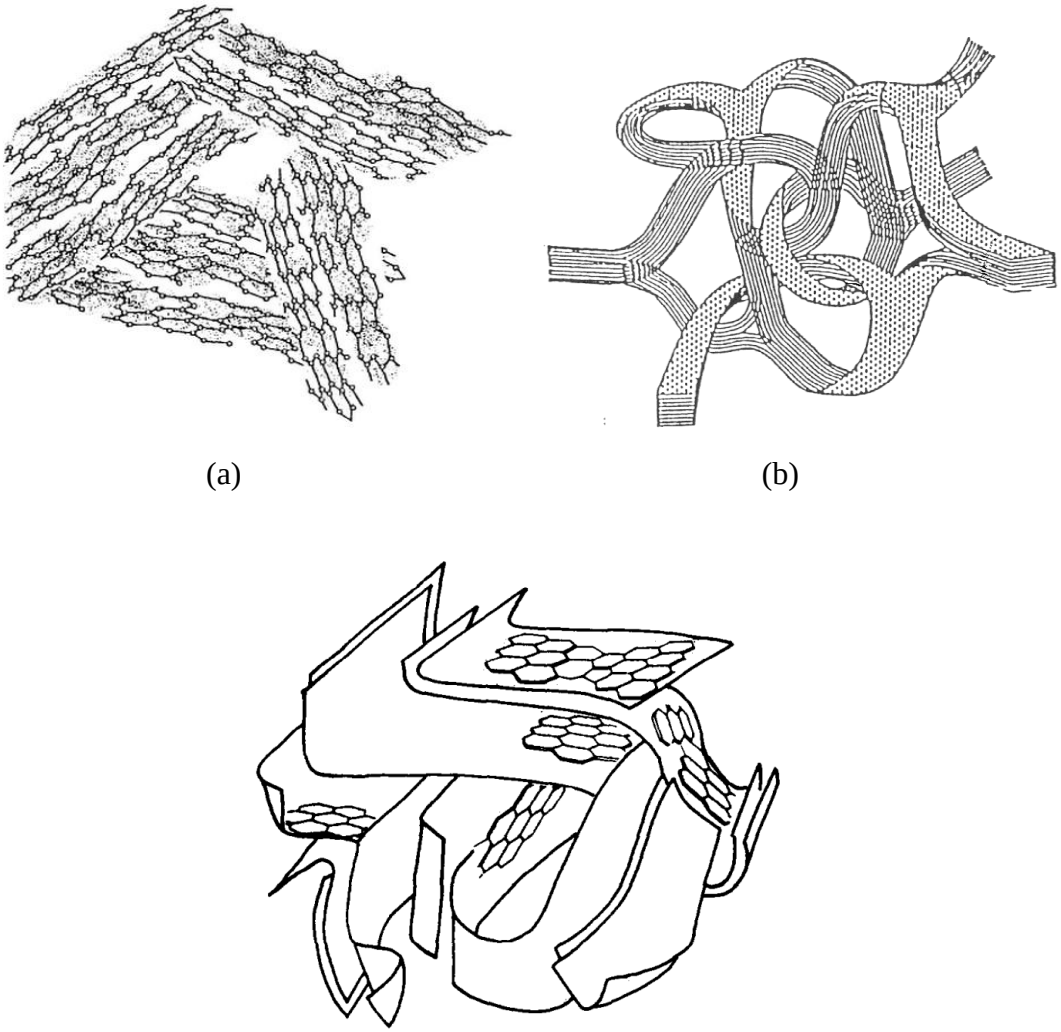

(a) (b)

(c)

Figure 2.2: Structure of CMS membranes (a) sp^2-hybridized carbon sheets on short range [2], (b) turbostratic structure on long range [1], and (c) overall structure [5].

"Slit-like" pore structures are formed from packing imperfections between ordered regions. A bimodal pore distribution is used to describe CMS structures – "micropores" with size of 7 to 20 Å connected by molecular-sieving "ultramicropores" with size below 7 Å, illustrated in Figure 2.3 [4].

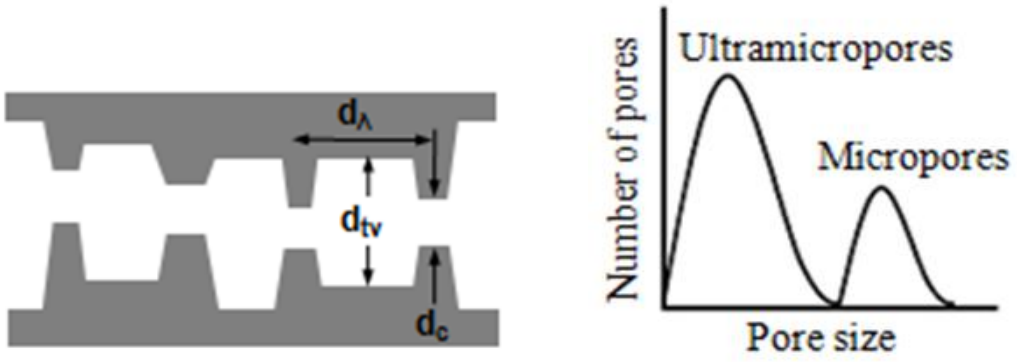

Figure 2.3: Pore structure in CMS membranes (a) idealized pore structure of CMS membranes, and (b) idealized bimodal pore size distribution of CMS membranes [4]. In (a), the notations correspond to d_c: ultramicropore dimension, d_{tv}: size of adsorptive pore dimension, and d_λ: jump length dimension.

The combination of micropores and ultramicropores is believed to provide high permeability and high selectivity at the same time – the micropores offer high permeability by providing sorption cavities and promoting larger average diffusional jumps, and the ultramicropores offer high selectivity by molecular sieving mechanism.

2.3 Formation of Carbon Molecular Sieve Membranes

As mentioned in the above section, carbon molecular sieve (CMS) membranes are formed by pyrolyzing polymer precursors under vacuum or inert gas. The initial step of pyrolysis at temperature between 300 and 500 ℃ involves bond cleavage, hydrogen transfer and formation of free radicals, followed by intramolecular coupling and

intermolecular cross-linking of the generated radicals [6-8]. The result is a loose network of conjugated system with increased permeability. Around 500 ℃, dehydrogenation starts and aliphatic carbon is converted to aromatic carbon, resulting in higher C:H ratio [1, 7, 9]. Separate conjugated systems become interconnected to form disordered carbon lamellae. The density, hardness, stiffness and conductivity are increased and the permeability is decreased in this process [1]. At the same time, small molecules of water, methane, carbon dioxide, carbon monoxide, hydrogen, etc. are released and microporosity within the rigid macromolecular system is generated [7, 9].

The carbonization of polymer is a complicated process and varies with different precursors and pyrolysis conditions. Several key parameters control the pore size distribution and the separation performance of resulting CMS membranes. The influences of polymer precursor, pre-treatment, heating protocol and pyrolysis atmosphere are reviewed and presented below.

2.3.1 Polymer Precursor

Polymer precursors for CMS membrane fabrication should maintain their macroscopic morphology after pyrolysis. A variety of polymers have been used to fabricate CMS membranes, including phenolic resins [10-12], polyimides [4, 13-19], cellulose derivative [20, 21], poly(furfuryl alcohol) [22, 23], and vinylidene chloride copolymers [24]. Among these, polyimides show outstanding properties as a precursor. They exhibit high glass transition temperatures, good processability, good mechanical strength, high carbon yields, and low shrinkage [14, 15, 25, 26].

The correlation between polymer precursor structure and CMS membrane microstructure and properties has attracted the interest of many researchers in this field. Several studies have been performed to interpret the guiding relationship. In these studies, usually different polymers were pyrolyzed with the same pyrolysis condition, and the separation properties of resulting CMS membranes are compared.

Fractional free volume (FFV), glass transition temperature, chemical structure, chain structure and mobility can all affect the CMS membrane separation properties. Williams compared CMS membranes derived from two isomeric precursors – 6FDA-6FpDA and 6FDA-6FmDA. This study showed that the isomer 6FDA-6FpDA with higher FFV resulted in CMS membrane with higher permeability [27]. Park et al. have also shown that the introduction of methyl groups can increase the FFV of polymer precursor and lead to higher permeability of resulting CMS membranes [28].

Steel and Koros compared CMS membranes produced from polyimides Matrimid® and 6FDA:BPDA-DAM, and found Matrimid®-derived CMS membranes showed lower permeabilities but higher selectivities for a series of gas pairs. This result is not only due to the lower FFV of Matrimid®, but is also believed to be largely due to the presence of bulky CF_3 groups in 6FDA:BPDA-DAM. The evolvement of fluorinated compounds such as CHF_3 and trace HF can lead to higher microporosity and permeability in CMS membranes [4].

For hollow fiber CMS membranes, the properties of polymer precursor not only affect the intrinsic separation performance in the skin layer, but also the CMS hollow fiber substructure morphology and permeance. Recent study by Xu has shown that

precursors with higher glass transition temperature can reduce the level of densification of the porous supporting layer in hollow fiber during pyrolysis, resulting in higher permeance [29].

These studies indicate that choosing an appropriate starting material is critical to fabricate CMS membranes for particular gas separations. In the current study, a series of polymers have been chosen to analyze the influence of precursor on separation properties, which will be discussed and presented in Chapter 5.

2.3.2 Pre-treatment of Polymer Precursor

Different pre-treatments of polymer precursors prior to pyrolysis have been used to change chain packing, alter chain segmental mobility, and preserve membrane micro-morphology. Thermal stabilization and pre-oxidation of polymer precursors is a commonly used method to enhance the structure stability and uniformity of pore formation during pyrolysis [26].

Tin et al. used methanol, ethanol, propanol and butanol to soak polymer precursors before pyrolysis to weaken intermolecular interactions and allow structure reorganization of carbon chains. This method helped to reduce the pore size in CMS membranes and increase selectivity [30]. Centeno and Fuertes have shown that oxidative pre-treatment in air at 200 ℃ can also improve the selectivity of CMS membranes derived from poly(vinylidene chloride-co-vinyl chloride) [31].

Xiao et al. brominated Matrimid® to increase the chain rigidity, FFV and glass transition temperature of precursor. The results showed this method can improve permeability while maintain a competitive selectivity [32].

Thermal stabilization has been proved to be able to stabilize hollow fibers from softening and collapse and maintain the asymmetric cross-sectional structure during pyrolysis [33, 34]. Recently, a new method to prevent the collapse in CMS hollow fiber substructure was developed by a sol-gel reaction of organic-alkoxy silane and moisture on Matrimid® and 6FDA:BPDA-DAM. Results showed this treatment before pyrolysis can significantly improve the CMS hollow fiber permeance while maintaining a relative high selectivity [35].

In this study, the pre-treatment of dense film polymer precursor was not explored. However, the sol-gel reaction of organic-alkoxy silane and moisture was applied on hollow fiber to address the substructure collapse problem in Chapter 6.

2.3.3 Pyrolysis Temperature

Polymer precursors are heated under a controlled temperature protocol during pyrolysis. Pyrolysis temperature is the highest temperature that the precursor reaches. It is a key parameter of the carbonization reaction. Usually, pyrolysis temperature is selected at a temperature above its decomposition temperature but well below the graphitization temperature.

Pyrolysis temperature has a strong impact on CMS membrane separation properties. Generally, the increase of pyrolysis temperature results in more compact CMS structure and smaller pore sizes. Thus lower permeability and higher selectivity is expected. This trend has been confirmed by a series of studies on different polyimides for the separation of O_2/N_2, CO_2/CH_4, CO_2/N_2, C_2H_4/C_2H_6, and C_3H_6/C_3H_8 [19, 36-39]. The optimum temperature depends on the selection of polymer precursor and the specific application. For example, size-similar gas pairs might require higher pyrolysis temperature to obtain adequate selectivity; while gas pairs with larger size difference might prefer lower pyrolysis temperature to get higher permeability, since the selectivity is high enough and is not a major concern.

2.3.4 Ramp Rate

The temperature ramp rate can influence the total pyrolysis time and the rate of evolution of volatile molecules from the polymer matrix during carbonization. Suda and Haraya have shown that the increase of ramp rate can result in higher permeability by varying heating rate from 1.33K/min to 13.3 K/min [13]. It is believed that slower evolution of by-product and longer total pyrolysis time allow higher extent of pore sintering, which leads to smaller average pore size and lower permeability [14].

2.3.5 **Soak Time**

Soak time refers to the duration of time that precursor is held at the final pyrolysis temperature. It is another factor that can tune the microstructure of CMS membranes.

Longer soak time promotes the sintering of pore structure and narrows average pore size. Studies have shown that the increase of soak time can result in decreased permeability and increased selectivity for a series of polyimides [4, 40]. However, results by Steel showed that soak time has larger effect on permeability but smaller effect on selectivity. Also, as the pyrolysis temperature increases from 550 ℃ to 800 ℃, the influence of soak time on selectivity becomes even less pronounced (Figure 2.4) [4].

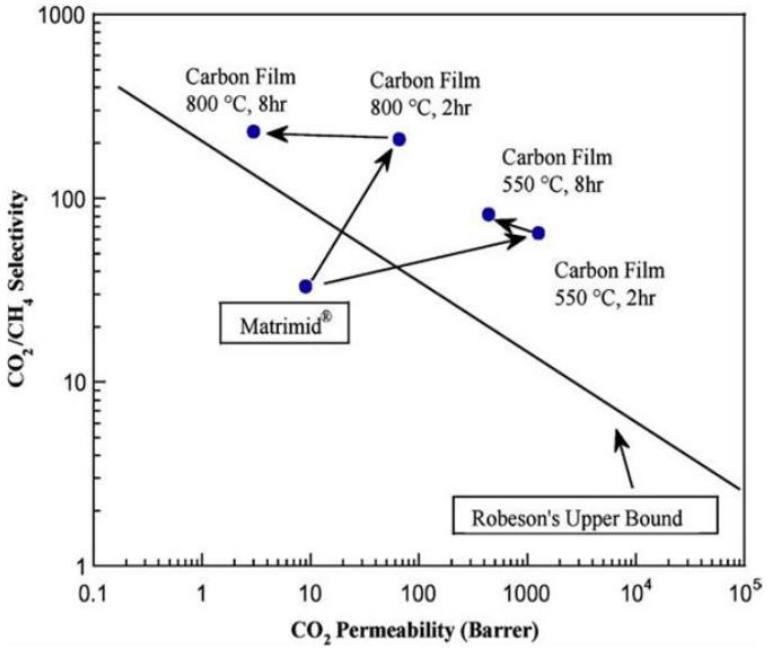

Figure 2.4: Effect of thermal soak time on Matrimid®-derived CMS membranes for CO_2/CH_4 separation [4].

The effect of pyrolysis temperature and soak time studied in this work will be discussed and presented in Chapter 4.

2.3.6 Pyrolysis Atmosphere

The pyrolysis atmosphere is controlled to be essentially inert to prevent undesired burn-off of membrane precursor. Vacuum and inert gas purging have been used for the pyrolysis environment. Previous studies have shown that vacuum pyrolysis yields more selective but less permeable CMS membranes than inert gas purging pyrolysis [3, 41]. However, vacuum pyrolysis has been shown to lack reproducibility due to the poor control of vacuum level. The vacuum level can varies significantly from system to system because of the sealing of pyrolysis system and the power of pump. The vacuum is correlated to the oxygen level in the pyrolysis system, which can have big influence on the pore structure in CMS membranes.

Controlled, mostly inert, gas purging is preferred to vacuum for practical scale-up. With such purging, the oxygen level can also be better controlled since the positive pressure in pyrolysis system prevents the invasion of oxygen from air. Geiszler investigated the effect of flow rate at 20 and 200 ccSTP/min argon and helium purging. Results revealed that higher permeability was obtained at higher flow rate while selectivity remained the same within the error range [3]. It is suggested that higher flow rate may enhance the convective mass transfer of pyrolysis by-products from membrane surface and result in more open CMS structure with higher permeability [3].

Oxygen can selectively chemisorb onto the edges of ultramicropores during pyrolysis, resulting in a significant influence of the molecular sieving properties of CMS membranes [42, 43]. Kiyono, Williams and Koros have developed an oxygen doping method to fine tune the CMS membrane separation performance [18, 44, 45]. Figure 2.5

illustrates the mechanism of oxygen doping. As precursor is carbonized at elevated temperature, trace amount of oxygen in the inert gas flow tends to selectively chemisorb to the edges of carbon lamellae which form the ultramicropores. The chemi-sorption at this site is ~17 times more reactive than that at the carbon basal planes, which form the micropores [42]. Thus the molecular sieving site of ultramicropores can be fine-tuned to improve selectivity, while the micropores can be kept at open structure to largely maintain the permeability.

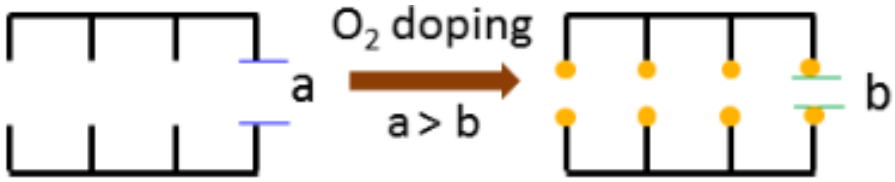

Figure 2.5: Mechanism of oxygen doping on CMS membranes.

Kiyono carried out a detailed study on oxygen doping method and discovered the oxygen concentration in the pyrolysis atmosphere is critical for separation properties. The oxygen level can be optimized for different gas pairs while the polymer precursor and pyrolysis temperature is controlled. Figure 2.6 shows the optimization of oxygen level for CO_2/CH_4 separation with 6FDA:BPDA-DAM pyrolyzed at 550 ℃.

In this work, the influence of pyrolysis atmosphere will be discussed and presented in Chapter 4.

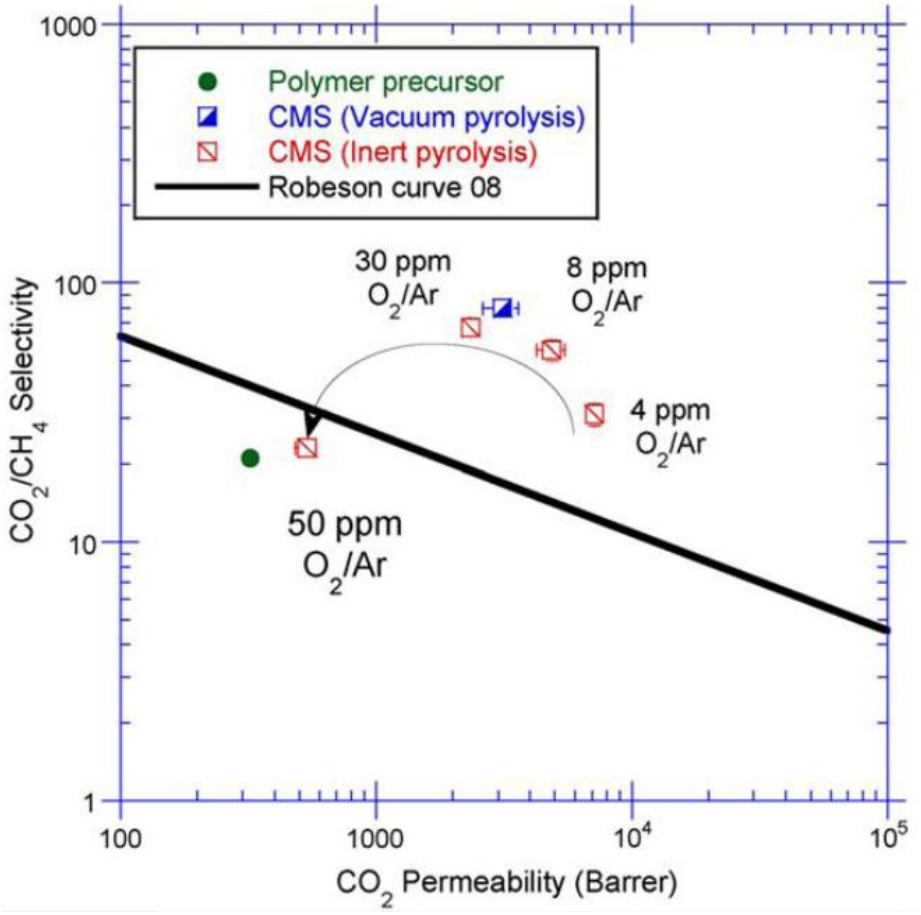

Figure 2.6: Effect of oxygen level on separation performance of 550 ℃ pyrolyzed 6FDA:BPDA-DAM for CO_2/CH_4 [43].

2.3.7 Post-treatment of Carbon Molecular Sieve Membrane

Several post-treatment techniques including post-oxidation and chemical vapor deposition have been used to further adjust the pore structure of CMS membranes. Post-oxidation in air has been applied to cellulose and polyimide-derived CMS membranes to increase the pore volume and permeability [46, 47]. However, selectivity is compensated at the same time. Chemical vapor deposition technique was developed to enhance

selectivity by introducing hydrocarbon or propylene carbon source to narrow the pore structure in CMS membranes [48].

While post-treatment methods may be useful in tuning CMS pore structure, it might also increase the complexity and cost of membrane fabrication process. Thus this method was not investigated in the current work.

2.4 Fundamentals of Gas Transport in Membranes

Gas separation membrane is a selective barrier. When a gas mixture is fed at the upstream side of the membrane, certain components selectively pass through the membrane as a permeate stream, while other components are rejected at the retentate side of the membrane. Several mechanisms have been found to selectively transport gas penetrants through membranes: (i) Knudsen diffusion transport, (ii) selective surface adsorption with surface diffusion, (iii) molecular sieving transport, and (iv) sorption-diffusion transport [49, 50]. These mechanisms are shown in Figure 2.7.

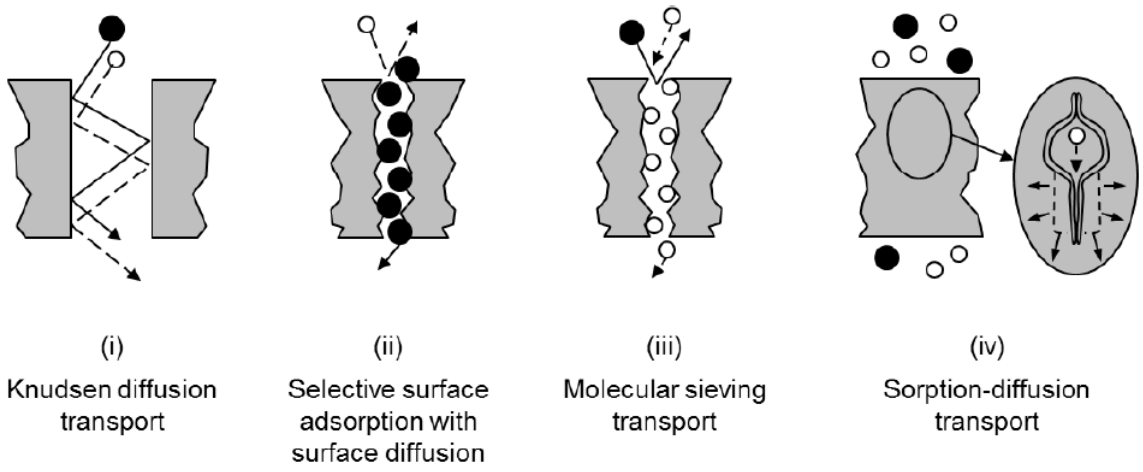

Figure 2.7: General mechanisms for selective gas and vapor transport through membranes [49, 50].

Knudsen flow occurs when the pore size in membrane is smaller than the mean free path of gas molecules. The discrimination between gas penetrants can be based on their molecular weights, as

$$\alpha_{A/B} = \sqrt{\frac{M_A}{M_B}} \tag{2.1}$$

Where $\alpha_{A/B}$ represents the diffusion selectivity of gas penetrant A over B, and M_A and M_B represent the molecular mass of gas A and B, respectively. Selective adsorption separation occurs when certain penetrants are preferentially adsorbed into the membrane while other penetrants are excluded, followed by surface diffusion of the adsorbed species across the membrane from one sorbed site to another. Molecular sieving transport occurs when gas penetrants are sieved by membrane pore structure based on their size and shape. Smaller molecules with the right shape can diffuse much faster than other gas

molecules in this mechanism. In sorption-diffusion transport mechanism, a combination of size (diffusivity) and condensability (solubility) determines which gas penetrant permeates faster through the membrane. This mechanism is commonly used for polymer and molecular sieve membranes.

2.4.1 Permeation

According to the sorption-diffusion model, gas molecules sorb into the membrane at the high pressure upstream, then diffuse through the membrane under the influence of a chemical potential gradient, and finally desorb from the membrane at the low pressure downstream side [50]. Figure 2.8 shows the schematic membrane separation process for N_2/CH_4. Mixture of N_2 and CH_4 gas is fed at the high pressure upstream side. The smaller gas N_2 permeates faster through the membrane and is enriched at the low pressure downstream side; the larger CH_4 permeates slower through the membrane is enriched at the upstream side.

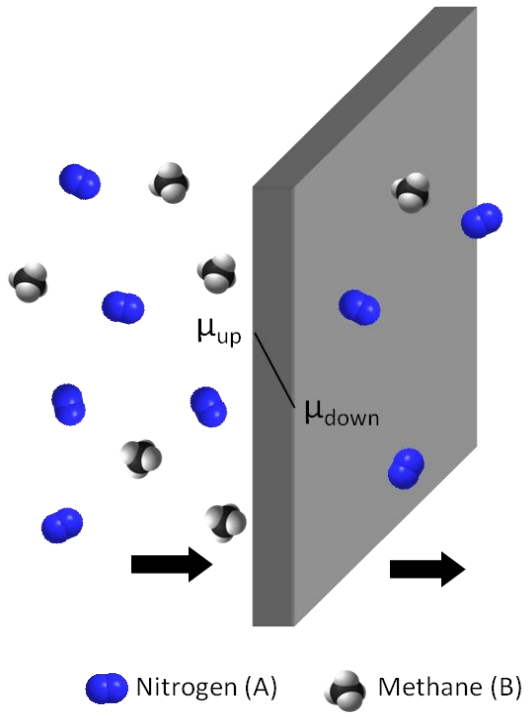

Figure 2.8: Schematic membrane separation process for N_2/CH_4.

Permeability and permselectivity are two intrinsic properties to evaluate the performance of membrane materials in terms of productivity and separation efficiency. The permeability of a membrane of a given gas A is defined as the pressure-and-thickness-normalized flux, given by the following expression:

$$P_A = \frac{N_A \cdot l}{\Delta p_A} \tag{2.2}$$

where N_A is molar flux of A, l is membrane thickness, and Δp_A is partial pressure difference between upstream and downstream for gas A. It is common to express permeability in Barrer, for which the unit is given below.

$$1\ Barrer = 10^{-10}\ \frac{cm^3(STP)\cdot cm}{cm^2 \cdot s \cdot cmHg} \tag{2.3}$$

The membrane thickness can be easily determined for homogeneous dense film. However, for asymmetric hollow fiber membranes, the exact thickness of the separation layer cannot be accurately determined. So productivity of these membranes is described by permeance, which is defined as the pressure-normalized flux:

$$\left(\frac{P}{l}\right)_A = \frac{N_A}{\Delta p_A} \tag{2.4}$$

"Gas Permeation Unit" (GPU) is usually used as the unit for permeance, which is defined as:

$$1\ GPU = 1\times 10^{-6}\ \frac{cm^3(STP)}{cm^2 \cdot s \cdot cmHg} \tag{2.5}$$

Permeability usually increases with temperature, following an Arrhenius relationship:

$$P_A = P_{0A}\, exp\left(\frac{-E_{PA}}{RT}\right) \tag{2.6}$$

where P_{0A} is the preexponential factor for permeation, E_{PA} is the activation energy for permeation, R is the molar gas constant, and T is the temperature.

The flux of gas molecules through solution-diffusion membranes is governed by Fick's law [51]. The equation for one-dimentional diffusion is given below.

$$N_A = -D_A \frac{dC_A}{dx} \tag{2.7}$$

In Eq. (2.7), N_A is the mass flux of component A, D_A is the diffusion of component A through the membrane, C_A is the concentration of component A, and x is

the coordinate in the direction of permeation. Eq. (2.7) can be fitted into the equation for permeance (Eq. 2.4) to obtain the following expression.

$$\frac{P_A}{l} = \frac{-D_A \frac{dC_A}{dx}}{\Delta p_A} \tag{2.8}$$

Diffusion coefficient depends on local concentration. Thus an average diffusion coefficient $\overline{D}_A$ for component A can be obtained from the following equation:

$$\overline{D}_A = \frac{\int_{C_{Z,down}}^{C_{A,up}} D_A(C_A) dC_A}{\int_{C_{Z,down}}^{C_{A,up}} dC_A} \tag{2.9}$$

where Ci,up and Ci,down are the concentrations of component A in the upstream and downstream sides of the membrane, respectively. Substituting Eq. (2.9) into Eq. (2.8) gives an expression for permeability in terms of the average diffusion coefficient:

$$P_A = \frac{\overline{D}_A (C_{A,up} - C_{A,down})}{\Delta p_A} \tag{2.10}$$

The average sorption coefficient can be defined as:

$$\overline{S}_A = \frac{C_{A,up} - C_{A,down}}{\Delta p_A} \tag{2.11}$$

Therefore, Eq. (2.10) can be further simplified into the following equation to express the permeability of a solution-diffusion membrane, where the permeability is a product of the kinetic factor of diffusion coefficient, and the thermodynamic factor of sorption coefficient.

$$P_A = \overline{D}_A \cdot \overline{S}_A \tag{2.12}$$

The separation factor between gases A and B is defined as the ratio of permeate-side and feed-side mole fractions of A and B. When downstream pressure is held at vacuum, the separation factor equals to the intrinsic permselectivity of the membrane, $\alpha_{A/B}$ [50]. The permselectivity is also a product of diffusion selectivity $\frac{D_A}{D_B}$ and sorption selectivity $\frac{S_A}{S_B}$, so:

$$\alpha_{A/B} = \frac{(y_A / y_B)_{permeate}}{(x_A / x_B)_{feed}} = \frac{P_A}{P_B} = \frac{(P/l)_A}{(P/l)_B} = \frac{\overline{D}_A}{\overline{D}_B} \cdot \frac{\overline{S}_A}{\overline{S}_B} \tag{2.13}$$

2.4.2 Sorption

The sorption coefficient describes the amount of gas taken up by membrane material at equilibrium at a given pressure:

$$S_A = \frac{C_A}{p_A} \tag{2.14}$$

For polymeric membranes, gas penetrants may sorb either into well packed Henry's law regions by dilation of the matrix, or into the preexisting gaps between polymer chain segments comprising Langmuir regions [52]. The Henry's law region is in the dense polymer matrix where ordinary dissolution happens. This type of sorption is available in both rubbery and glassy polymers. The Langmuir sorption occurs in a limited

number of holes or microvoids in the polymer matrix corresponding to the unrelaxed excess free volume in glassy polymers. Figure 2.9 shows the specific volume of a polymer sample versus temperature. The sorption in glassy polymer membranes can be described by a dual mode sorption model, shown as in the following equation

$$C_A = C_{DA} + C_{HA} = k_{DA} p_A + \frac{C'_{HA} b_A p_A}{1 + b_A p_A} \tag{2.15}$$

where C_A is the concentration of sorbed penetrant A, C_{DA} is the concentration in Henry's region, C_{HA} is the concentration in Langmuir region, k_{DA} is the Henry's law coefficient, p_A is the partial pressure, C'_{HA} is the Langmuir hole-filling capacity and b_A is the Langmuir affinity constant. A typical sorption isotherms showing the concentration of sorbed penetrant at a given pressure and temperature is presented in Figure 2.10.

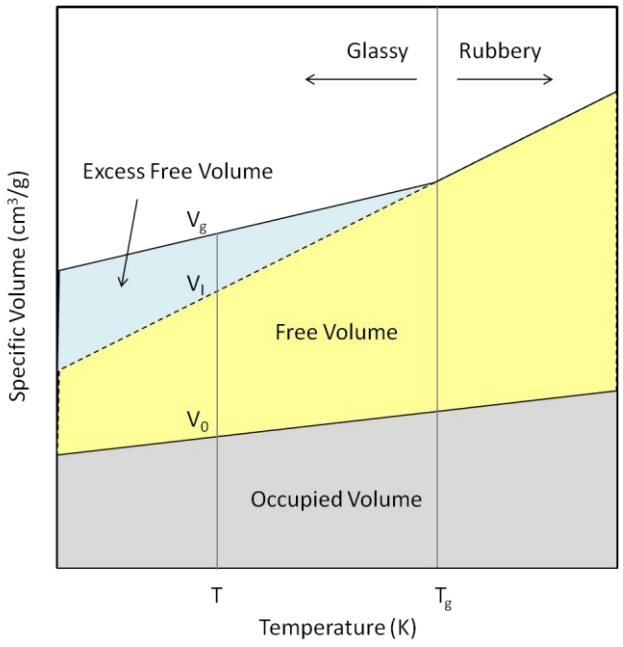

Figure 2.9: Specific volume of a hypothetical polymer sample versus temperature.

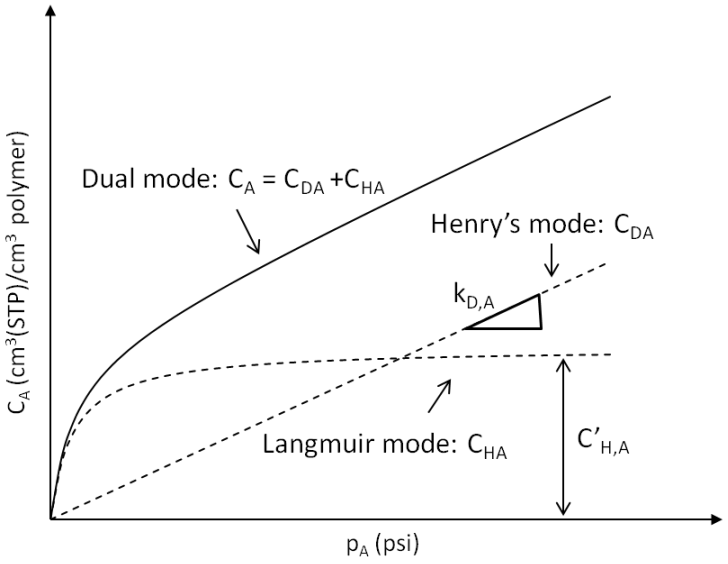

Figure 2.10: Typical sorption isotherm.

For CMS membranes, there is no dilation of the rigid CMS structure. The majority of gas penetrants are sorbed in the micropores, which can be described by the Langmuir isotherm, as shown in the following equation:

$$C_A = C_{HA} = \frac{C'_{HA} b_A p_A}{1 + b_A p_A} \tag{2.16}$$

For multiple components, competitive sorption happens when more than one component competes to take the same sorption sites. In such a case, sorption selection favors the gas penetrant with higher Langmuir affinity constant b. The sorption isotherm for multiple components can be expressed as below:

$$C_i = C_{Hi} = \frac{C'_{Hi} b_i p_i}{1 + \sum b_i p_i} \tag{2.17}$$

The thermodynamically-based sorption coefficient $\mathcal{S}_A$ decreased with temperature, following van't Hoff equation [53]:

$$\mathcal{S}_A = \mathcal{S}_{0A} \exp\left(\frac{-H_{SA}}{RT}\right) \tag{2.18}$$

where $\mathcal{S}_{0A}$ is the preexponential factor for sorption, and H_{SA} is the apparent heat of sorption, which is typically negative.

2.4.3 Diffusion

In polymer and CMS membranes, gas molecules diffuse through the membrane by making random jumps from site to site. The diffusion coefficient measures the mobility of a gas penetrant through the membrane. It is a function of frequency of jumps (f_A) and average jump length λ_A [54]:

$$D_A = \frac{f_A \lambda_A^2}{6} \tag{2.19}$$

In polymer membranes, diffusion of sorbed gas penetrant happens in transient gaps that are continuously created and redistributed by thermally stimulated polymer chain segmental motions [53, 54]. A sufficient-sized transient gap enables an adjacent sorbed gas molecule to execute a diffusion jump, as shown in Figure 2.11. The gas molecules enclosed in a sorption site are considered to be in the normal state of a diffusion jump. The gas molecules going through the transient gap between dilated polymer chains are considered to be in the activated state. The diffusion coefficient in

polymer membranes is controlled by the penetrant size, the packing and mobility of the polymer chains, and the cohesive energy [55].

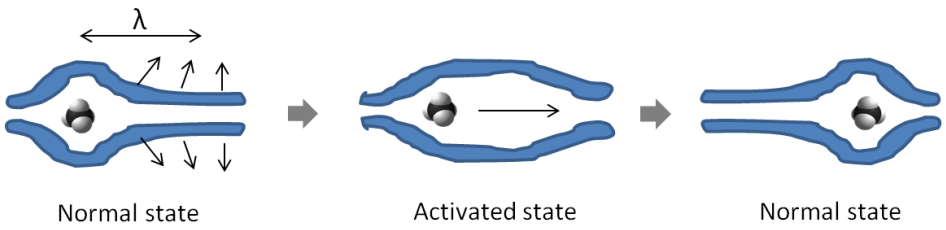

Figure 2.11: Depiction of a gas molecule making a diffusion jump through a transient gap between polymer chains.

In CMS membranes, the diffusion of gas penetrant is different from that in polymer membranes due to the rigid pore structure. The micropores form the sorption site in CMS sites. Gas penetrants have to overcome the repulsion energy from rigid ultramicropores to perform a diffusion jump from one sorption site to another. Gas molecules residing in micropores are considered to be in the normal state of a diffusion jump. Gas molecules going through ultramicropores are considered to be in the activated state. The diffusion of a gas molecule in CMS membranes is shown in Figure 2.12. The rigid ultramicropore structure in CMS membranes can very effectively discriminate the shapes and sizes of different gas molecules, resulting in high diffusion selectivity.

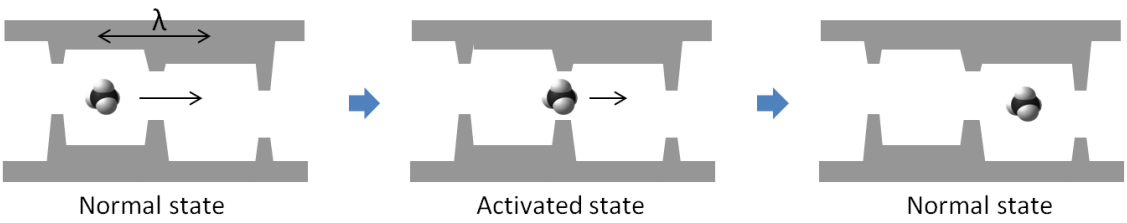

Figure 2.12: Depiction of a gas molecule making a diffusion jump from one micropore to another in CMS membranes.

Gas diffusion in CMS membrane is an activated process and the diffusion coefficient D_A follows an Arrhenius relationship:

$$D_A = D_{0A}\, exp\left(\frac{-E_{DA}}{RT}\right) \tag{2.20}$$

where D_{0A} is the pre-exponential factor and E_{DA} is the activation energy for diffusion of penetrant A.

2.4.4 Energetic and Entropic Contributions to Diffusion Selectivity

As the rigid ultramicropore window size approaches the minimum dimension of gas penetrants, very effective size and shape diffusion selection becomes possible, thereby providing high diffusion selectivity [37]. As described in the previous section, diffusion coefficient follows an Arrhenius relationship. According to Eq. (2.20), the diffusion selectivity can be expressed in the following equation:

$$\frac{D_A}{D_B} = \frac{D_{0A}}{D_{0B}}\, exp\left(-\frac{E_{DA} - E_{DB}}{RT}\right) \tag{2.21}$$

The pre-exponential factor D_0 can be represented from transition state theory as

$$D_0 = e\lambda^2 \frac{kT}{h} exp\left[\frac{S_D}{R}\right] \tag{2.22}$$

where λ is the average diffusive jump length, S_D is the activation entropy of diffusion, *k* is Boltzmann's constant, and *h* is Planck's constants [56]. Note that the *S* used for entropy here is different from the $\mathcal{S}$ used for the sorption coefficient. For gas pairs with similar kinetic diameters able to access all of the micropores, λ can be considered equal for both gases [57]. According to Eq. (2.21) and (2.22), the diffusion selectivity for a gas pair can be decomposed to the product of an entropic factor and an energetic factor, as shown below:

$$\frac{D_A}{D_B} = exp\left(\frac{S_{DA} - S_{DB}}{R}\right) \cdot exp\left(-\frac{E_{DA} - E_{DB}}{RT}\right)$$

$$= \underbrace{exp\left(\frac{\Delta S_{DA,B}}{R}\right)}_{\text{Entropic Selectivity}} \cdot \underbrace{exp\left(-\frac{\Delta E_{DA,B}}{RT}\right)}_{\text{Energetic Selecitivity}} \tag{2.23}$$

where $\Delta S_{DA,B}$ is the difference in the diffusion activation entropy for penetrants A and B, and $\Delta E_{DA,B}$ is the difference in the activation energy of diffusion for penetrants A and B. The difference in activation entropy provides entropic diffusion selection effect; while the difference in activation energy provides energetic diffusion selection effect. Unlike polymer membranes, highly rigid size and shape media such as CMS materials show considerable entropic diffusion selectivity [19, 57].

According to transition state theory, the diffusion coefficient for a penetrant through any medium can be described by the following equation

$$D = \lambda^2 \frac{kT}{h} \frac{F^{\neq}}{F} exp\left(\frac{-E_D}{RT}\right) \tag{2.24}$$

where $F^{\neq}$ represents the partition function for the gas penetrant in activated state, and F is the partition function for the same molecule in the normal state [56, 57]. Considering equal diffusive jump length, the entropic diffusion selectivity can be written as

$$\left(\frac{D_A}{D_B}\right)_{entropic} = \frac{D_{0A}}{D_{0B}} = exp\left(\frac{S_{DA} - S_{DB}}{R}\right) = \frac{(F^{\neq}/F)_A}{(F^{\neq}/F)_B} \tag{2.25}$$

The partition function consists of translational, rotational, and vibrational contributions, as shown below.

$$F = F_{trans} \cdot F_{rot} \cdot F_{vib} \tag{2.26}$$

The ultramicropores in CMS membranes are analogous to the selective window openings in zeolite. Such pore structure can restrict certain translational and rotational degrees of freedom, resulting in reduced value of partition function in the activated state, $F^{\neq}$. The motions of bulky gas molecules tend to be more restricted than slimmer gas molecules in activated state. Thus considerable entropic diffusion selectivity can be observed CMS membranes, which is lacking in polymeric membranes comprising flexible chains. This capability can be especially useful for similar sized gas pairs like N_2 and CH_4.

2.5 References

[1] Jenkins GM, Kawamura K. Polymeric carbons -- carbon fiber, glass and char. London: Cambridge University Press; 1976.

[2] Pierson HO. Handbook of carbon, graphite, diamond, and fullerenes. New Jersey: Noyes; 1993.

[3] Geiszler VC. Polyimide precursors for carbon molecular sieve membranes. Austin TX USA: University of Texas at Austin; 1997.

[4] Steel KM. Carbon membranes for challenging gas separations. Austin: University of Texas at Austin; 2000.

[5] Stoeckli HF. Microporous carbons and their characterization: The present state of the art. Carbon 1990;28(1):1-6.

[6] Hatori H, Yamada Y, Shiraishi M, Yoshihara M, Kimura T. The mechanism of polyimide pyrolysis in the early stage. Carbon 1996;34(2):201-8.

[7] Inagaki M, Ibuki T, Takeichi T. Carbonization behavior of polyimide films with various chemical structures. J Appl Polym Sci 1992;44(3):521-5.

[8] Ehlers GFL, Fisch KR, Powell WR. Thermal degradation of polymers with phenylene units in the chain. Iv. Aromatic polyamides and polyimides. Journal of Polymer Science Part A-1: Polymer Chemistry 1970;8(12):3511-27.

[9] Rungta M. Carbon molecular sieve dense film membranes for ethylene/ethane separations. Atlanta: Georgia Institute of Technology; 2012.

[10] Fuertes AB, Menendez I. Separation of hydrocarbon gas mixtures using phenolic resin-based carbon membranes. Sep Purif Technol 2002;28(1):29-41.

[11] Wei W, Qin G, Hu H, You L, Chen G. Preparation of supported carbon molecular sieve membrane from novolac phenol–formaldehyde resin. J Membr Sci 2007;303(1–2):80-5.

[12] Centeno TA, Fuertes AB. Supported carbon molecular sieve membranes based on a phenolic resin. J Membr Sci 1999;160(2):201-11.

[13] Suda H, Haraya K. Gas permeation through micropores of carbon molecular sieve membranes derived from kapton polyimide. The Journal of Physical Chemistry B 1997;101(20):3988-94.

[14] Williams PJ, Koros WJ. Gas separation by carbon membranes. Advanced membrane technology and applications 2008:599-631.

[15] Jones CW, Koros WJ. Carbon molecular sieve gas separation membranes-i. Preparation and characterization based on polyimide precursors. Carbon 1994;32(8):1419-25.

[16] Fuertes A, Nevskaia D, Centeno T. Carbon composite membranes from matrimid< sup>®</sup> and kapton< sup>®</sup> polyimides for gas separation. Microporous Mesoporous Mater 1999;33(1):115-25.

[17] Barsema J, Klijnstra S, Balster J, Van Der Vegt N, Koops G, Wessling M. Intermediate polymer to carbon gas separation membranes based on matrimid pi. J Membr Sci 2004;238(1):93-102.

[18] Kiyono M, Williams PJ, Koros WJ. Effect of polymer precursors on carbon molecular sieve structure and separation performance properties. Carbon 2010;48(15):4432-41.

[19] Rungta M, Xu L, Koros WJ. Carbon molecular sieve dense film membranes derived from matrimid® for ethylene/ethane separation. Carbon 2012;50(4):1488-502.

[20] Lie JA, Hägg M-B. Carbon membranes from cellulose and metal loaded cellulose. Carbon 2005;43(12):2600-7.

[21] Koresh J, Soffer A. 185. A molecular sieve carbon membrane for continuous process gas separation. Carbon 1984;22(2):225.

[22] Acharya M, Foley HC. Spray-coating of nanoporous carbon membranes for air separation. J Membr Sci 1999;161(1):1-5.

[23] Acharya M, Raich BA, Foley HC, Harold MP, Lerou JJ. Metal-supported carbogenic molecular sieve membranes: Synthesis and applications. Ind Eng Chem Res 1997;36(8):2924-30.

[24] Centeno TA, Fuertes AB. Carbon molecular sieve gas separation membranes based on poly(vinylidene chloride-co-vinyl chloride). Carbon 2000;38(7):1067-73.

[25] Singh A. Membrane materials with enhanced selectivity: An entropic interpretation. Austin: The university of texas at Austin; 1997.

[26] Saufi SM, Ismail AF. Fabrication of carbon membranes for gas separation—a review. Carbon 2004;42(2):241-59.

[27] Williams PJ. Analysis of factors influencing the performance of cms membranes for gas separation. Atlanta: Georgia Institute of Technology; 2006.

[28] Park HB, Kim YK, Lee JM, Lee SY, Lee YM. Relationship between chemical structure of aromatic polyimides and gas permeation properties of their carbon molecular sieve membranes. J Membr Sci 2004;229(1):117-27.

[29] Xu L. Carbon molecular sieve hollow fiber membranes for olefin/paraffin separations. Atlanta: Georgia Institute of Technology; 2012.

[30] Tin PS, Chung T-S, Hill AJ. Advanced fabrication of carbon molecular sieve membranes by nonsolvent pretreatment of precursor polymers. Ind Eng Chem Res 2004;43(20):6476-83.

[31] Centeno TA, Fuertes AB. Carbon molecular sieve gas separation membranes based on poly (vinylidene chloride-< i> co-</i> vinyl chloride). Carbon 2000;38(7):1067-73.

[32] Xiao Y, Dai Y, Chung T-S, Guiver MD. Effects of brominating matrimid polyimide on the physical and gas transport properties of derived carbon membranes. Macromolecules 2005;38(24):10042-9.

[33] Kusuki Y, Shimazaki H, Tanihara N, Nakanishi S, Yoshinaga T. Gas permeation properties and characterization of asymmetric carbon membranes prepared by pyrolyzing asymmetric polyimide hollow fiber membrane. J Membr Sci 1997;134(2):245-53.

[34] Okamoto K-I, Kawamura S, Yoshino M, Kita H, Hirayama Y, Tanihara N, et al. Olefin/paraffin separation through carbonized membranes derived from an asymmetric polyimide hollow fiber membrane. Ind Eng Chem Res 1999;38(11):4424-32.

[35] Bhuwania N. Engineering the morphologhy of carbon molecular sieve (cms) hollow fiber membranes. Atlanta: Georgia Institute of Technology; 2013.

[36] Lafyatis DS, Tung J, Foley HC. Poly (furfuryl alcohol)-derived carbon molecular sieves: Dependence of adsorptive properties on carbonization temperature, time, and poly (ethylene glycol) additives. Ind Eng Chem Res 1991;30(5):865-73.

[37] Singh-Ghosal A, Koros WJ. Air separation properties of flat sheet homogeneous pyrolytic carbon membranes. J Membr Sci 2000;174(2):177-88.

[38] Steel KM, Koros WJ. An investigation of the effects of pyrolysis parameters on gas separation properties of carbon materials. Carbon 2005;43(9):1843-56.

[39] Vu DQ, Koros WJ, Miller SJ. High pressure co2/ch4 separation using carbon molecular sieve hollow fiber membranes. Ind Eng Chem Res 2002;41(3):367-80.

[40] Kim YK, Park HB, Lee YM. Preparation and characterization of carbon molecular sieve membranes derived from btda–oda polyimide and their gas separation properties. J Membr Sci 2005;255(1):265-73.

[41] Vu DQ. Formation and characterization of asymmetric carbon molecular sieve and mixed matrix membranes for natural gas purification. Austin: The University of Texas at Austin; 2001.

[42] Grisdale R. The properties of carbon contacts. J Appl Phys 2004;24(10):1288-96.

[43] Kiyono M. Carbon molecular sieve membranes for natural gas separations. Atlanta: Georgia Institute of Technology; 2010.

[44] Kiyono M, Williams PJ, Koros WJ. Effect of pyrolysis atmosphere on separation performance of carbon molecular sieve membranes. J Membr Sci 2010;359(1–2):2-10.

[45] Kiyono M, Williams PJ, Koros WJ. Generalization of effect of oxygen exposure on formation and performance of carbon molecular sieve membranes. Carbon 2010;48(15):4442-9.

[46] Koresh JE, Soffer A. The carbon molecular sieve membranes. General properties and the permeability of ch4/h2 mixture. Sep Sci Technol 1987;22(2-3):973-82.

[47] Kusakabe K, Yamamoto M, Morooka S. Gas permeation and micropore structure of carbon molecular sieving membranes modified by oxidation. J Membr Sci 1998;149(1):59-67.

[48] Amar A, Azariah M, Cohen H, Golub D, Saguee S, Soffer A, et al., inventors; Google Patents, assignee. Method of improving the selectivity of carbon membranes by chemical carbon vapor deposition patent US5695818A. 1997.

[49] Koros W. Membranes: Learning a lesson from nature. Chem Eng Prog 1995;91(10):68-81.

[50] Koros W, Fleming G. Membrane-based gas separation. J Membr Sci 1993;83(1):1-80.

[51] Koros WJ, Chern RT. Separation of gaseous mixtures using polymer membranes. In: Rousseau RW, editor. Handbook of separation process technology. New York: John Wiley & Sons, Ltd.; 1987.

[52] Paul DR, Koros WJ. Effect of partially immobilizing sorption on permeability and the diffusion time lag. Journal of Polymer Science: Polymer Physics Edition 1976;14(4):675-85.

[53] Koros WJ, Madden WC. Transport properties. Encyclopedia of polymer science and technology 2002.

[54] Koros WJ. Barrier polymers and structures. Washington D.C.: American Chemical Society; 1990.

[55] Crank J, Park GS. Diffusion in polymers: Academic Press; 1968.

[56] Glasstone S, Laidler KJ, Eyring H. The theory of rate processes: The kinetics of chemical reactions, viscosity, diffusion and electrochemical phenomena. New York: McGraw-Hill Book Company, Incorporated; 1941.

[57] Singh A, Koros WJ. Significance of entropic selectivity for advanced gas separation membranes. Ind Eng Chem Res 1996;35(4):1231-4.

CHAPTER 3

MATERIALS AND EXPERIMENTAL PROCEDURES

3.1 Overview

This chapter describes materials and experimental procedures used in this study. Section 3.2 discusses the polymers and gases involved in this work. Section 3.3 describes the membrane fabrication methods for both polymer and carbon molecular sieve in the morphologies of dense film and hollow fiber. Finally, Section 3.4 presents the various characterization techniques and equipments.

3.2 Materials

3.2.1 Polymers

Most of the precursors used for CMS membranes are polyimides. Some of these polyimides are commercially available, while the others are custom or in-house synthesized. Matrimid® 5218 is the commercial name of BTDA-DAPI and is supplied by Huntsman in the form of yellow powder. P84® is the commercial name of BTDA-TDI/MDI developed by Evonik. Kapton® is a commercial film made from polyimide PMDA-ODA and is supplied by DuPont. Torlon® is the commercial name of a polyamide-imide (PAI). 6FDA:BPDA(1:1)-DAM and 6FDA-DAM were custom synthesized and supplied in the form of white fibers by Akron Polymer Systems, Inc. 6FDA:mPDA was synthesized in-house and kindly provided by Wulin Qiu. BTDA-

s/aMDA and BTDA-sMDA were synthesized in the current study. The details of this synthesis will be provided in Chapter 5.

3.2.2 Gases

All pure gases used for permeation test, sorption test, and pyrolysis were provided by Airgas with purity of 99.999% or greater. The pure gases used include N_2, CH_4, O_2, CO_2, and Ar. Mixed gas of 20% N_2/80% CH_4 was supplied by Airgas. Mixed gases with "ppm" level of O_2 or H_2 with balance Ar were purchased from Praxair.

3.3 Membrane Formation

3.3.1 Polymer Membrane Formation

Most of the polymer films were prepared by solution casting method while BTDA-s/aMDA and BTDA-sMDA dense films were prepared by melt pressing method due to their poor solubility in common solvents at room temperature. Before film formation, all polymers were first dried in convection oven at 110 ℃ for at least 12 hours to remove moisture.

3.3.1.1 Dense Film Solution Casting

The dried polymer was dissolved in dichloromethane (≥99.8% purity, Sigma-Aldrich) to form a 2-5 wt% polymer solution in a 40 ml ICHEM vial (Fisher Scientific)

and placed on a roller for at least 6 hours to allow well mixing. The polymer solution was then used to prepare polymer dense film by a solution casting method at room temperature, as shown in Figure 3.1. The entire casting set-up was placed and sealed inside a glove bag (Cole Parmer) in a fume hood. The set-up included leveled stage, Teflon® disk, polymer solution in vial, 30 ml syringe with a Millex®-RH micron PTFE filter (Micropore Corporation), short-neck glass funnel, as well as two jars containing excess dichloromethane. The sealed glove bag was purged with nitrogen and then dichloromethane in the two jars was allowed to evaporate to saturate the atmosphere in glove bag for 3 hours. After that, the polymer solution was transferred from the vial to the syringe and slowly pushed through the filter into the Teflon® disk. The Teflon® disk was then covered with the inverted glass funnel with open end plugged with Kimwipe, which allowed minimum solvent evaporation rate. After 3 days, the vitrified film was removed from glove bag and dried in a vacuum oven at 120 ℃ for at least 12 hours to remove residual solvent.

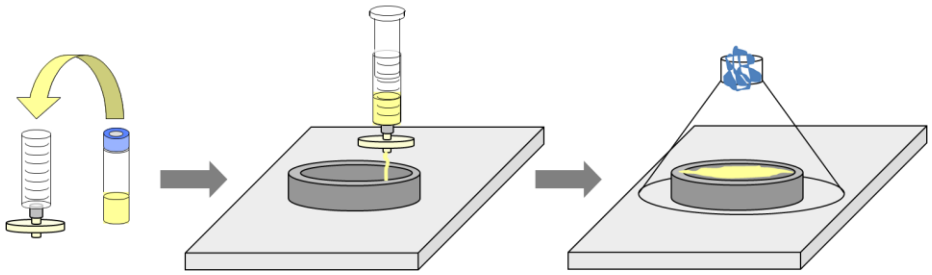

Figure 3.1: Schematic of solution casting method for polymer dense film preparation.

3.3.1.2 Dense Film Melt Pressing

Due to the poor solubility of BTDA-s/aMDA and BTDA-sMDA in common solvents at room temperature, these two polymer dense films were prepared by melt pressing method similar to that developed previously [1, 2]. The hot press (Wabash press) machine in the Manufacturing Research Center at Georgia Institute of Technology was used to transform polymer powder into films. Polymer films were first preheated at 325 ℃ for 2 min and pressed under vacuum between two nonstick metal sheets (Faberware) at 30 ton and 325 ˚C for 30 sec and then immediately quenched in a water bath at room temperature. Stacked aluminum shim layers (hard-temper aluminum foil, McMaster Carr, 3 mils thick) with 9 cm circle cut out was used between the metal sheets to control the film thickness. The Schematic of melt pressing method is shown in Figure 3.2.

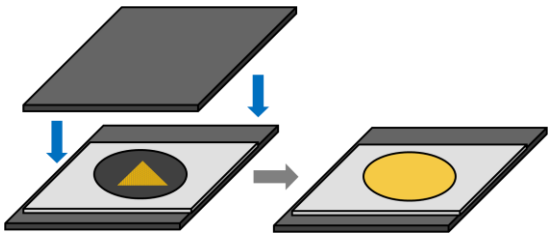

Figure 3.2: Schematic of melt pressing method for polymer dense film preparation.

3.3.1.3 Hollow Fiber Spinning

The hollow fiber spinning was performed by group members Liren Xu and Nitesh Bhuwania. Matrimid® was first dried in a convection oven at 110 ℃ for 24 hours and then mixed with solvents and non-solvent in a Qorpak® glass bottle to form a polymer

dope. NMP was chosen as the non-volatile solvent due to its relatively benign nature and miscibility with water. THF was chosen as the volatile solvent to assist the formation of skin layer. Ethanol was the non-solvent. After mixing, the dope was left on roller for 2 weeks to obtain a homogenous solution.

Asymmetric hollow fibers were formed via a dry-jet/wet-quench spinning process (Figure 3.3). The polymer dope was loaded into a 500 mL syringe pump (ISCO Inc., Lincoln, NE) and allowed to degas overnight. Bore fluid (96% NMP/ 4% water) was loaded into a 100 mL syringe pump. During spinning, the dope and bore fluid were co-extruded through a customized spinneret. The temperature during spinning was controlled by thermocouples placed on the spinneret, dope line and dope pump. As the polymer dope went through the air gap, dense skin layer was formed as solvent evaporated. When the dope and bore fluid were immersed into the water quench bath, phase separation occurred and porous support structure was formed. The hollow fiber was then collected on a rotating drum. The obtained hollow fibers were rinsed with four water baths for 48 hour and then solvent exchanged in three 20 min methanol baths and three 20 min hexane baths. After the solvent exchange, the hollow fibers were dried in vacuum oven at 75 ℃ for 2 hours.

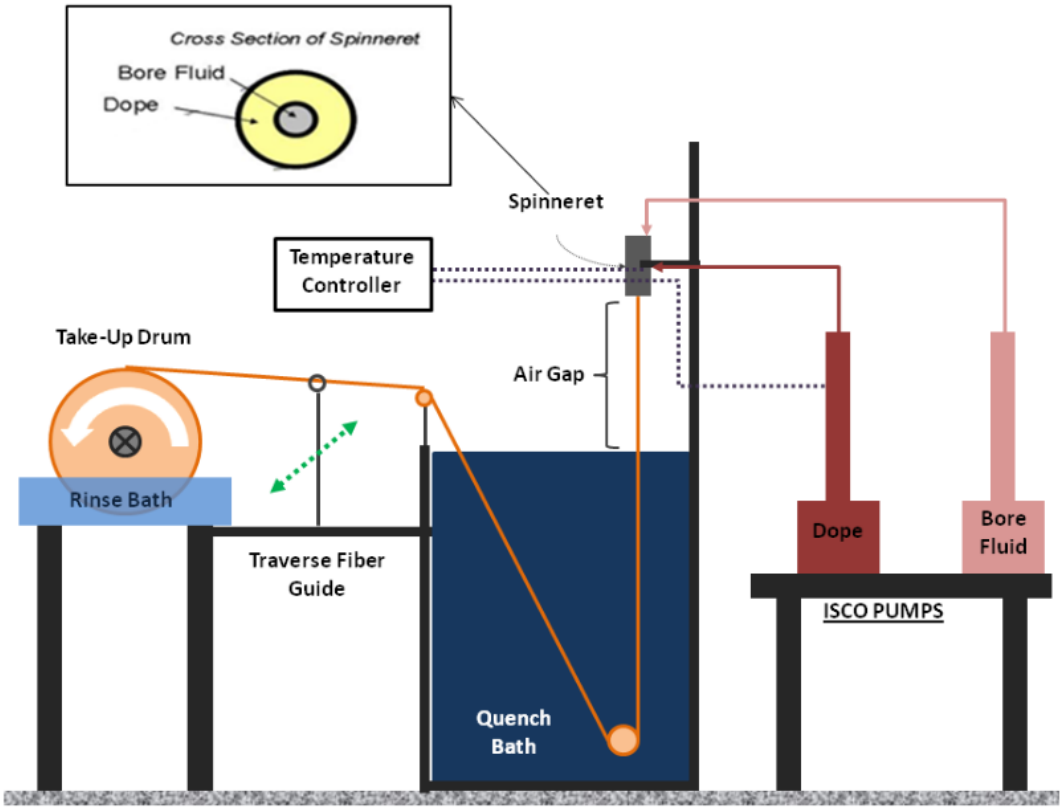

Figure 3.3: Dry-jet/wet-quench spinning process to fabricate polymer hollow fiber membranes [3].

3.3.2 Carbon Molecular Sieve Membrane Formation

3.3.2.1 Pyrolysis Set-up

Polymer membranes were pyrolyzed in a pyrolysis set-up updated from a previously reported apparatus [4], as shown in Figure 3.4. Polymer dense films were first cut into small discs with a one inch die and placed on a corrugated quartz plate (United Silica Products, Franklin, NJ). Then the quartz plate and dense films were loaded into a quartz tube (National Scientific Company, GE Type 214 quartz tubing, Quakertown, PA)

and placed into a pyrolysis furnace (Thermocraft, Inc., Model 23-24-1ZH, Winston-Salem, NC), which was connected to a temperature controller (Omega). The quartz tube was sealed by an assembly of metal flanges with silicon O-rings (MTI Corporation, Richmond, CA) on both ends. A mass flow controller (Alicat Scientific, Inc. Tucson, AZ) was used on the upstream side of the tube to accurately control the purge gas flow rate. On the downstream side, a U-shaped ¼ inch stainless steel tube was used to cool flowing gas below the maximum working temperature (650 ˚C) of the O_2 sensor. The oxygen sensor and analyzer (Cambridge Sensotec Ltd., Rapidox 2100 series, Cambridge, England) were integrated into the system to monitor the oxygen concentration during pyrolysis. A 1/8 inch stainless steel tube coil was attached in the purge line to prevent any back diffusion to the pyrolysis system.

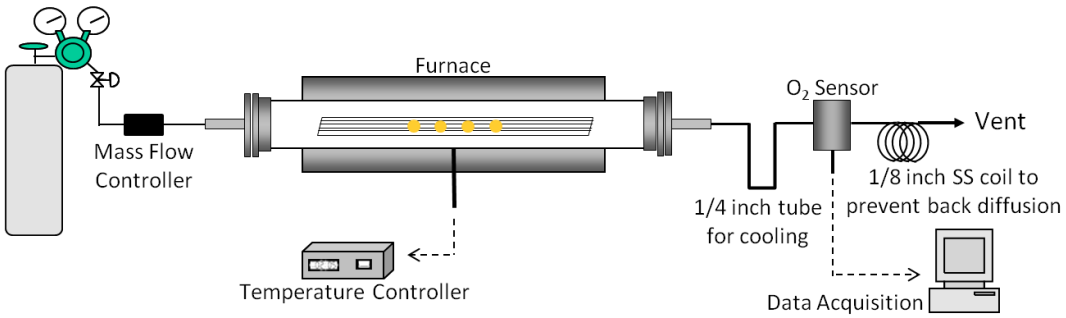

Figure 3.4: Schematic presentation of the pyrolysis system.

The pyrolysis of hollow fiber membranes was done in a three-zone furnace (Thermocraft, Inc., Model # XST-3-0-24-3C, Winston-Salem, NC) [5], which can provide uniform temperature control along the length of hollow fiber. A stainless steel wire mesh plate (McMaster Carr, Robbinsville, NJ) instead of quartz plate was used for

hollow fiber pyrolysis. Thin stainless steel wires were threaded onto the plate to loosely bind the fibers and to ensure the fibers were separate from each other. The quartz plate and mesh plate used for pyrolysis are shown in Figure 3.5.

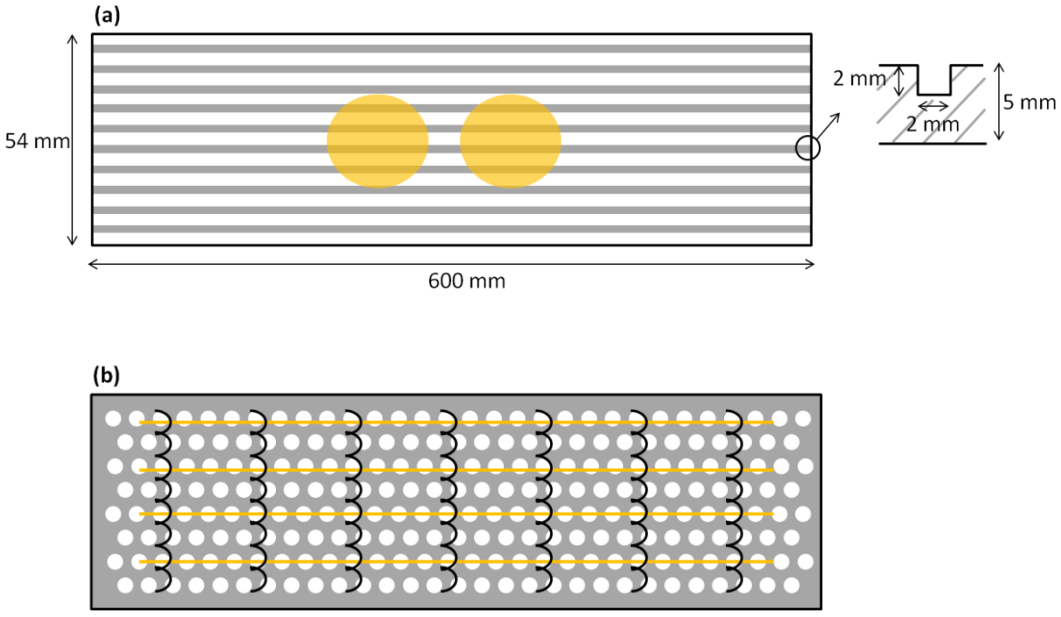

Figure 3.5: (a) Quartz plate and (b) mesh plate used for pyrolysis.

3.3.2.2 Pyrolysis Protocol

Polymer membranes were pyrolyzed under 200 scc/min inert gas purge to avoid external mass transfer complications. The inert gas was kept purging for at least 12 hours before heating started to ensure the desired pyrolysis atmosphere was achieved. After initial purging, the following previously optimized heating protocol [6, 7] was used to reach the final pyrolysis temperature.

(1) 50 → 250 ℃ at a ramp rate of 13.3 ℃/min.

(2) 250 ℃ → (T_{max} -15) ℃ at a ramp rate of 3.85 ℃/min.

(3) (T_{max} -15) ℃ → T_{max} ℃ at a ramp rate of 0.25 ℃/min.

(4) Soak at T_{max} for 2 hour.

After the heating protocol was complete, the furnace was allowed to cool naturally under the inert gas flow. The resulting CMS membranes were removed from the furnace for further characterization. After each pyrolysis run, both the quartz tube and the quartz plate or mesh plate were thoroughly rinsed with acetone and baked under 500 scc/min ultra high purity (UHP) air flow at 800 ℃ for 2 hour to remove any deposit that could affect subsequent runs.

3.4 Characterization Techniques

3.4.1 Permeation Test

3.4.1.1 Dense Film Masking

A permeation cell was used for polymer or CMS dense film permeation experiments. The cell is made of stainless steel and is sealed by o-ring assembly. The process to sandwich a film between the upstream and downstream sides of the permeation cell is called masking. The film was first masked by sandwiching between two concentric annular shaped pieces of impermeable aluminum tape (Avery Dennion) with test area exposed in the center. A third larger annular shaped piece of aluminum tape

was then used to hold the sandwiched film onto the bottom part of permeation cell. Usually two or three layers of filter paper were placed beneath the sandwich to provide cushion. Five minute epoxy (3M, DP-100) or higher temperature epoxy (Duralco 4525) was applied at the interface between the film and tape to seal any possible leaks. The permeation cell was finally assembled with O-rings and screws, and then loaded into permeation system. Figure 3.7 shows the masking assembly. The exposed test area was determined by counting pixels of scanned picture of CMS film using Photoshop. The film thickness was measure with a micrometer (Mitutoyo Series 293).

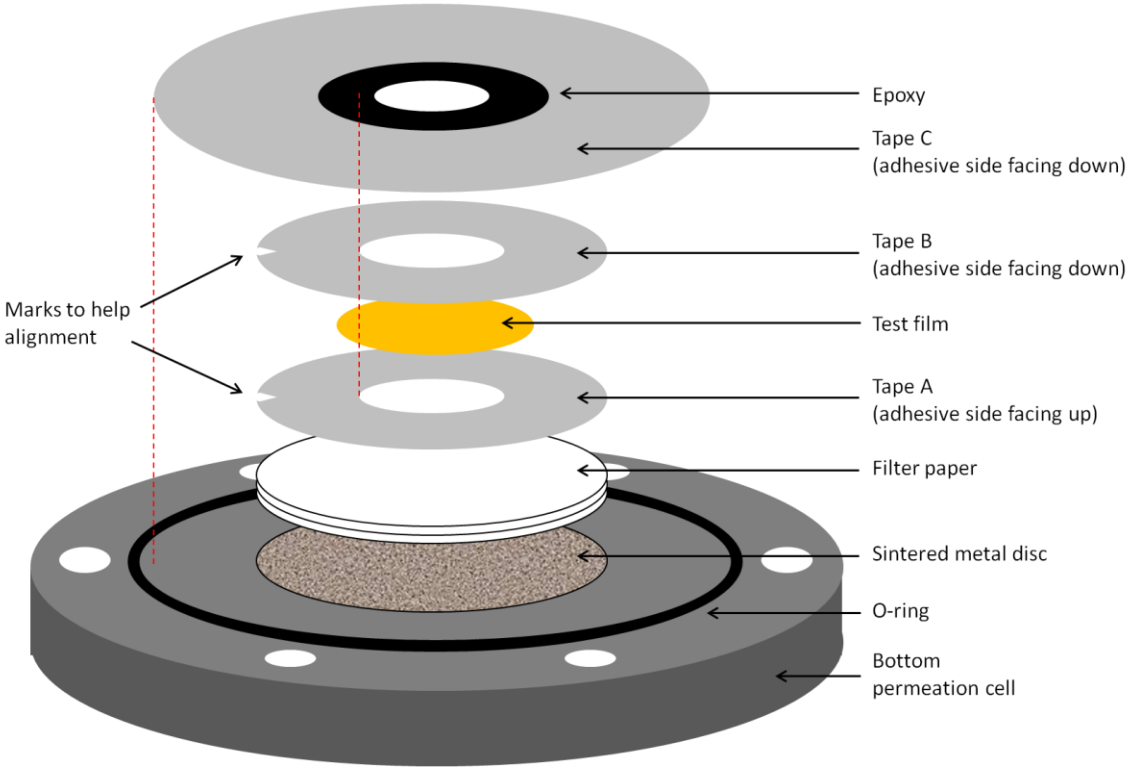

Figure 3.6: Schematic presentation of masking a dense film into permeation cell.

Due to the brittle nature, special cautions need to be taken for the masking of CMS dense films. CMS films pyrolyzed at higher temperature and from less permeable polymer precursors are usually more brittle and more difficult to hold flatness during pyrolysis. Special cautions to handle highly brittle CMS films include using smaller test area, using flat-head tweezers to pick up CMS films, and applying minimal pressure onto CMS film during the masking process.

3.4.1.2 Hollow Fiber Module Formation

The separation performance of CMS hollow fiber membranes were evaluated in lab scale fiber modules. The details of making hollow fiber module were described previously [7, 8]. One to three carbon fibers were used for each module. Five minute epoxy (3M, DP-100) was used to seal the ends of modules. Figure 3.7 shows the schematic of a lab-scale hollow fiber membrane module.

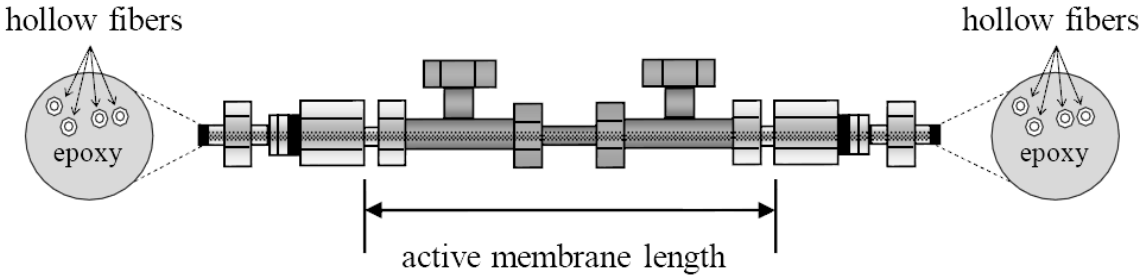

Figure 3.7: Schematic of lab-scale hollow fiber membrane module [9].

3.4.1.3 Constant-volume Permeation Test

Dense film permeation cell or hollow fiber module was loaded into the permeation box to evaluate the membrane separation properties. Figure 3.8 shows the schematic of a constant-volume permeation system with dense film permeation cell [10, 11]. For hollow fiber measurement, the permeation cell will be replaced by hollow fiber module. The shell side of module was connected to the upstream, and the bore side was connected to the downstream of the permeation system.

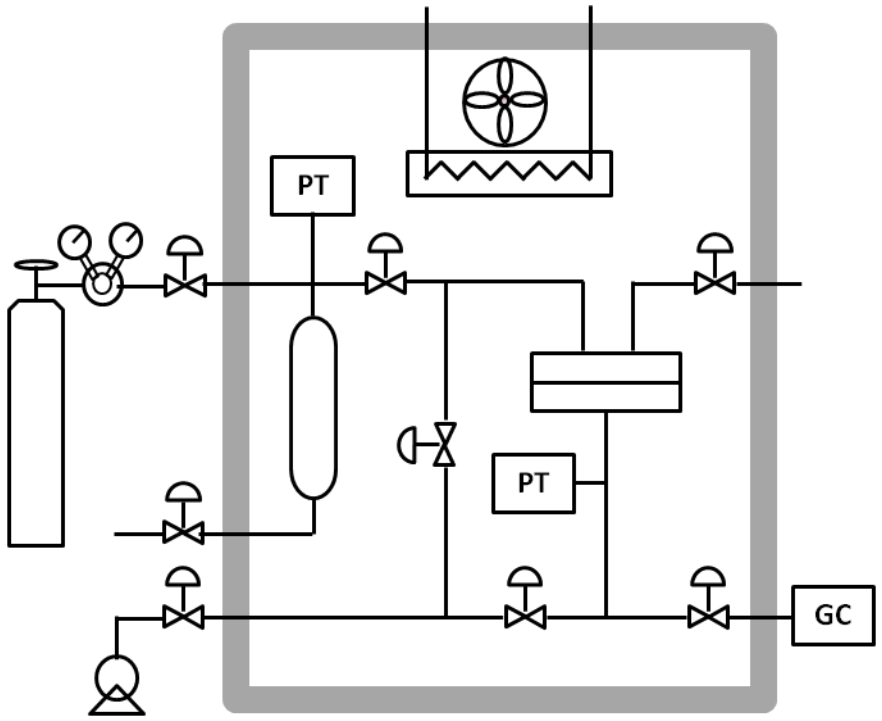

Figure 3.8: Schematic of constant-volume permeation system.

Before permeation test, both upstream and downstream were evacuated for over 24 hours and a leak rate was measured (<1% of the permeation rate). After evacuation and leak test, feed gas was introduced into the upstream from cylinder. For CMS membranes, the valves should be opened slowly to avoid sudden pressure change, which might result in film breaking. As feed gas permeates through the membrane, pressure rise in the constant-volume downstream can be observed. This downstream pressure change was recorded over time using LabVIEW (National Instruments, Austin, TX) until at least 6 times of time lag were reached. Permeability for dense film was calculated using the following equation:

$$P = \frac{(1.77 \times 10^{6}) \cdot \left(\frac{dp}{dt}\right) \cdot V \cdot l}{T \cdot A \cdot (\Delta p)} \tag{3.1}$$

where P is the permeability in Barrer, (dp/dt) is the downstream pressure change rate at steady state in torr/s, V is the downstream volume in cm^3, l is the membrane thickness in mils, T is the absolute temperature in permeation system in K, A is the film test area in cm^2, and Δp is the pressure difference between the upstream and downstream in psia.

For hollow fiber membranes, the permeance was calculated suing the following equation:

$$\frac{P}{l} = \frac{(2.46 \times 10^{7}) \cdot \left(\frac{dp}{dt}\right) \cdot V}{T \cdot OD \cdot L \cdot n \cdot (\Delta p)} \tag{3.2}$$

where (P/l) is the permeance in GPU, OD is the outer diameter of fiber, L is the active fiber length, n is the number of fibers in module. It should be noted that the downstream

volume *V* for dense film and hollow fiber in the same permeation system is different and should be measured individually.

A binary mixture of 20% N_2 and 80% CH_4 was used for mixed gas permeation measurement. The flow rate of feed stream over the membrane surface was controlled by a needle valve and measured by a digital flow-meter on the retentate side. The stage cut, which is the percentage of feed that permeates through the membrane, was maintained at <1% to avoid concentration polarization [12]. The downstream composition was determined using a gas chromatograph (Bruker 450-GC) with TCD detector during mixed gas permeation experiments. It should be noted that the N_2 content leaked from air should be deducted from the GC-measured N_2 concentration. The leaked N_2 content was determined by measuring O_2 concentration and converting it to N_2 concentration according to the O_2:N_2 ratio in air, as shown below.

$$N_2\%_{real} = N_2\%_{measured} - O_2\%_{measured} \times \frac{78}{21} \tag{3.3}$$

Between the permeation measurements of different gases, the system was pulled vacuum for at least 12 hours to have the membrane fully degassed.

3.4.2 Sorption Test

The sorption coefficients of CMS samples were measured by a pressure decay sorption system [13, 14]. CMS sample was crushed into small pieces between two pieces of weighing paper and loaded into a porous stainless steel filter (0.5 μm, Swagelok). This filter was wrapped with aluminum foil and a piece of copper wire to secure the CMS

samples inside the filter. The wrapped filter was degassed in a vacuum oven at 180 ℃ overnight to obtain accurate weight of the CMS sample. The sample was loaded into the sample cell which was then placed in an oil bath with temperature controller and circulator (Fisher Scientific Isotemp 2150) to maintain uniform temperature. The pressure decay sorption system is shown in Figure 3.9. The entire system was evacuated for 24 hour prior to testing.

For the measurement at each pressure level, the reservoir chamber was first charged with feed gas and allowed to wait for ~15 min to reach the testing temperature. Then the valve between the reservoir and sample cells was quickly opened and closed to introduce gas into the sample cell. The pressure in both reservoir and sample cells was monitored by pressure transducers and recorded over time by LabVIEW until the pressure became constant. The compressibility factors of the gases were calculated using National Institute of Standards and Technology (NIST) SUPERTRAPP program. Density and volume of the CMS sample was measure by a 25 mL pycnometer (KIMAX) with ethanol (≥99.8% purity, Sigma-Aldrich) as the liquid of precisely known density. With the acquired fugacity data and the known volume of sample/reservoir cells and CMS samples, a mole balance was used to calculate the amount of gas taken up by the CMS sample:

$$n_{total} = n_{res}^{i} + n_{sam}^{i} + n_{mem}^{i} = n_{res}^{f} + n_{sam}^{f} + n_{mem}^{f} \tag{3.4}$$

where n means the mole of gas existing in different environments; superscripts i and f mean initial state and final state, respectively; subscripts *res*, *sam* and *mem* mean reservoir cell, sample cell, and membrane.

Gas uptake was plotted against pressure and the data was fitted to Langmuir model to obtain sorption isotherms.

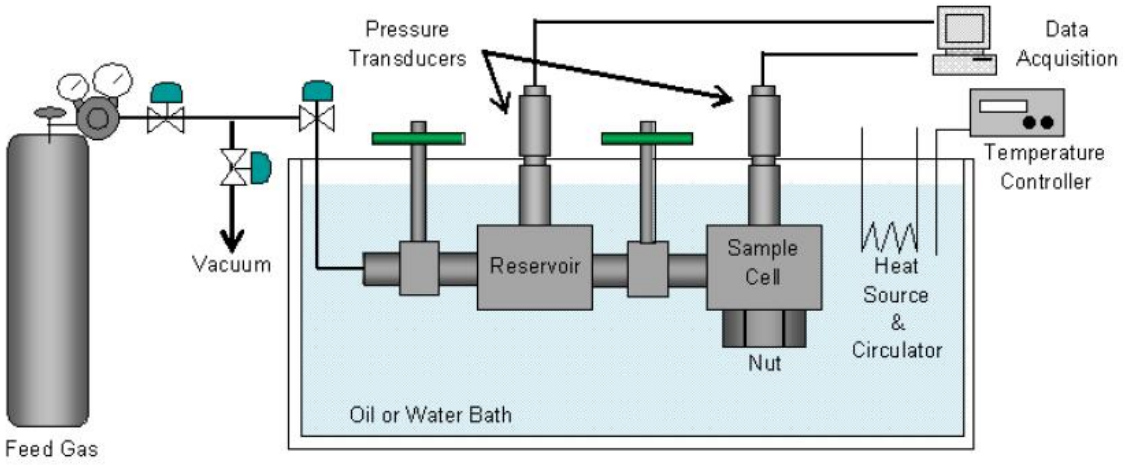

Figure 3.9: Schematic representation of the pressure decay sorption system.

3.4.3 Thermo-gravimetric Analysis (TGA)

TGA (Netzsch, STA 409 PC Luxx TGA/DSC) was performed to analyze the mass loss during pyrolysis and to determine the decomposition temperature (T_d) of polymers.

3.4.4 Differential Scanning Calorimetry (DSC)

DSC (Q200, TA Instruments) was performed to determine the glass transition temperature (T_g) of the polymers. Nitrogen flow of 50 mL/min and heating/cooling rate of 10 ℃ /min were used during analysis. Before running DSC characterization, TGA was performed to make sure the polymer would not decompose during the temperature protocol in DSC test.

3.4.5 Dense Film Bulk Density Measurement

The densities of polymer dense films were measure at 23 ℃ using a density gradient column (Techne, Burlington, NJ). Calcium nitrate solutions was prepared and filled into the 70 cm long column to form density gradient. Glass balls were used to calibrate the density gradient. Since the density of CMS film exceeds the measurement range of the density gradient column, CMS density was measured by a 25 mL pycnometer (KIMAX) with ethanol (≥99.8% purity, Sigma-Aldrich) as the liquid with known density.

3.4.6 Scanning Electron Microscopy (SEM)

SEM (LEO 1530 and LEO 1550) was used to characterize the morphology of asymmetric hollow fibers. For polymer fibers, the fibers were soaked in hexane and then shear fractured in liquid nitrogen to preserve the cross-sectional morphology. All fibers were coated with gold before SEM.

3.4.7 Elemental Analysis

Elemental analysis was performed by ALS labs, Tuscon, AZ. The samples were dried at 150 ℃ and bench ground into fine powder before analysis. The C, H and N wt% were measured by combustion/TC and IR detection. The O wt% was measured by pyrolysis/IR detection. The F wt% was measured by bomb and oxygen flask combustion/ion chromatography.

3.5 References

[1] Burgess SK, Leisen JE, Kraftschik BE, Mubarak CR, Kriegel RM, Koros WJ. Chain mobility, thermal, and mechanical properties of poly (ethylene furanoate) compared to poly (ethylene terephthalate). Macromolecules 2014.

[2] Lee JS, Leisen J, Choudhury RP, Kriegel RM, Beckham HW, Koros WJ. Antiplasticization-based enhancement of poly (ethylene terephthalate) barrier properties. Polymer 2012;53(1):213-22.

[3] Bhuwania N. Engineering the morphologhy of carbon molecular sieve (cms) hollow fiber membranes. Atlanta: Georgia Institute of Technology; 2013.

[4] Kiyono M, Williams PJ, Koros WJ. Effect of pyrolysis atmosphere on separation performance of carbon molecular sieve membranes. J Membr Sci 2010;359(1–2):2-10.

[5] Rungta M. Carbon molecular sieve dense film membranes for ethylene/ethane separations. Atlanta: Georgia Institute of Technology; 2012.

[6] Rungta M, Xu L, Koros WJ. Carbon molecular sieve dense film membranes derived from matrimid® for ethylene/ethane separation. Carbon 2012;50(4):1488-502.

[7] Vu DQ, Koros WJ, Miller SJ. High pressure co2/ch4 separation using carbon molecular sieve hollow fiber membranes. Ind Eng Chem Res 2002;41(3):367-80.

[8] Kosuri MR, Koros WJ. Defect-free asymmetric hollow fiber membranes from torlon< sup>®</sup>, a polyamide–imide polymer, for high-pressure co< sub> 2</sub> separations. J Membr Sci 2008;320(1):65-72.

[9] Xu L. Carbon molecular sieve hollow fiber membranes for olefin/paraffin separations. Atlanta: Georgia Institute of Technology; 2012.

[10] Pye D, Hoehn H, Panar M. Measurement of gas permeability of polymers. I. Permeabilities in constant volume/variable pressure apparatus. J Appl Polym Sci 1976;20(7):1921-31.

[11] Pye D, Hoehn H, Panar M. Measurement of gas permeability of polymers. Ii. Apparatus for determination of permeabilities of mixed gases and vapors. J Appl Polym Sci 1976;20(2):287-301.

[12] Baker RW. Membrane technology and applications. New York: McGraw-Hill; 2000.

[13] Koros WJ, Paul DR. Design considerations for measurement of gas sorption in polymers by pressure decay. Journal of Polymer Science: Polymer Physics Edition 1976;14(10):1903-7.

[14] Costello LM, Koros WJ. Temperature dependence of gas sorption and transport properties in polymers: Measurement and applications. Ind Eng Chem Res 1992;31(12):2708-14.

CHAPTER 4

EFFECTS OF PYROLYSIS CONDITIONS ON CMS MEMBRANES FOR N_2/CH_4 SEPARATION

4.1 Overview

Although carbon molecular sieve (CMS) membranes have shown attractive separation performance for a wide range of gas separations, membrane properties need to be tailored and optimized for different gas pairs. Dramatic differences in diffusion coefficients can occur for molecules with even subtle size and shape differences in such CMS materials. While a particular optimized pyrolysis condition may be suitable for one gas pair, it may give poor separation performance for another gas pair for the same polymer precursor.

The effects of pyrolysis temperature protocol and pyrolysis atmosphere have been well studied for gas pairs including O_2/N_2, CO_2/CH_4, C_2H_4/C_2H_6, and C_3H_6/C_3H_8 [1-4], but not for the N_2/CH_4 pair. Two available polymers, therefore, Matrimid® and 6FDA:BPDA-DAM were chosen to study the effects of pyrolysis temperature, soak time, oxygen doping, and hydrogen doping for N_2/CH_4 separation. These two precursors were selected because of their good separation performance for many other gas pairs and good processability into both dense film and hollow fiber morphologies.

4.2 Carbon Molecular Sieve Membranes Derived from 6FDA:BPDA-DAM

6FDA:BPDA-DAM is a preferred precursor for many gas pairs due to its high flux and good asymmetry in the hollow fiber morphology even after pyrolysis. Optimization of the pyrolysis conditions for N_2/CH_4 separation using CMS membranes derived from 6FDA:BPDA-DAM is presented in this section. Permeation measurements were made at 35 ℃ and 65 psia feed pressure for pure gas, and 100 psia feed pressure for 20% N_2/80% CH_4 mixed gas. The results of this study are summarized below.

4.2.1 Effect of Pyrolysis Temperature on Separation Performance

6FDA:BPDA-DAM dense films were pyrolyzed under UHP Ar at two final pyrolysis temperatures of 550 ℃ and 800 ℃ using the protocols described in Chapter 3. The permeation results are presented in Figure 4.1. Results showed that both CMS membranes provided better separation performance than the polymer precursor, and the increase in pyrolysis temperature led to an increase in N_2/CH_4 selectivity and a decrease in N_2 permeability. The more than 10 fold N_2 permeability increase from precursor to 550 ℃ pyrolyzed CMS reflects the creation of micropores during pyrolysis. As discussed in Chapter 2, the micropores in CMS provide higher Langmuir sorption volume and promote longer diffusion jump compared to polymer membranes. As pyrolysis temperature increased from 550 ℃ to 800 ℃, the average sizes of both micropores and ultramicropores were reduced due to a general tightening of the micropore and ultramicropore structure shown in Figure 2.3, resulting in decreased permeabilities and increased N_2/CH_4 selectivity. While 550 ℃ and 800 ℃ pyrolyzed 6FDA:BPDA-DAM

CMS membranes were shown to provide good separation performance above the upper bound line for several other gas pairs [5, 6], the separation performance for N_2/CH_4 with a selectivity below 2 is far from satisfying. The results reflect the small size difference between N_2 and CH_4 (3.64 Å vs. 3.80 Å) and the relatively open micropore and ultramicropore structure in 6FDA:BPDA-DAM derived CMS membranes. The bulky CF_3 groups in 6FDA:BPDA-DAM not only increase the free volume in the polymer precursor, but also prevents dense packing of the final carbon structure as they leave the polymer chain during the pyrolysis process. The resulting open CMS structure cannot provide effective discrimination of the subtle size and shape difference between N_2 and CH_4. When this poor diffusion selection effect is further offset by the adverse sorption selection effect, only low overall N_2/CH_4 permselectivity can be achieved.

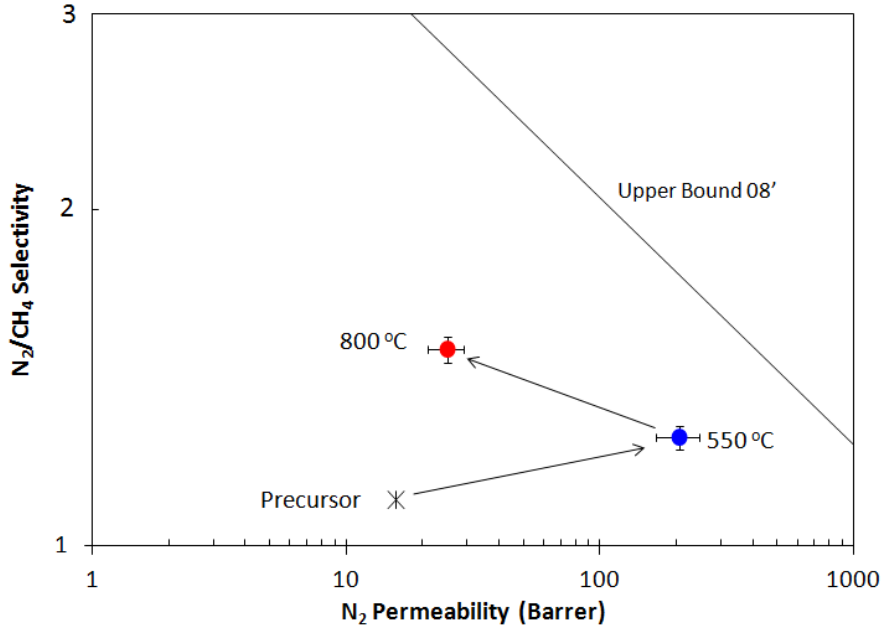

Figure 4.1: Plot showing N_2/CH_4 separation performance (35 ℃, 65 psia) of CMS dense films pyrolyzed from 6FDA:BPDA-DAM at 550 ℃ and 800 ℃ for 2 hour soak time under UHP Ar. Error bars represent standard deviations from multiple measurements.

4.2.2 Effect of Soak Time on Separation Performance

To improve the N_2/CH_4 selectivity of 6FDA:BPDA-DAM derived CMS membranes, a longer soak time of 8 hour at the final pyrolysis temperature was used. Longer soak time promotes a general tightening of the pore structure. The permeation properties of 6FDA:BPDA-DAM CMS membranes pyrolyzed under UHP Ar at 550 ℃ and 800 ℃ with 8 hour soak time are presented in Figure 4.2, with comparison to those soaked for 2 hour. A large reduction in permeability but small change in N_2/CH_4 selectivity was observed. It is hypothesized that the carbon structure consolidation happens mostly in the relatively larger micropores under longer soak time; while the size discriminating ultramicropores do not show much favorable changes due to longer soak time.

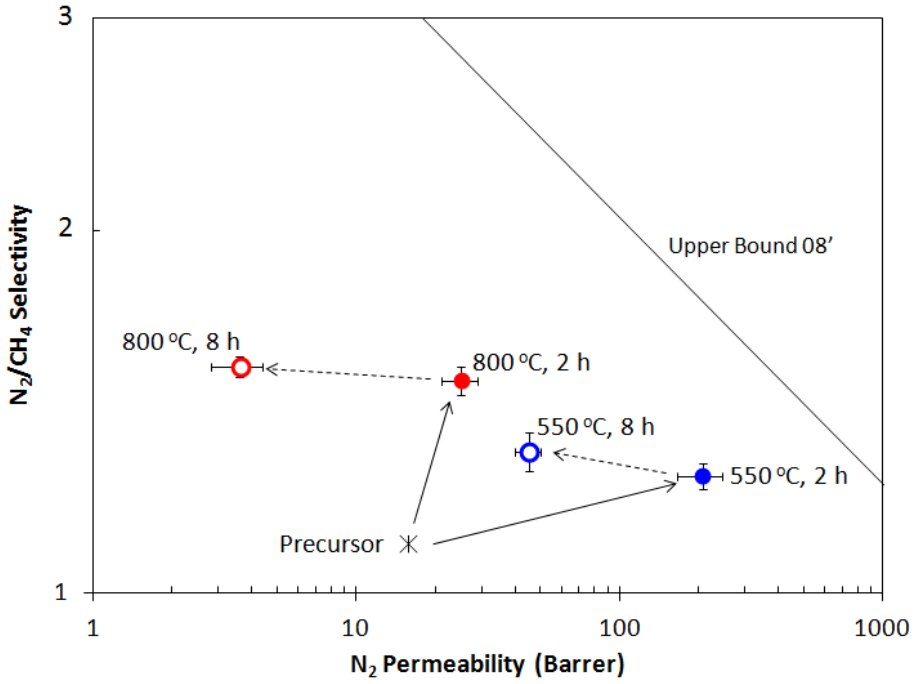

Figure 4.2: Plot showing N_2/CH_4 separation performance (35 ℃, 65 psia) of CMS dense films pyrolyzed from 6FDA:BPDA-DAM at 550 ℃ and 800 ℃ for 2 hour and 8 hour soak time under UHP Ar. Error bars represent standard deviations from multiple measurements.

4.2.3 Effect of Oxygen Doping

As discussed in Chapter 2, oxygen in the pyrolysis atmosphere can selectively chemisorb onto the edges of ultramicropores during pyrolysis and fine-tune the pore structure (Figure 2.5). Such method has been successfully developed by Kiyono et al. for optimizing the separation performance of CO_2/CH_4 for 6FDA:BPDA-DAM CMS [7].

Oxygen doping using 10, 17, and 53 ppm O_2 with balance Ar purge gas was applied at 800 ℃ and 900 ℃ pyrolysis temperatures for 6FDA:BPDA-DAM. During the 900 ℃ pyrolysis, it was observed that there was a 35 ℃ overshoot when the furnace was approaching the final pyrolysis temperature, which did not happen for other lower pyrolysis temperatures. This indicates that the furnace could not provide a good temperature control at the high temperature of 900 ℃. As a result, pyrolysis at above 800 ℃ was not performed in the following study. The permeation results of the oxygen-doped CMS dense films are shown in Figure 4.3.

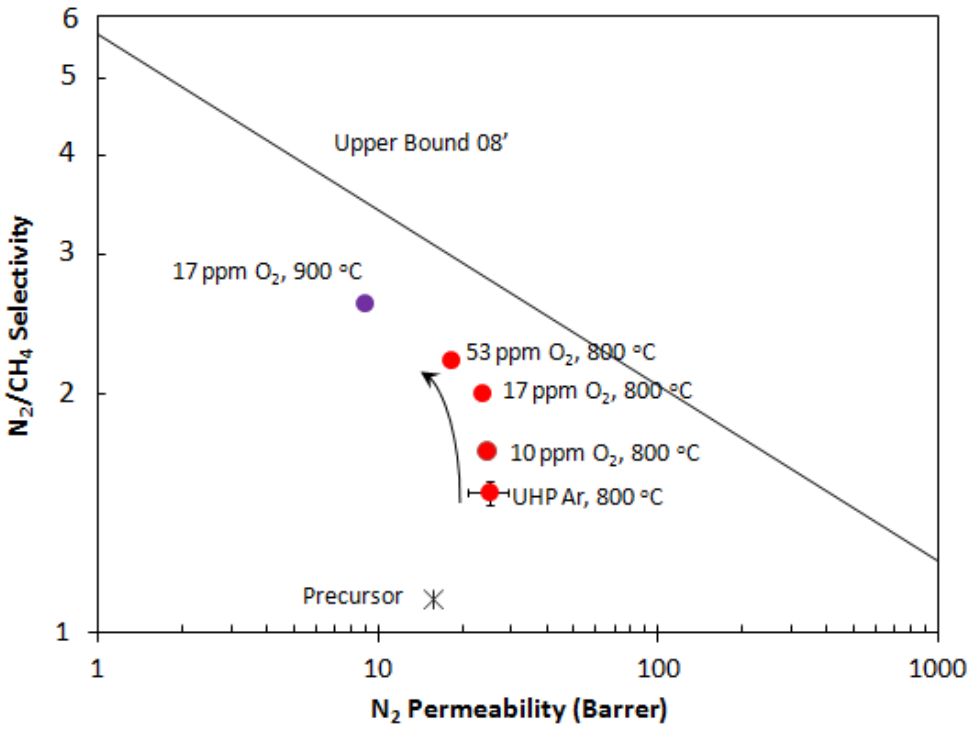

Figure 4.3: Effect of oxygen doping on N_2/CH_4 permeation (35 ℃, 65 psia) for 6FDA:BPDA-DAM CMS dense films.

The permeation results of 800 ℃ pyrolyzed 6FDA:BPDA-DAM CMS membranes show that as oxygen level increased from below 1 ppm (UHP Ar) to 53 ppm, N_2/CH_4 selectivity increased by 47% (from 1.5 to 2.2) while N_2 permeability decreased only 27% (from 25 to 18.2 Barrer). On the other hand, when oxygen level was controlled at 17 ppm, as the pyrolysis temperature increased from 800 ℃ to 900 ℃, N_2/CH_4 selectivity increased by 30% (from 2.0 to 2.6) while N_2 permeability decreased by 62% (from 23.6 to 8.9 Barrer). Comparing these two effects of pyrolysis temperature and oxygen level for 6FDA:BPDA-DAM CMS membranes, it can be concluded that while both factors can be used to improve the N_2/CH_4 selectivity, the oxygen doping method results in much less reduction in N_2 permeability. This is presumably mainly because of

the selective reaction of oxygen at the ultramicropore windows. The boundaries of ultramicropores in CMS are believed to be formed by the edges of carbon lamellae, while the boundaries of micropores are mainly formed by the carbon basal planes. It has been estimated that the chemi-sorption at the edges of carbon lamellae is ~17 times more reactive than that at the carbon basal planes [8]. Thus the oxygen doping is considered to be mainly happening at the ultramicropore windows, as shown in Figure 4.4. As a result, the overall carbon structure does not condense and the micropore volume remains while the ultramicropores are tighten by adding a layer of oxygen atom. The decrease of ultramicropore window size improves the discrimination of gas penetrant size and shape difference and leads to enhanced selectivity and reduced permeability. However, since the sorption cavities or the micropores remain largely unchanged, so the decrease in permeability is not significant. On the other hand, the increase of pyrolysis temperature results in an extensive condensation of the overall carbon structure, as shown in Figure 4.4. Thus the sizes of both ultramicropores and micropores are reduced, leading to an increase in selectivity accompanied by a significant decrease in permeability.

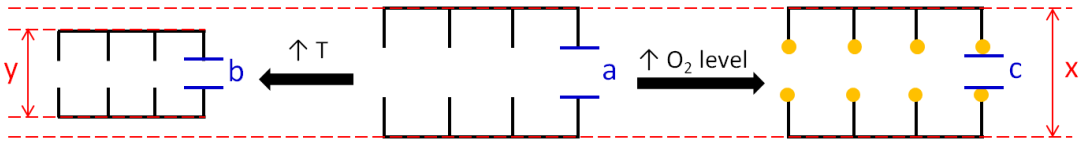

Figure 4.4: Schematic representation of the effects of final pyrolysis temperature and oxygen doping on 6FDA:BPDA-DAM CMS pore structure.

It should be noted that while the oxygen doping method was proved to be effective for selective tightening the ultramicropores in 6FDA:BPDA-DAM CMS membranes, the N_2/CH_4 separation performance obtained from such treatment is still below the upper bound line. With the N_2/CH_4 selectivity below 3, the pore structure of 6FDA:BPDA-DAM CMS membranes is, therefore, considered to be too open for such similar-sized N_2/CH_4 gas pair.

4.2.4 Pure Gas vs. Mixed Gas Performance

The 550 ℃ and 800 ℃ pyrolyzed 6FDA:BPDA-DAM CMS membranes with 2 hour soak time were tested with a most demanding case of 20% N_2/80% CH_4 mixed gas feed. The total feed gas pressure was 100 psia and the stage cut was maintained at <1%. The steady state mixed gas permeation results together with pure gas permeation results are shown in Figure 4.5. It is seen that both the permeabilities and N_2/CH_4 mixed gas selectivity (or separation factor) were lower than the pure permeation data. This is because that competition between the two gas penetrants slows down the permeation of both, leading to lower permeabilities. At the same time, CH_4 takes advantage of its stronger sorption effect in the competition and occupies sorption sites available to N_2 under pure gas condition, resulting in a lower N_2/CH_4 mixed gas selectivity.

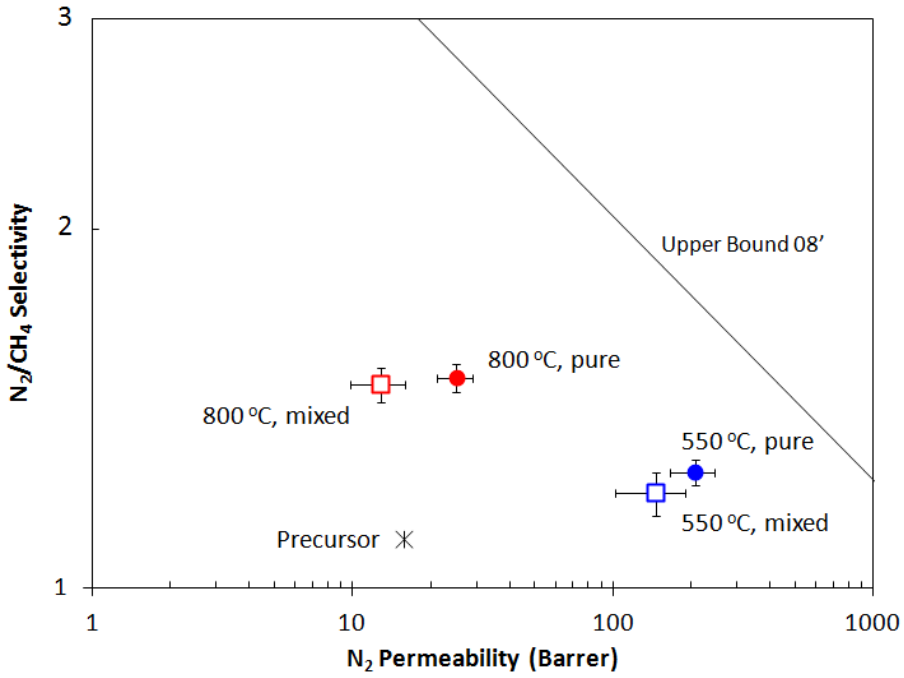

Figure 4.5: Mixed and pure gas permeation results of 550 ℃ and 800 ℃ pyrolyzed 6FDA:BPDA-DAM CMS membranes with 2 hour soak time. Error bars represent standard deviations from multiple measurements.

4.3 Carbon Molecular Sieve Membranes Derived from Matrimid®

Since 6FDA:BPDA-DAM CMS membranes did not show attractive separation performance, even with high pyrolysis temperature and oxygen doping, a more densely packed polymer precursor Matrimid® was studied for N_2/CH_4 separation. Matrimid® has lower fractional free volume (0.139 vs. 0.151 for 6FDA:BPDA-DAM) and does not have the bulky CF_3 groups compared to 6FDA:BPDA-DAM. These two facts lead to more condensed carbon structure after pyrolysis for Matrimid®. Previous studies on other gas pairs have shown that Matrimid® CMS membranes usually provide higher selectivity but

lower permeability than 6FDA:BPDA-DAM CMS membranes [5, 6]. It was also observed in the current study that CMS dense films derived from Matrimid® are usually more brittle and more prone to curl slightly compared to those derived from 6FDA:BPDA-DAM, especially at high pyrolysis temperatures. More attention needs to be paid during masking and permeation test to avoid the breakage of film samples. Special cautions regarding masking and permeation testing brittle CMS dense films were described in Chapter 3.

4.3.1 Effect of Pyrolysis Temperature on Separation Performance

Matrimid® dense films were pyrolyzed under UHP Ar at three final pyrolysis temperatures of 550, 675, and 800 ℃, following the temperature protocol described in Chapter 3. Pure N_2 and CH_4 permeation tests were performed at 35 ℃ and 65 psia feed pressure for both Matrimid® precursor and the resulting CMS dense films. The N_2 permeability and N_2/CH_4 permselectivity are plotted on the so-called N_2/CH_4 upper bound [9] in Figure 4.6. As seen from Figure 4.6, all CMS films performed much better than the polymer precursor, providing higher N_2 permeability and higher N_2/CH_4 permselectivity at the same time.

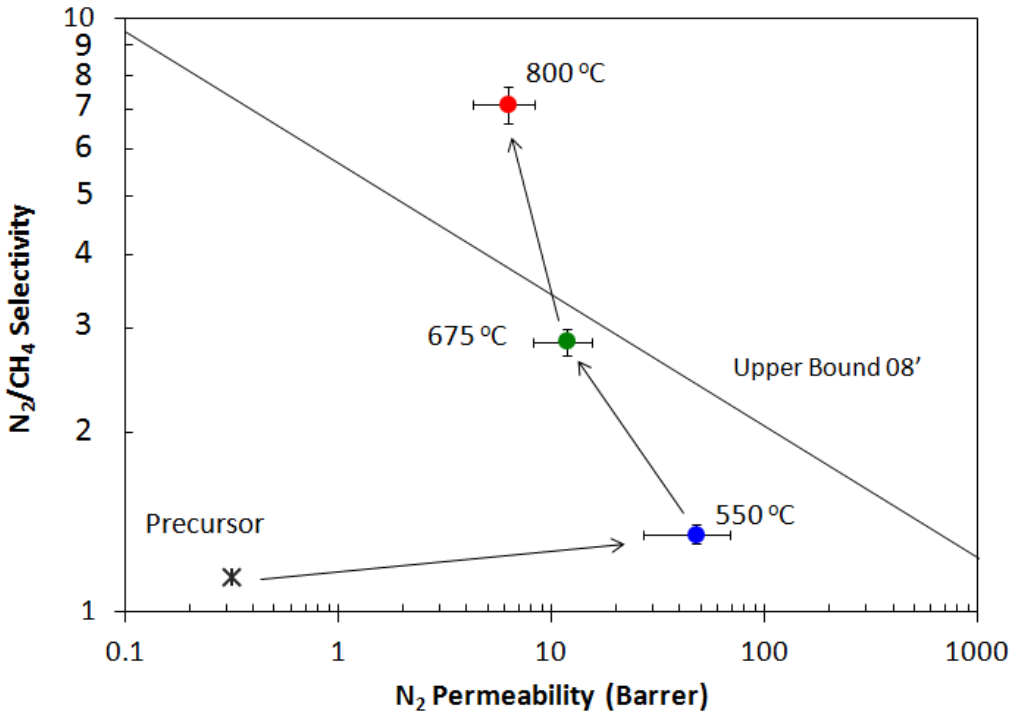

Figure 4.6: N_2/CH_4 permeation results (35 ℃, 65 psia pure gas feed) of Matrimid® CMS dense films pyrolyzed at 550, 675, and 800 ℃ and soaked for 2 hour. Error bars represent standard deviations from multiple measurements.

As expected, as pyrolysis temperature increases, permeability decreases while N_2/CH_4 permselectivity increases. This can be qualitatively explained by the hypothetical ultramicropore size distribution curve (Figure 4.7) proposed by Steel and Koros [2, 10]. A given gas penetrant has free diffusive access to all inter-connected pores that are longer than its characteristic size. In Figure 4.7, the number of these accessible pores is represented as the area under the distribution curve and to the right of the line of this penetrant. The area ratio in the plot for the two gas penetrants represents the diffusion selectivity. As final pyrolysis temperature increases, CMS structure starts to be more tightly packed, resulting in the ultramicropore distribution shifting to the lower size end [2]. As a result, the diffusion coefficient and permeability of both penetrants decrease, but

N_2/CH_4 diffusion selectivity and permselectivity increase since the loss in pore access is relatively less for the 'slimmer' N_2 vs. CH_4.

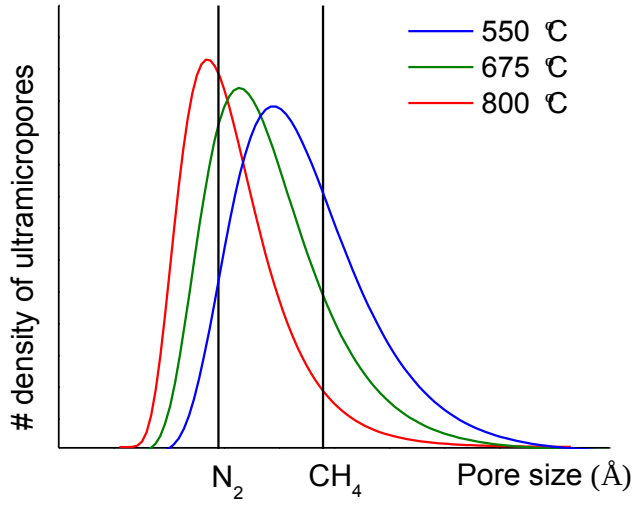

Figure 4.7: Idealized hypothetical ultramicropore size distribution for CMS membranes pyrolyzed at three final pyrolysis temperatures.

The 800 ℃ CMS membrane provides an attractive combination of N_2 permeability and N_2/CH_4 permselectivity that exceeds the polymer-based upper bound line. More detailed studies of this high performing CMS membrane regarding the diffusion selection effect and entropic factor in the diffusion selectivity were performed and will be discussed in later sections in this chapter. It should be noticed that such a high pyrolysis temperature is essential to effectively separate N_2 and CH_4. For other less demanding gas pairs like O_2/N_2, CO_2/CH_4, C_2H_4/C_2H_6, and C_3H_6/C_3H_8, lower pyrolysis temperatures of 675 ℃ and 550 ℃ are adequate [1, 10]; however, the lower final pyrolysis temperatures give poor separation performance for highly size-similar N_2/CH_4 pair. The tradeoff between diffusion selectivity from the relatively small size difference

of N_2 and CH_4 (kinetic diameter 3.64 vs. 3.80 Å) and the N_2 permeability does not become attractive until the ultramicropores are tightened at the high pyrolysis temperature.

The 675 ℃ and 800 ℃ pyrolyzed Matrimid® CMS dense films were also tested for O_2 and CO_2 permeation at 35 ℃ with 65 psia feed pressure. The results are summarized in Table 4.1. These data provide useful reference for other applications with the studied membrane materials. They also suggest that most other gas pairs including O_2/N_2, CO_2/CH_4 and CO_2/N_2 are easier to separate than N_2/CH_4. For the natural gas processing application considered in this study, CO_2 removal from CH_4 is also involved during upgrading. While CO_2 is usually removed by amine absorption, there is a great potential to save this separate CO_2 removal unit if nitrogen rejection is achieved by N_2-selective membrane. As both N_2 (3.64 Å) and CO_2 (3.3 Å) are smaller than CH_4 (3.8 Å), they can be enriched in the permeate stream at the same time, leaving upgraded CH_4 in the retentate stream.

Table 4.1: Permeabilities and selectivities of Matrimid® CMS dense films pyrolyzed at 675 ℃ and 800 ℃ and soaked for 2 hour under UHP Ar. Tests were conducted at 35 ℃ with 65 psia feed pressure.

	Permeability (Barrer)				Selectivity			
	N_2	CH_4	O_2	CO_2	N_2/CH_4	O_2/N_2	CO_2/CH_4	CO_2/N_2
675 ℃	15.3	4.23	110	318	3.6	7.2	75	21
800 ℃	6.78	0.88	66.1	220	7.7	9.8	250	33

4.3.2 Effect of Hydrogen Doping

While oxygen doping method was proved to be effective for less densely packed polymer precursors like 6FDA:BPDA-DAM, it has been shown that applying oxygen doping to more densely packed intrinsic structure of carbon should be avoided. Kiyono has shown that increasing oxygen level from 1 ppm to 100 ppm in the pyrolysis atmosphere for 550 ℃ pyrolyzed Matrimid® resulted in monotonic decrease in both CO_2 permeability and CO_2/CH_4 selectivity, as shown in Figure 4.8.

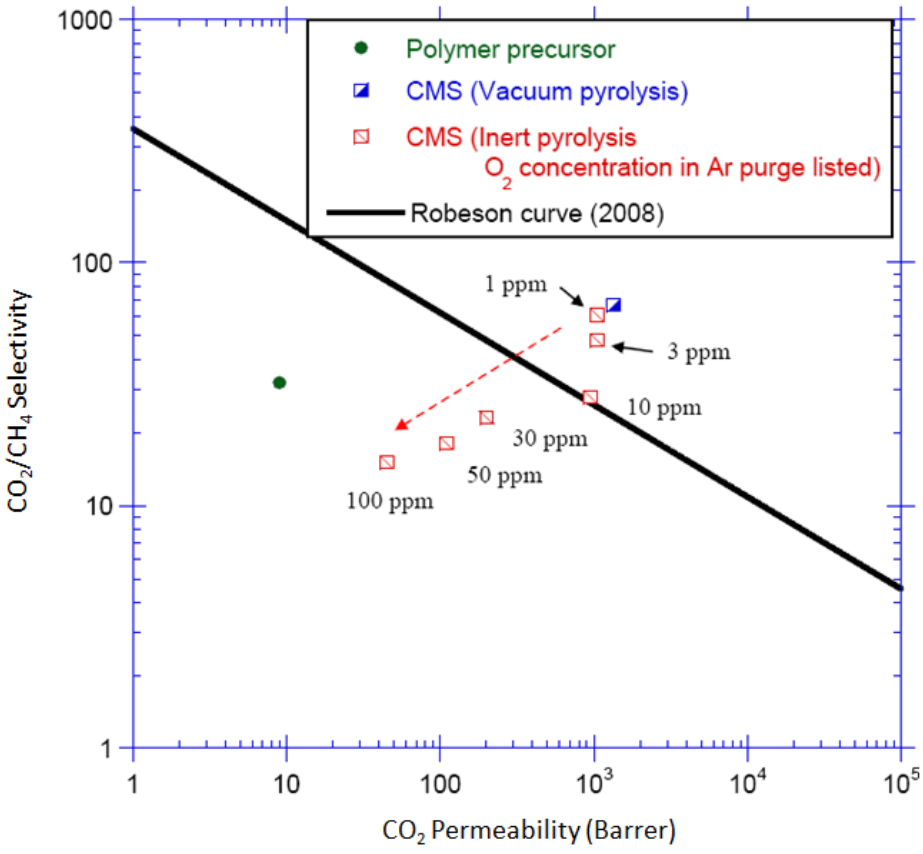

Figure 4.8: Oxygen doping effect on 550 ℃ pyrolyzed Matrimid® for CO_2/CH_4 [7].

Such phenomena suggest that the oxygen is "clogging" the already tight structure of ultramicropores, as shown in Figure 4.9. The clogging not only reduces the ultramicropores accessible to the relatively larger CH_4, but also may lead to the block of a large amount of ultramicropores that were accessible to the smaller CO_2. As a result, no enhancement of selectivity is observed, but a significant loss in the permeabilities of both penetrants is observed. Since N_2 has a much larger kinetic diameter than CO_2 (3.64 vs. 3.3 Å), it is expected that the clogging will also reduce a large amount of ultramicropores that were accessible to N_2, resulting in decrease in both N_2 permeability and N_2/CH_4 selectivity for 550 ℃ and higher temperature pyrolyzed Matrimid® CMS membranes. So the oxygen-doping method was not considered to enhance the N_2/CH_4 separation performance for Matrimid® derived CMS membranes.

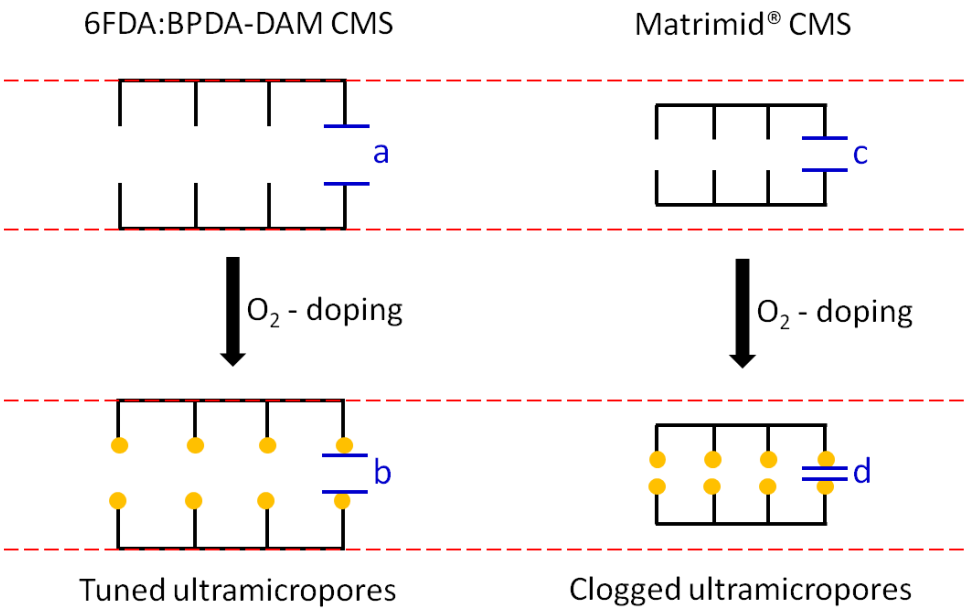

Figure 4.9: Schematic representation of the oxygen doping effects on the pore structure of 6FDA:BPDA-DAM and Matrimid® derived CMS membranes.

Instead of O_2-doping, H_2-doping was considered for pore structure improvement for Matrimid® CMS membranes, since the atomic radius of H is much smaller than that of O (0.25 Å vs. 0.60 Å [11]). It is hypothesized that like oxygen, hydrogen might react and bind to the reactive edges of carbon lamellae that form the ultramicropores and finely tune the ultramicropore size. Previous study showed that H_2 starts to leave the polymer matrix at ~520 ℃ during the carbonization of polyimides films, as shown in Figure 4.10 [12]. To replace some hydrogen, H_2-doping was pursued as a post treatment at lower temperature of 500 ℃, instead of the simultaneous doping and pyrolyzing method used for the O_2-doping of 6FDA:BPDA-DAM. The heating protocol listed below was used for post H_2-doping after the standard heating protocol under UHP Ar was completed and the furnace was naturally cooled down to 50 ℃. The purging gas used for post H_2-doping was 1000 ppm H_2 with balance Ar.

(1) 50 → 250 ℃ at a ramp rate of 13.3 ℃/min.

(2) 250 ℃ → 485 ℃ at a ramp rate of 3.85 ℃/min.

(3) 485 ℃ → 500 ℃ at a ramp rate of 0.25 ℃/min.

(4) Soak at 500 ℃ for 2 hour.

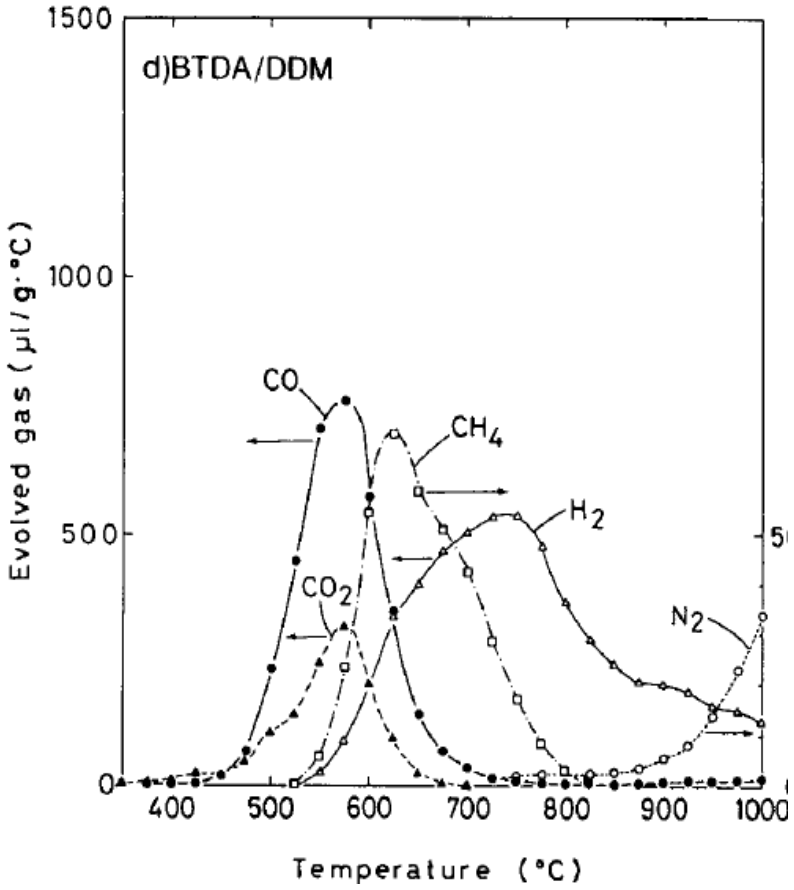

Figure 4.10: Changes of decomposition gases during the carbonization process of polyimide [12].

The permeation results of post H_2-doped Matrimid® CMS dense films pyrolyzed at 550, 675, and 800 ℃ are shown in Figure 4.11, with comparison to the undoped CMS dense films. It is concluded that the influence of post H_2-doping on N_2 permeability and N_2/CH_4 selecitivity is not significant beyond experimental error. It is hypothesized that the weaker pore-tuning capability of H_2-doping compared to O_2-doping is not only because of the smaller size of hydrogen, but also because of the less intrinsic chemisorption tendency of hydrogen versus that of oxygen at the reactive edges. Previous

study showed that the amount of hydrogen adsorbed on carbon was much less than the amount of oxygen at the same pressure and temperature [13, 14].

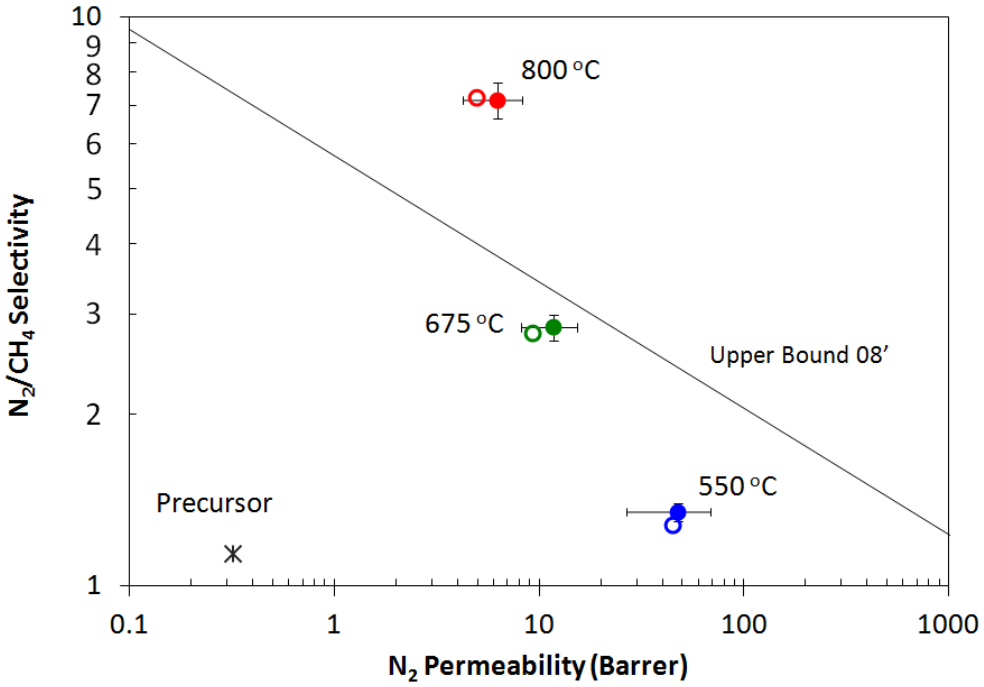

Figure 4.11: N_2/CH_4 permeation results (35 ℃, 65 psia pure gas feed) of Matrimid® derived CMS dense films pyrolyzed at 550, 675, and 800 ℃ under UHP Ar with and without post H_2-doping. Solid circles represent CMS membranes without post H_2-doping, and open circles represent CMS membranes with post H_2-doping.

4.3.3 Deconvolution of the Sorption and Diffusion Effects in Permeation

Sorption measurements were performed on the 800 ℃ pyrolyzed Matrimid® CMS dense film to deconvolute the sorption and diffusion effects from permeation. Figure 4.12 shows the sorption isotherms of 800 ℃ pyrolyzed Matrimid® CMS dense film at 35 ℃. Sorption coefficients S_{N2} and S_{CH4} at 35 ℃ and 65 psia were calculated using Eq. (2.14) based on the concentration of sorbed penetrants shown in Figure 4.12. The N_2

permeability, sorption coefficient, diffusion coefficient and corresponding N_2/CH_4 selectivities of Matrimid® precursor and 800 ℃ pyrolyzed CMS dense film are listed in Table 4.2. From these data, it can be concluded that the improvement of N_2 permeability after pyrolysis mainly results from the increase of N_2 sorption coefficients. On the other hand, the higher N_2/CH_4 permselectivity is solely contributed by a high diffusion selectivity of 15.1, while the sorption selectivity of 0.51 gives negative contribution to the permselectivity. This conclusion is consistent with the unique structure of CMS membranes -- micropores provide high sorption coefficients and high permeability, while ultramicropores function as molecular sieving sites to give high diffusion selectivity and permselectivity.

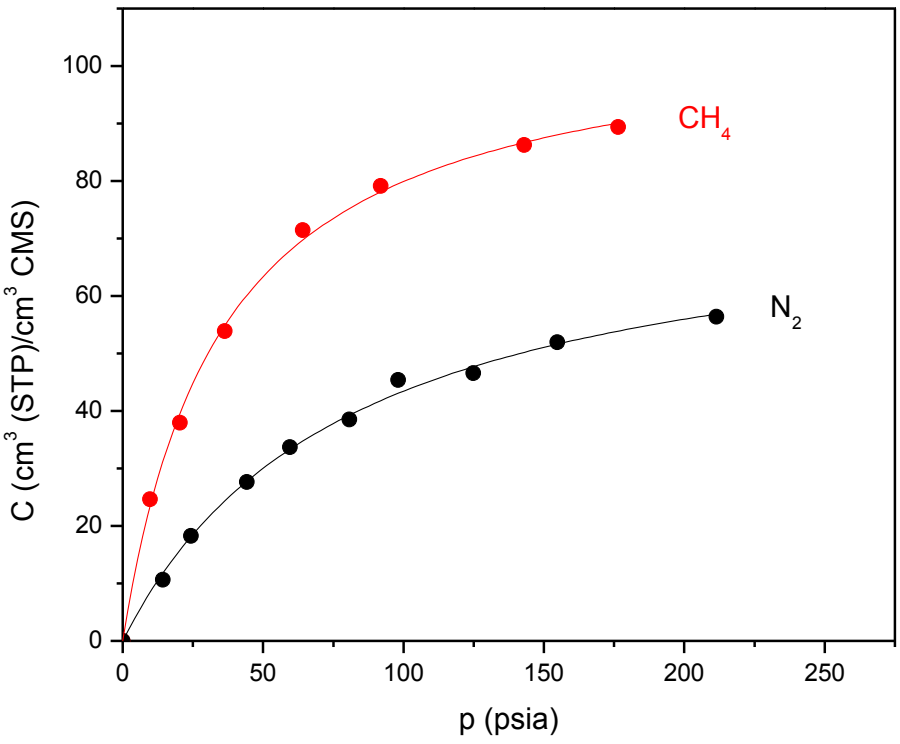

Figure 4.12: N_2 and CH_4 sorption isotherms of 800 ℃ Matrimid® CMS dense film, measured at 35 ℃.

Table 4.2: Permeabilities, sorption and diffusion coefficients of Matrimid® polymer dense film and 800 ℃ pyrolyzed CMS dense film.

	Matrimid®	CMS_800 ℃
P_{N_2} (Barrer)	0.32	6.78
D_{N_2} (10^{-8} cm^2/s)	0.662	0.619
S_{N_2} (cm^3 (STP)/cm^3 CMS/psi)	0.025 [15]	0.566
P_{N_2} / P_{CH_4}	1.14	7.69
S_{N_2} / S_{CH_4}	0.37	0.50
D_{N_2} / D_{CH_4}	3.05	15.3

Sorption isotherm parameters were measured at 35 ℃. Permeabilities, sorption coefficients, diffusion coefficients, and selectivities are based on 35 ℃, 65 psia. The sorption coefficients of Matrimid® precursor were obtained from literature [15].

4.3.4 Temperature Effect of Gas Transport in CMS Membranes

4.3.4.1 Temperature Effect on Permeation

The temperature dependence of permeabilities and permselectivity of the 800 ℃ pyrolyzed Matrimid® CMS sample were studied over the permeation test range of 25-50 ℃ at 65 psia upstream pressure. Permeabilities, permselectivities and Arrhenius parameters in for the temperature range between 25-50 ℃ are reported in Table 4.4, with the least squares fitting plot shown in Figure 4.13. The error analysis was done following previously described method [16]. Results show that the permeabilities of both N_2 and CH_4 increase with permeation temperature; however, the larger CH_4 penetrant shows stronger temperature dependency with higher permeation activation energy, so N_2/CH_4 permselectivity decreases with temperature.

Table 4.3: Permeation properties of 800 ℃ Matrimid® CMS membrane at 65 psia.

		N_2	CH_4
P (Barrer)	25 ℃	5.62	0.68
	35 ℃	6.78	0.88
	50 ℃	8.98	1.19
E_p (kJ/mol)	-	15.0 ± 0.3	17.7 ± 1.0
P_0 (Barrer)	-	$(2.40 \pm 0.31) \times 10^3$	$(8.83 \pm 3.40) \times 10^2$
P_{N2} / P_{CH4}	25 ℃	8.27	
	35 ℃	7.69	
	50 ℃	7.57	

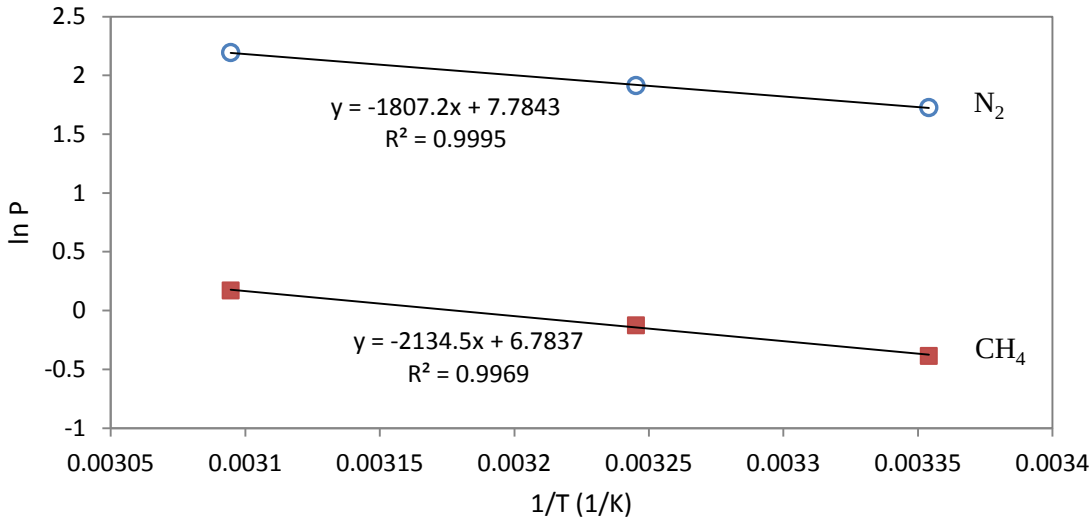

Figure 4.13: Temperature dependence of permeabilities of 800 ℃ Matrimid® CMS membrane at 65 psia (permeability P is in the unit of Barrer).

The temperature effect on other gas penetrant permeation was analyzed for both 675 ℃ and 800 ℃ pyrolyzed Matrimid® CMS dense films. The permeation results of N_2, CH_4, O_2 and CO_2 tested at 25 ℃, 35 ℃ and 50 ℃ are summarized in Table 4.4 and Table 4.5. These results show that as expected, the permeabilities of all gas penetrants increase with permeation temperature. Since the larger molecules require more activation energy for permeation, the temperature dependence of permeability is stronger for larger gas penetrants. As a result, as temperature increases, the permeability increase for larger penetrants is more than that for smaller penetrants, leading to the decrease of selectivities at higher permeation temperature.

Table 4.4 Temperature effect on permeation of 675 ℃ pyrolyzed Matrimid® CMS dense film for several gas penetrants. Tests were conducted at 25, 35 and 50 ℃ with 65 psia feed pressure.

Gas	Temperature (℃)	Permeability (Barrer)	Gas Pair	Temperature (℃)	Selectivity
N_2	25	11	N_2/CH_4	25	3.7
	35	14		35	3.6
	50	21		50	3.2
CH_4	25	3.0	O_2/N_2	25	8.0
	35	4.2		35	7.2
	50	6.7		50	5.7
O_2	25	88	CO_2/CH_4	25	91
	35	110		35	75
	50	122		50	62
CO_2	25	276	CO_2/N_2	25	25
	35	318		35	21
	50	411		50	19

Table 4.5 Temperature effect on permeation of 800 ℃ pyrolyzed Matrimid® CMS dense film for several gas penetrants. Tests were conducted at 25, 35 and 50 ℃ with 65 psia feed pressure.

Gas	Temperature (℃)	Permeability (Barrer)	Gas Pair	Temperature (℃)	Selectivity
N_2	25	5.6	N_2/CH_4	25	8.3
	35	6.8		35	7.7
	50	9.0		50	7.6
CH_4	25	0.68	O_2/N_2	25	10.5
	35	0.88		35	9.8
	50	1.2		50	9.3
O_2	25	59	CO_2/CH_4	25	290
	35	66		35	250
	50	83		50	212
CO_2	25	197	CO_2/N_2	25	35
	35	220		35	33
	50	252		50	28

4.3.4.2 Temperature Effect on Sorption

The temperature dependence of sorption coefficients of 800 ℃ CMS dense film was investigated between 25 and 50 ℃, and N_2 and CH_4 sorption isotherms in this temperature range are shown in Figure 4.14. The values of Langmuir isotherm parameters are listed in Table 4.6. As expected, CH_4 shows higher hole-filling capacity C_H' and higher affinity constant b than N_2 due to its higher condensability compared to N_2, reflected by the relative critical temperatures (N_2 126 K vs. CH_4 191 K). The Langmuir affinity constant b of both N_2 and CH_4 shows little temperature dependence, but the

Langmuir hole-filling capacity C_H' decreases with increasing temperature for both N_2 and CH_4. The rigid structure of CMS membrane makes it unlikely that the micropore volume will substantially change over the temperature range investigated. Nevertheless, since densities of sorbed penetrants at saturation in microporous cavities decrease with increasing temperature [17], most of the change in C_H' presumably reflects the change of sorbed density at saturation in the CMS membrane.

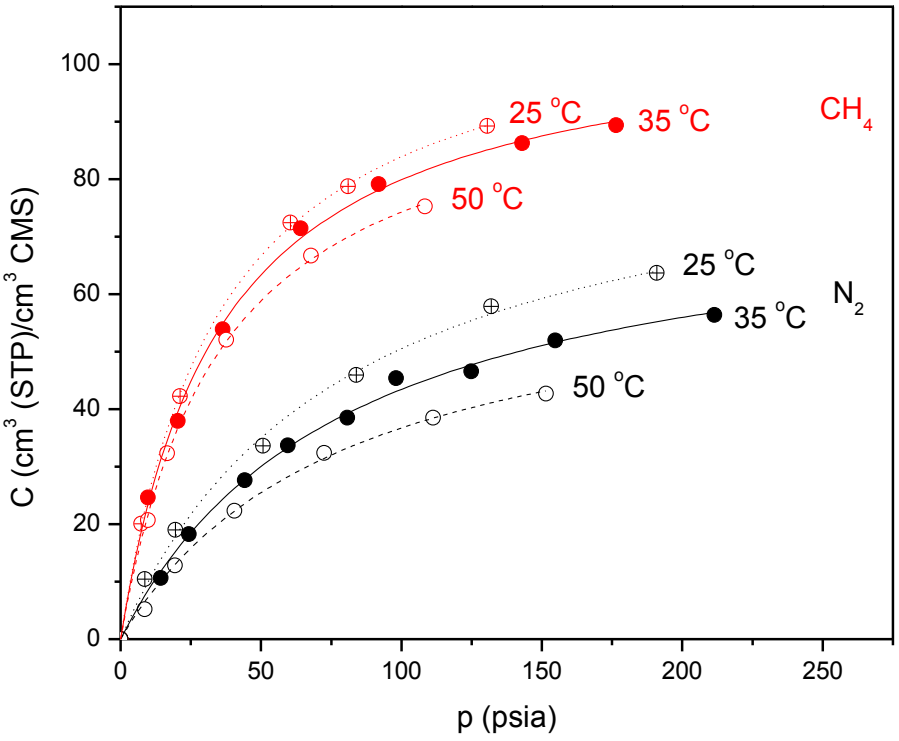

Figure 4.14: N_2 and CH_4 Langmuir isotherms of 800 ℃ Matrimid® CMS dense film at 25, 35 and 50 ℃.

Table 4.6 Langmuir isotherm parameters of 800 ℃ Matrimid® CMS dense film at 25, 35 and 50 ℃.

Gas	Temperature (℃)	C_H' (cm^3 (STP)/cm^3 CMS)	b (1/psia)
N_2	25 ℃	102.1 ± 4.4	0.014 ± 0.002
	35 ℃	77.9 ± 2.5	0.013 ± 0.003
	50 ℃	59.5 ± 1.1	0.014 ± 0.001
CH_4	25 ℃	115.2 ± 5.5	0.027 ± 0.004
	35 ℃	108.1 ± 3.4	0.028 ± 0.003
	50 ℃	98.5 ± 0.9	0.030 ± 0.001

The temperature dependence of sorption coefficient S follows the van't Hoff relationship described in Chapter 2. The sorption properties of 800 ℃ CMS dense film evaluated at 25, 35, and 50 ℃ and 65 psia are listed in Table 4.7. The apparent heat of sorption H_S and sorption pre-exponential factor S_0 for N_2 and CH_4 are obtained from least squares fitting plot (Figure 4.15) and are listed in Table 4.7. Results show that the sorption coefficients of N_2 and CH_4, and N_2/CH_4 sorption selectivity all decrease with increasing temperature. It should be noticed that N_2 shows lower (more negative) apparent heat of adsorption than CH_4. In the exothermic sorption process, a more negative heat of adsorption indicates lower adsorbed energy. This is contrary to the general trend that more condensable penetrants with higher critical temperature exhibit more negative heats of sorption that Costello and Koros previously proved in some polyimides and polycarbonates [18, 19]. However, in some other polymers, zeolite and

active carbon, more negative heats of sorption of N_2 than CH_4 have also been observed [16, 20, 21]. The lower adsorbed energy of N_2 in CMS might be explained by the interaction between the quadrupole moments of N_2 molecule and graphite basal plane [22]. In any case, the heat of adsorption for both N_2 and CH_4 are rather low.

Table 4.7: Sorption properties of 800 ℃ Matrimid® CMS membrane at 65 psia.

		N_2	CH_4
$\mathcal{S}$ (cm3 (STP)/cm3 CMS/psi)	25 ℃	0.603	1.131
	35 ℃	0.543	1.080
	50 ℃	0.476	1.004
H_S (kJ/mol)	-	-7.6 ±0.2	-3.8 ±0.2
$\mathcal{S}_0$ (cm3 (STP)/cm3 CMS/psi)	-	0.028 ±0.002	0.242 ±0.015
$\mathcal{S}_{N2}$ / $\mathcal{S}_{CH4}$	25 ℃	0.53	
	35 ℃	0.50	
	50 ℃	0.47	

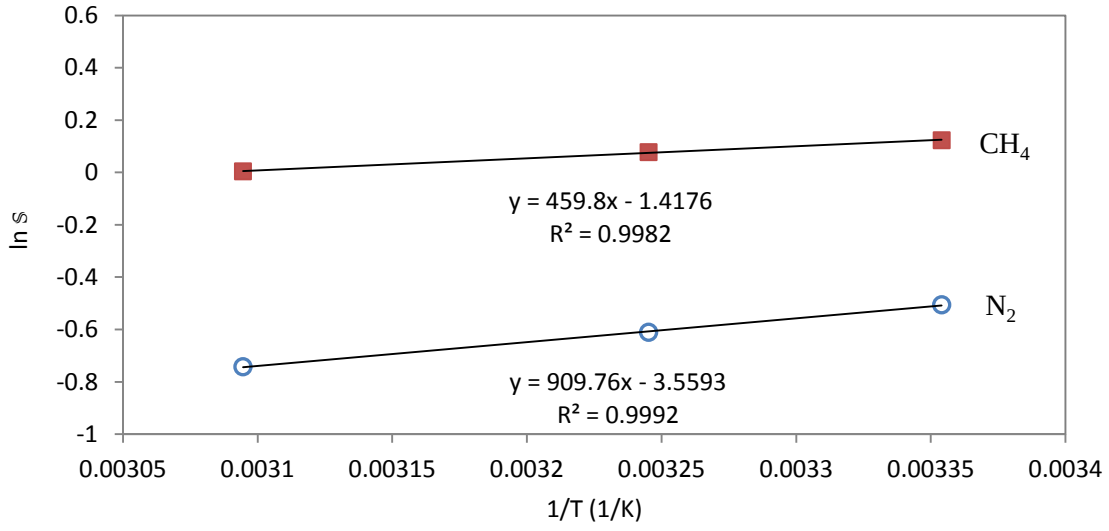

Figure 4.15: Temperature dependence of sorption coefficients of 800 ℃ Matrimid® CMS membrane at 65 psia (sorption coefficient $\mathcal{S}$ is in the unit of cm^3 (STP)/cm^3 CMS/psi).

4.3.4.3 Temperature Effect on Diffusion

From the permeabilities and sorption coefficients measured at 25, 35, and 50 ℃, diffusion coefficients can be calculated and they are listed with diffusion selectivities in Table 4.8. The temperature dependence of diffusion coefficients follows the Arrhenius relationship described in Chapter 2. The activation energy of diffusion E_D and diffusion pre-exponential factor D_0 for N_2 and CH_4 were obtained from the least squares fitting plot (Figure 4.16) and are listed in Table 4.8. As expected, the diffusion coefficients of both N_2 and CH_4 increase with temperature; however, since the temperature dependences of these two diffusion coefficients are at a similar level, the diffusion selectivity trend is not significant beyond experimental error. This tendency is an indication of dominance of entropic factors in the activation process, as will be discussed in Section 4.3.5, and shown in Table 4.8.

Table 4.8: Diffusion properties of 800 ℃ Matrimid® CMS membrane at 65 psia.

		N_2	CH_4
D (10^{-8} cm^2/s)	25 ℃	0.482	0.031
	35 ℃	0.646	0.042
	50 ℃	0.975	0.061
E_D (kJ/mol)	-	22.6 ± 0.1	21.6 ± 0.8
D_0 (10^{-8} cm^2/s)	-	$(4.37 \pm 0.20) \times 10^3$	$(1.89 \pm 0.61) \times 10^2$
$D_{N2}/ DCH4_0$	25 ℃	15.5	
	35 ℃	15.3	
	50 ℃	16.0	
Entropic factor in Eq. (4.2)	-	23.6	
Energetic factor in Eq. (4.2)	35 ℃	~0.7	

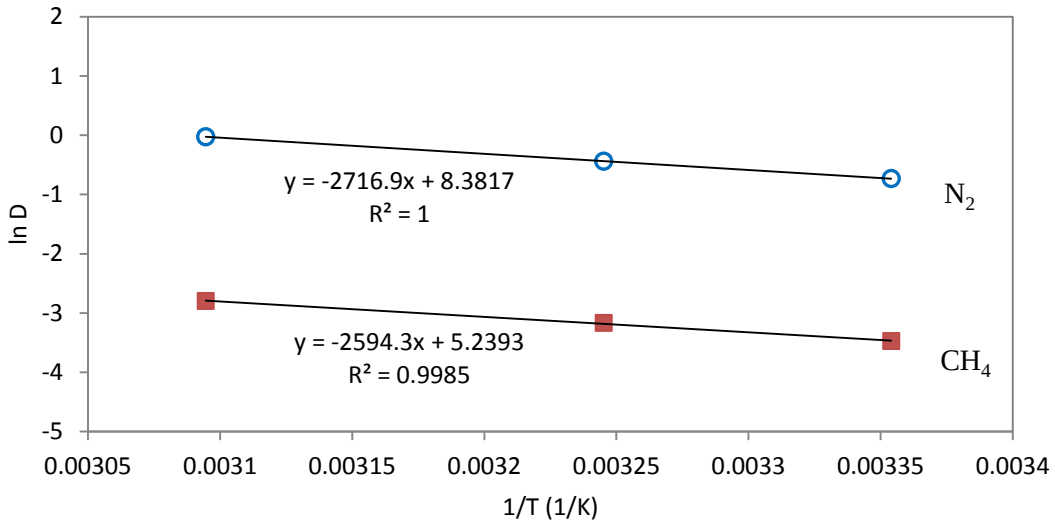

Figure 4.16: Temperature dependence of diffusion coefficients of 800 ℃ Matrimid® CMS membrane at 65 psia (diffusion coefficient D is in the unit of 10^{-8} cm^2/s).

4.3.5 Deconvolution of Energetic and Entropic Factors in Diffusion Selection Effect

Diffusion selectivity can be further decomposed into a product of entropic selectivity and energetic selectivity as described in Chapter 2. The pre-exponential factor D_0 in the Arrhenius relationship can be represented from transition state theory as

$$D_0 = e\lambda^2 \frac{kT}{h} exp\left[\frac{S_D}{R}\right] \tag{4.1}$$

where λ is the average diffusive jump length, S_D is the activation entropy of diffusion, k is Boltzmann's constant, and h is Planck's constants [23]. Note that the S used for entropy here is different from the $\mathcal{S}$ used to designate the sorption coefficient. For gas pairs with similar kinetic diameters able to access all of the micropores, λ can be

considered equal for both gases [24]. In such a case, the diffusion selectivity can be expressed as a product of entropic diffusion selectivity and energetic diffusion selectivity, as shown in Equation (4.2).

$$\frac{D_A}{D_B} = \frac{D_{0A}}{D_{0B}} exp\left(-\frac{E_{DA} - E_{DB}}{RT}\right)$$

$$= \underbrace{exp\left(\frac{S_{DA} - S_{DB}}{R}\right)}_{\text{Entropic selectivity}} \cdot \underbrace{exp\left(-\frac{E_{DA} - E_{DB}}{RT}\right)}_{\text{Energetic selectivity}}$$

$$= exp\left(\frac{\Delta S_{DA,B}}{R}\right) \cdot exp\left(-\frac{\Delta E_{DA,B}}{RT}\right) \qquad (4.2)$$

where $\Delta S_{DA,B}$ is the difference in the diffusion activation entropy for penetrants A and B, and $\Delta E_{DA,B}$ is the difference in the activation energy of diffusion for penetrants A and B. The entropic factor and energetic factor in the N_2/CH_4 diffusion selectivity of the 800 ℃ Matrimid® CMS membrane are listed in Table 4.8. These results show that energetic factor makes negative contribution to the diffusion selectivity due to the higher apparent diffusion activation energy for N_2; however, the entropic factor provides a significant contribution to the high diffusion selectivity.

4.3.5.1 Energetic Factor in Diffusion Selectivity

The higher diffusion activation energy for N_2 vs. CH_4 and the N_2/CH_4 energetic diffusion selectivity of 0.7 shown in Table 4.10 are interesting, given the relative size of N_2 and CH_4. According to the Kihara potential, the length and width of spherocylindrical N_2 are considered to be 3.09 and 4.07 Å, respectively [24], while CH_4 can be considered

essentially a spherical molecule with kinetic diameter of 3.8 Å (Fig. 4.17). The diffusion jump between a normal state and an activated state in the molecular sieving ultramicropore window effectively determines the diffusion selectivity. The normal state can be either a free molecule within the micropores, or an adsorbed state on the graphitic basal plane in the micropores. From either of the states, the penetrant must acquire adequate energy to overcome the repulsion opposing movement into the ultramicropore. The slimmer shape of N_2 would seem to experience less repulsion than that of CH_4; however, if the penetrant starts its diffusion jump from a lower energy adsorbed state, more energy is required to desorb from the sorption site before it can jump into the ultramicropore. Thus the diffusion activation energy E_D, will be the sum of the desorption energy E_{desorp}, and the energy to overcome ultramicropore repulsion, $E_{repulsion}$, as shown below.

$$E_D = E_{desorb} + E_{repulsion} \tag{4.3}$$

Indeed, the apparent heat of sorption shows a roughly 3.8 kJ/mol stronger interaction between N_2 and the sorption site, and the N_2 activation energy to jump from an adsorbed state to ultramicropore is 1 kJ/mol higher than that of CH_4. This difference is only slightly beyond the experimental uncertainty and may not be significant; however, studies over larger temperature ranges might be useful to explore this issue in more detail. In any case, it appears possible that a lower repulsion of the compact N_2, coupled with a lower sorbed energy for N_2 vs. CH_4 combine to yield the similar diffusion activation energies observed for the quite different sized penetrants. If the ultramicropores were smaller, due to more extensive thermal exposure during pyrolysis, CH_4 may be able to

barely get through, while the slimmer N_2 could pass. In such a hypothetical case, the repulsion opposing the diffusion jump of CH_4 is expected to increase much more significantly than that of N_2, and the lower repulsion for N_2 might compensate its higher energy of desorption. In such a case, one might expect to observe an overall lower diffusion activation energy for N_2 relative to CH_4; however, both activation energies would be higher than observed here. This means if subtly tighter ultramicropores can be achieved, the energetic factor in diffusion selectivity could assist N_2, in addition to an entropic factor, discussed below.

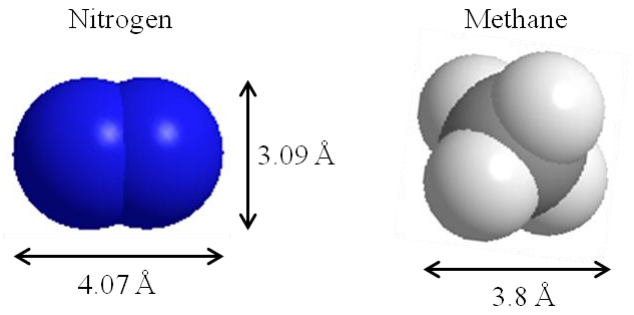

Figure 4.17: Sizes and shapes of N_2 and CH_4 molecule.

4.3.5.2 Entropic Factor in Diffusion Selectivity

High entropic diffusion selectivity has been previously observed in molecular sieving materials including zeolite 4A and CMS for O_2/N_2 and C_2H_4/C_2H_6 [1, 24]; however, an entropic contribution to N_2/CH_4 diffusion selectivity in molecular sieving

materials has not been reported previously. The highest N_2/CH_4 entropic diffusion selectivity that has been observed in polymer is 3.5, which was obtained from 6FDA/PMDA(50/50)-TAB membrane [25].

The high entropic factor in N_2/CH_4 diffusion coefficient can be interpreted using the Transition State Theory. According to this theory, the diffusion coefficient for a penetrant through any medium can be described by the following equation

$$D = \lambda^2 \frac{kT}{h} \frac{F^{\neq}}{F} exp\left(\frac{-E_D}{RT}\right) \tag{4.4}$$

where $F^{\neq}$ represents the partition function for the gas penetrant in the transition state as it passes through the constricted ultramicropore window, and F is the partition function for the same molecule in the normal state when it resides in the micropore cavities [23, 24]. Considering the same jump length λ for N_2 and CH_4, the N_2/CH_4 entropic diffusion selectivity can be written as

$$\left(\frac{D_{N_2}}{D_{CH_4}}\right)_{entropic} = exp\left(\frac{S_{D,N_2} - S_{D,CH_4}}{R}\right) = \frac{(F^{\neq}/F)_{N_2}}{(F^{\neq}/F)_{CH_4}} \tag{4.5}$$

The partition function consists of translational, rotational, and vibrational contributions, as shown below.

$$F = F_{trans} \cdot F_{rot} \cdot F_{vib} \tag{4.6}$$

These partition functions can be calculated in an idealized cubic cavity of dimension *a* using the following equations.

Translational: $$F_{trans} = \left(\frac{2\pi \ m \ k \ T}{h^2} \right)^{n/2} a^n \tag{4.7}$$

Rotational:

Diatomic: $$F_{rot} = \left(\frac{T}{\sigma \ \Theta_r} \right)^{n/2} \tag{4.8}$$

Polyatomic: $$F_{rot} = \frac{\pi^{n/6}}{\sigma^{n/3}} \left(\frac{T^3}{\Theta_{rA} \ \Theta_{rB} \ \Theta_{rC}} \right)^{n/6} \tag{4.9}$$

Vibrational:

Diatomic: $$F_{vib} = \left[\frac{exp\left(-\frac{\Theta_v}{2T} \right)}{1 - exp\left(-\frac{\Theta_v}{T} \right)} \right] \tag{4.10}$$

Polyatomic: $$F_{vib} = \prod_{i=1}^{n} \left[\frac{exp\left(-\frac{\Theta_{v,i}}{2T} \right)}{1 - exp\left(-\frac{\Theta_{v,i}}{T} \right)} \right] \tag{4.11}$$

where n is the number of degrees of freedom for each type of motion of the molecule, m is the mass of the molecule, k is Boltzmann constant, h is Planck constant. Besides, a is the length of the cubic cavity in which the penetrant is confined, Θ_r, Θ_{rA}, Θ_{rB}, and Θ_{rC} are the characteristic rotational temperatures, σ is the symmetry number of the molecule, and Θ_v is the characteristic vibrational temperature. The characteristic rotational and

vibrational temperatures Θ_r and Θ_v are used to simplify the partition function, and are defined as below.

$$\Theta_r = \frac{h^2}{8\pi^2 Ik} \tag{4.12}$$

$$\Theta_v = \frac{h\nu}{k} \tag{4.13}$$

where I is the moment of inertia, and ν is the frequency of vibration [26]. Parameters used in this calculation are listed in Table 4.9.

Table 4.9 Parameters used in entropic diffusion selectivity calculation [26].

	N_2	CH_4
Θ_r (K)	2.88	7.54, 7.54, 7.54
Θ_v (K)	3374	4170, 2180(2), 4320(3), 1870(3)
σ	2	12

The numbers in parentheses represent the degeneracy of each vibrational temperature.

At this point, some speculative approximations must be made to proceed further. As noted above, gas penetrants initiate a diffusion jump from an adsorbed state, and we will idealize this state to be essentially adsorbed on the graphitic basal plane in the micropore, which is a reasonable limiting case. The activated transition state corresponds to that with the gas penetrant moving through the 'slit'-shaped ultramicropore of CMS with a characteristic average pore size shown as 3.8 Å. The normal state and activated

state are illustrated in Figure 4.18 for this case, and in the adsorbed normal state, both N_2 and CH_4 have an in-plane minimum energy adsorption orientation on the graphitic structure basal plane as shown in Figure 4.18 (a) and (b) [27-30]. However, at the temperatures investigated in this study, both penetrants in the adsorbed phase are orientationally disordered and can both translate and rotate [27, 31]. In the activated state, the partition function $F^{\neq}$ does not contain the translational partition function in the direction of gas diffusion (horizontal direction in Figure 4.18(c)) for either penetrant, since the factor $\frac{kT}{h}$ in Eq. (4.4) accounts for this degree of freedom [24]. The 'slimmer' N_2 has two translational degrees of freedom in the vertical direction and along the lateral dimension of the 'slit-shaped' pore (in the direction perpendicular to paper). For the vertical direction, the cavity height a is considered to be 0.7 Å, which is the difference between N_2 molecule height 3.09 Å and the pore size 3.8 Å. In contrast, CH_4 can only have one translational degree of freedom along the lateral dimension of the slit-shaped pore at certain configurations with minimal projected height in the vertical direction, like the one shown on the right in Figure 4.18(c), but no translational degree of freedom in the vertical direction due to its larger width vs. N_2. Moreover, subtle changes in the configuration may cause it to lose its single translational degree of freedom. For example, if the projected height in the vertical direction in Figure 4.18 (c) is the same as the 'slit-shaped' pore size in some configurations, CH_4 would be stuck in it and could not freely translate or rotate. Thus the translational degree of freedom for CH_4 is believed to be either 1 or 0, depending on its configuration in the activated state. The rotational degrees of freedom of both penetrants are shown in Figure 4.18 (c). Clearly, N_2 can rotate freely around the vertical axis, since its width is much smaller than the size of the pore.

Moreover, N_2 can also tilt ~45◦ around the axis perpendicular to paper in the activated state as shown in the middle in Figure 4.18 (c), which is approximately considered to be another ¼ rotational degree of freedom (considering it can rotate 90◦ out of 360◦). On the other hand, due to its relative large size in such a highly confined ultramicropore, CH_4 can only have one rotational degree of freedom around the vertical axis at certain configurations, like the one shown on the right in Figure 4.18 (c). A subtle change in the configuration would also make it impossible to rotate around this axis, as noted above. Thus the rotational degree of freedom for CH_4 is believed to be either 1 or 0, depending on its configuration in the activated state. The vibration of both penetrants is believed to be unrestricted in both normal and activated state. With the above discussion, the maximum N_2/CH_4 entropic diffusion selectivity at 35 ℃ is calculated to be 51.9 if the translational and rotational degrees of freedom for CH_4 in the activated state are both 0, while it is 5.5 when these two degrees of freedom for CH_4 are both 1. The details of calculations to get these results are presented in Appendix B. With CH_4 having different configurations in the activated state, the averaged entropic diffusion selectivity in the illustrated ultramicropore of size 3.8 Å will be between 5.5 and 51.9. Clearly, in a situation where there is some distribution in the ultramicropore size, the case is complex. The N_2/CH_4 entropic diffusion selectivity obtained from experiment, which is 23.6, lies in the range calculated above, suggesting that the average ultramicropore size in the 800 ℃ CMS membrane is very close to the size of CH_4. As a result, this membrane material can effectively distinguish the size and shape difference between N_2 and CH_4 and perform strong molecular sieving effect.

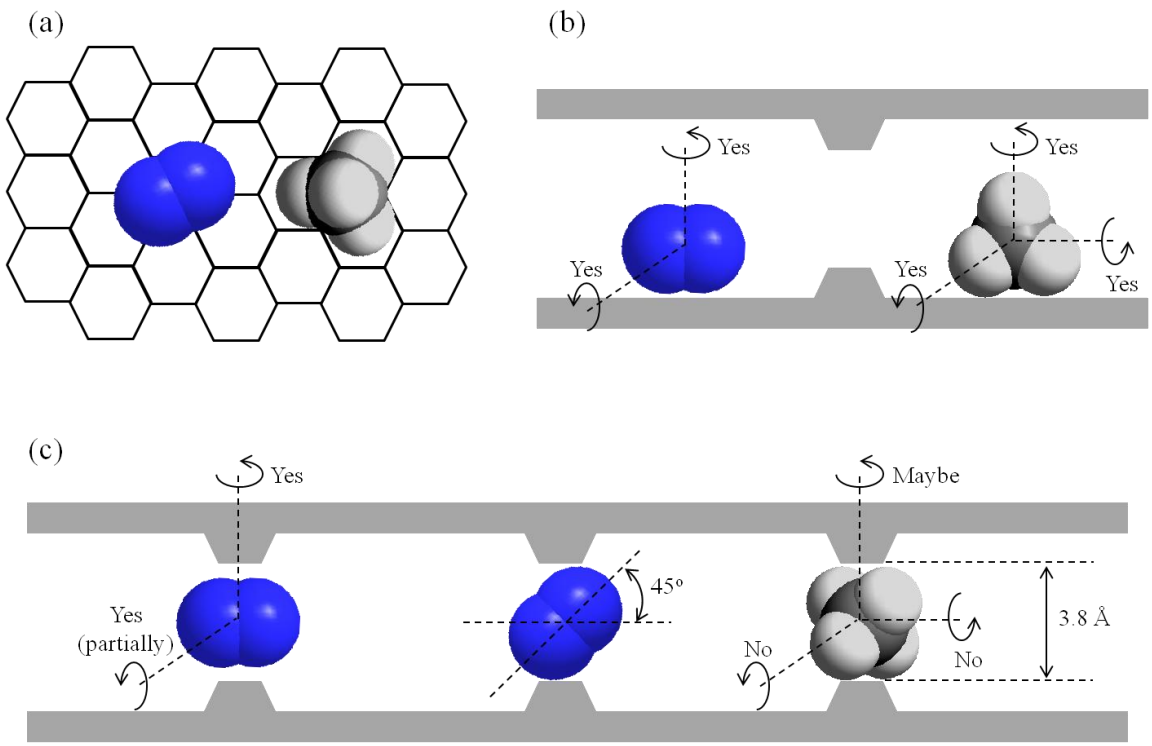

Figure 4.18: Configurations of N_2 and CH_4 in the normal and activated state, (a) top view of N_2 and CH_4 in adsorbed normal state, (b) side view of N_2 and CH_4 in adsorbed normal state, (c) side view of N_2 and CH_4 in activated transition state during a diffusion jump.

4.3.6 Wide Angle X-ray Diffraction (WAXD) of Matrimid® CMS Membranes

WAXD can be used to determine the crystalline structure of polymer and carbon materials. By analyzing the Bragg peaks scattered to wide angles, sub-nanometer-sized structures in tested samples can be implied. The atoms in crystalline samples are regularly spaced and positioned on imaginary planes. The distance between these planes is called the d-spacing, which can be determined by the Bragg angle between the incident ray and the scattering planes using the Bragg'a law:

$$n\lambda = 2d\sin\theta \tag{4.14}$$

where n is an integer, λ is the wavelength of incident wave (λ=1.53 Å for CuKα radiation), d is the d-spacing, and θ is the Bragg angle. The WAXD patterns of Matrimid® precursor and 550, 675, and 800 ℃ pyrolyzed Matrimid® CMS are shown in Figure 4.19, with a comparison to the WAXD pattern of graphite.

As shown by the WAXD pattern, carbon atoms are highly ordered in crystalline graphite. The well defined peak at 3.35 Å is the distance between graphite layers and represents the (002) plane reflection. The peak at 5.7 Å in Matrimid® precursor is a typical d-spacing in amorphous glassy polymers. This peak disappears as Matrimid® is pyrolyzed to CMS membranes. Two broad peaks at 3.8 Å and 2.1 Å appear in the CMS membranes and intensify as pyrolysis temperature increases from 550 to 800 ℃. This indicates that the CMS membranes are amorphous and disordered in the long range, but the ordering in carbon structure increases at higher pyrolysis temperature. Such increase in structure ordering explains the enhanced selectivities observed in CMS membranes pyrolyzed at higher temperature. The 2.1 Å peak in CMS membranes have the same d-spacing as the (100) plane in graphite, indicating the formation of short-range conjugated aromatic graphitic structure.

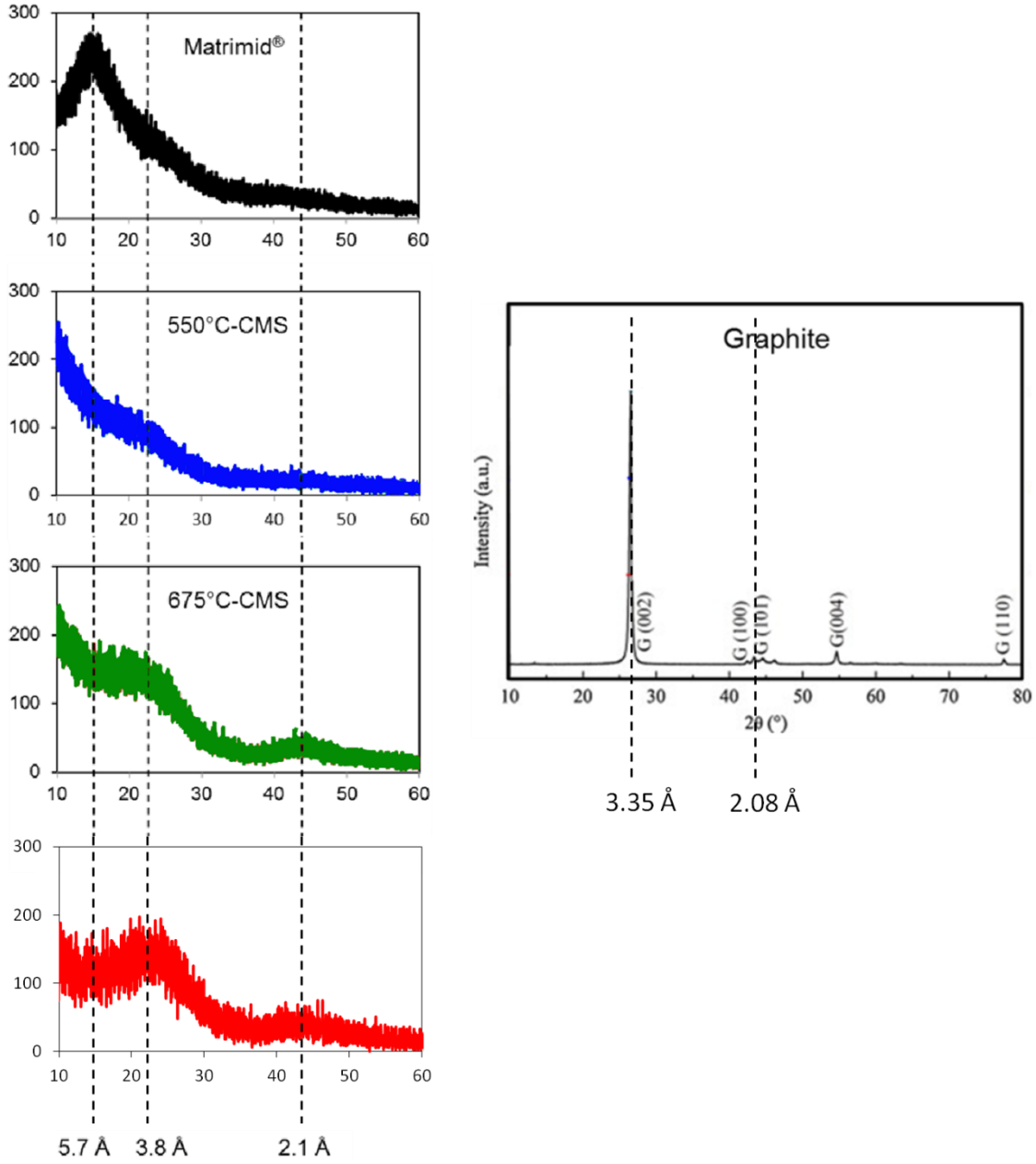

Figure 4.19: WAXD patterns for Matrimid® precursor and Matrimid® CMS membrane pyrolyzed at 550, 675 and 800 ℃, and graphite [32].

4.3.7 Pure Gas vs. Mixed Gas Performance

The 550, 675 and 800 ℃ pyrolyzed Matrimid® CMS membranes pyrolyzed under UHP Ar with 2 hour soak time were tested with the 20% N_2/80% CH_4 mixed gas feed. The total gas feed pressure was 100 psia and the stage cut was maintained at <1%. The steady state mixed gas permeation results are summarized in Figure 4.20, with comparison to the pure gas permeation results. The measured mixed gas permeation properties were obtained from feed stream and permeate stream compositions obtained from GC and the partial feed pressure of each gas. The mixed gas permeation properties of 800 ℃ pyrolyzed Matrimid® CMS can be predicted by the following equations, assuming there is only sorption competition between N_2 and CH_4. The pure gas, predicted mixed gas, and measured mixed gas permeation performance of 800 ℃ pyrolyzed Matrimid® CMS dense film is summarized in Table 4.10.

$$P_A = \frac{D_A C'_{HA} b_A}{1 + b_A p_A + b_B p_B} \tag{4.15}$$

$$P_B = \frac{D_B C'_{HB} b_B}{1 + b_A p_A + b_B p_B} \tag{4.16}$$

$$\alpha_{A/B} = \frac{P_A}{P_B} = \frac{D_A C'_{HA} b_A}{D_B C'_{HB} b_B} \tag{4.17}$$

Table 4.10: Comparison of pure and mixed gas permeation results of 800 °C Matrimid® CMS dense film. Tested at 35 °C with 100 psia feed pressure.

	P_{N_2} (Barrer)	P_{CH_4} (Barrer)	P_{N_2} / P_{CH_4}
Pure gas	6.78	0.88	7.69
Predicted mixed gas	3.57	0.71	5.12
Measured mixed gas	5.17	0.87	5.94

Similar to the results observed in 6FDA:BPDA-DAM derived CMS membranes, both N_2 permeabilities and N_2/CH_4 selectivities decreased from pure gas feed to mixed gas feed. The competition between the two gas penetrants slows down the permeation of both, leading to lower permeabilities. Also, CH_4 takes advantage of its stronger sorption affinity in the competition. With its higher Langmuir affinity constant, CH_4 can occupy sorption sites available to N_2 under pure gas condition; thereby resulting in a lower N_2/CH_4 mixed gas selectivity. This fact notwithstanding, the mixed gas separation performance is reasonably estimated by the pure gas permeation tests. For less challenging, but still realistic feeds with higher N_2 composition (e.g. 40% N_2), the CH_4 competition would be less significant, and the N_2 permeability would be expected to be even closer to the pure gas value.

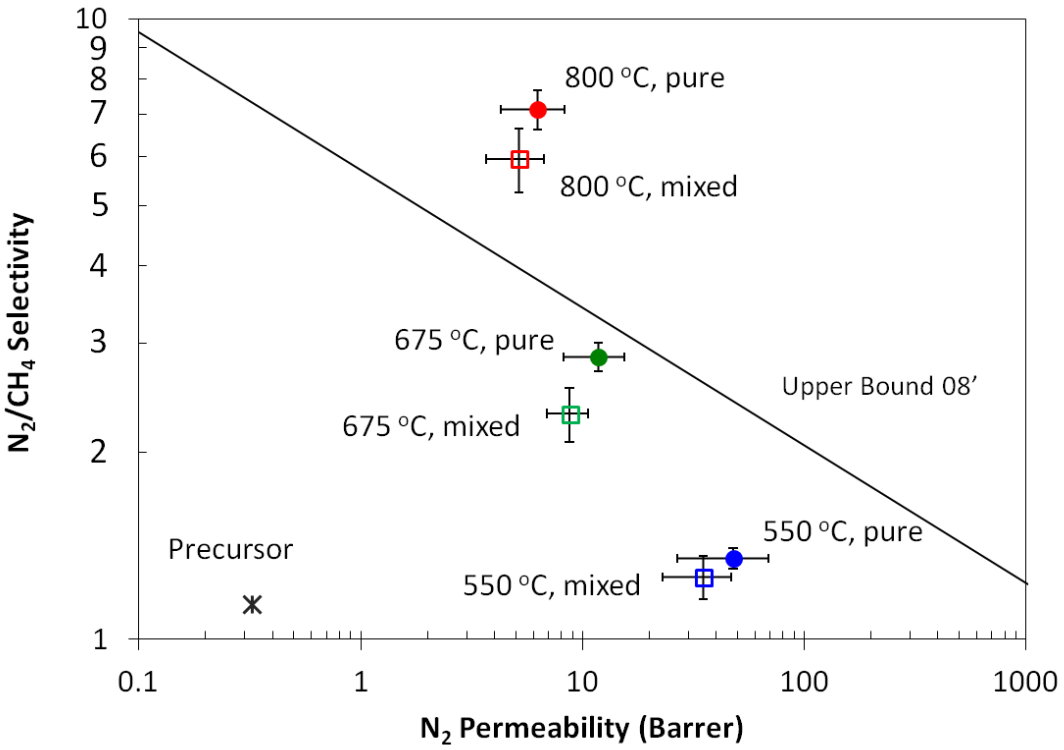

Figure 4.20: Mixed and pure gas permeation results of 550 °C and 800 °C pyrolyzed Matrimid® CMS membranes with 2 hour soak time.

4.4 Summary

The effects of pyrolysis conditions including pyrolysis temperature, soak time, oxygen/hydrogen doping were studied based on Matrimid® and 6FDA:BPDA-DAM CMS membranes. It was shown that increasing pyrolysis temperature is more effective to improve selecitivity than increasing soak time. Oxygen doping was proved to be able to fine tune the ultramicropore structure without a significant loss in permeability for 6FDA:BPDA-DAM CMS membrane. However, due to the intrinsic open structure, 6FDA:BPDA-DAM CMS membranes cannot provide satisfying separation performance

for N_2/CH_4. On the other hand, Matrimid® CMS membranes have shown superior N_2/CH_4 separation performance, especially at high pyrolysis temperature. Due to the small size difference between N_2 and CH_4, high pyrolysis temperature is essential to achieve tight ultramicropores with strong molecular sieving effect. Since oxygen doping can clog the tight ultramicropores, hydrogen doping was instead applied to Matrimid® CMS membranes. However, results showed that no significant change in separation properties was obtained mainly due to the poor chemisorption of hydrogen onto carbon. Temperature effects on permeability, sorption coefficient and diffusion coefficient for 800 ^{o}C Matrimid® CMS membrane were studied, and the entropic and energetic factors in diffusion selectivity were analyzed and discussed. It was found that diffusion selection effect, more specifically, the entropic contribution in diffusion selection solely contributes to the overall permselectivity observed in this high performing membrane sample. Transition state theory was applied to theoretically interpret how entropic factor plays an essential role in CMS membrane gas separation.

4.5 References

[1] Rungta M, Xu L, Koros WJ. Carbon molecular sieve dense film membranes derived from matrimid® for ethylene/ethane separation. Carbon 2012;50(4):1488-502.

[2] Steel KM, Koros WJ. Investigation of porosity of carbon materials and related effects on gas separation properties. Carbon 2003;41(2):253-66.

[3] Kiyono M, Williams PJ, Koros WJ. Effect of pyrolysis atmosphere on separation performance of carbon molecular sieve membranes. J Membr Sci 2010;359(1–2):2-10.

[4] Saufi SM, Ismail AF. Fabrication of carbon membranes for gas separation—a review. Carbon 2004;42(2):241-59.

[5] Rungta M. Carbon molecular sieve dense film membranes for ethylene/ethane separations. Atlanta: Georgia Institute of Technology; 2012.

[6] Steel KM. Carbon membranes for challenging gas separations. Austin: University of Texas at Austin; 2000.

[7] Kiyono M. Carbon molecular sieve membranes for natural gas separations. Atlanta: Georgia Institute of Technology; 2010.

[8] Grisdale R. The properties of carbon contacts. J Appl Phys 2004;24(10):1288-96.

[9] Robeson LM. The upper bound revisited. J Membr Sci 2008;320(1-2):390-400.

[10] Steel KM, Koros WJ. An investigation of the effects of pyrolysis parameters on gas separation properties of carbon materials. Carbon 2005;43(9):1843-56.

[11] Slater JC. Atomic radii in crystals. The Journal of Chemical Physics 1964;41(10):3199-204.

[12] Inagaki M, Ibuki T, Takeichi T. Carbonization behavior of polyimide films with various chemical structures. J Appl Polym Sci 1992;44(3):521-5.

[13] Bansal RC, Vastola FJ, Walker Jr PL. Studies on ultra-clean carbon surfaces—iii. Kinetics of chemisorption of hydrogen on graphon. Carbon 1971;9(2):185-92.

[14] Bansal RC, Vastola FJ, Walker Jr PL. Studies on ultraclean carbon surfaces: Ii. Kinetics of chemisorption of oxygen on graphon. J Colloid Interface Sci 1970;32(2):187-94.

[15] Moore TT, Koros WJ. Gas sorption in polymers, molecular sieves, and mixed matrix membranes. J Appl Polym Sci 2007;104(6):4053-9.

[16] Zimmerman CM, Koros WJ. Polypyrrolones for membrane gas separations. Ii. Activation energies and heats of sorption. Journal of Polymer Science Part B: Polymer Physics 1999;37(12):1251-65.

[17] Koros WJ, Paul DR. Co2 sorption in poly(ethylene terephthalate) above and below the glass transition. Journal of Polymer Science: Polymer Physics Edition 1978;16(11):1947-63.

[18] Costello LM, Koros WJ. Thermally stable polyimide isomers for membrane-based gas separations at elevated temperatures. Journal of Polymer Science Part B: Polymer Physics 1995;33(1):135-46.

[19] Costello LM, Koros WJ. Effect of structure on the temperature dependence of gas transport and sorption in a series of polycarbonates. Journal of Polymer Science Part B: Polymer Physics 1994;32(4):701-13.

[20] Cavenati S, Grande CA, Rodrigues AE. Adsorption equilibrium of methane, carbon dioxide, and nitrogen on zeolite 13x at high pressures. J Chem Eng Data 2004;49(4):1095-101.

[21] Al-Muhtaseb SA. Adsorption and desorption equilibria of nitrogen, methane, ethane, and ethylene on date-pit activated carbon. J Chem Eng Data 2009;55(1):313-9.

[22] Vernov A, Steele WA. The electrostatic field at a graphite surface and its effect on molecule-solid interactions. Langmuir 1992;8(1):155-9.

[23] Glasstone S, Laidler KJ, Eyring H. The theory of rate processes: The kinetics of chemical reactions, viscosity, diffusion and electrochemical phenomena. New York: McGraw-Hill Book Company, Incorporated; 1941.

[24] Singh A, Koros WJ. Significance of entropic selectivity for advanced gas separation membranes. Ind Eng Chem Res 1996;35(4):1231-4.

[25] Zimmerman CM, Koros WJ. Entropic selectivity analysis of a series of polypyrrolones for gas separation membranes. Macromolecules 1999;32(10):3341-6.

[26] Mcquarrie DA. Statistical thermodynamics. Sausalito CA: University Science Books; 1973.

[27] Diehl RD, Fain Jr SC. Structure and orientational ordering of nitrogen molecules physisorbed on graphite. Surf Sci 1983;125(1):116-52.

[28] Phillips JM, Hammerbacher MD. Methane adsorbed on graphite. I. Intermolecular potentials and lattice sums. Physical Review B 1984;29(10):5859-64.

[29] Phillips JM. Methane adsorbed on graphite. Ii. A model of the commensurate-incommensurate transitions. Physical Review B 1984;29(10):5865-71.

[30] Hammond WR, Mahanti SD. Polar pyramidal molecules on a graphite substrate. Surf Sci 1990;234(3):308-14.

[31] Knorr K. Monolayers of polar methane derivatives physisorbed on graphite. Phys Rep 1992;214(2):113-57.

[32] Lai J, Guo H, Wang Z, Li X, Zhang X, Wu F, et al. Preparation and characterization of flake graphite/silicon/carbon spherical composite as anode materials for lithium-ion batteries. J Alloys Compd 2012;530(0):30-5.

CHAPTER 5

ANALYSIS OF DIFFERENT POLYMERS AS PRECURSORS FOR N_2/CH_4 SEPARATION

5.1 Overview

Apart from the pyrolysis conditions discussed in the previous chapter, the intrinsic polymer precursor properties can also significantly affect the separation performance of resulting CMS membranes. CMS membranes for N_2/CH_4 separation have not been widely studied and only a few polymer precursors including cellulose, Matrimid®, 6FDA:BPDA-DAM, BPVE-PFCB, and SPPO have been reported [1-6]. CMS membranes derived from several polymer precursors are presented in this chapter. Discussion regarding the correlation between CMS separation performance and precursor structure and properties are given. Since high pyrolysis temperature was proved to be essential for N_2/CH_4 separation, all polymer precursors studied in this chapter were pyrolyzed at 800 ℃ for 2 hour soak time under UHP Ar.

5.2 Comparison Between 6FDA-based and Non-6FDA-based CMS Membranes

The previous chapter discussed the effects of pyrolysis conditions on Matrimid® and 6FDA:BPDA-DAM. It was shown that the transport properties of CMS membranes derived from these two precursors vary significantly. In this section, the CMS membranes derived from Matrimid® and 6FDA:BPDA-DAM pyrolyzed under the same condition, i.e.

800 ℃ and soaked for 2 hours under UHP Ar, are compared in terms of permeation, sorption and diffusion .

The N_2 and CH_4 permeabilities, sorption coefficients, diffusion coefficients and corresponding selectivities are summarized in Table 5.1, Table 5.2 and Table 5.3. As seen from Table 5.1, the 6FDA:BPDA-DAM CMS dense film showed higher permeability but much lower selectivity than the Matrimid® CMS dense film, because of the overall more open intrinsic carbon structure. Sorption and diffusion data are useful to deconvolute the effect of penetrant condensability from effect of penetrant size and shape. The Langmuir isotherm parameters of these two dense films at 35 ℃ are summarized in Table 5.4. It is shown that while the Langmuir affinity constants *b* are similar; the Langmuir hole-filling capacity C_H' of 6FDA:BPDA-DAM CMS is much higher than that of Matrimid® CMS. This indicates that the micropores that function as sorption cavities in 6FDA:BPDA-DAM CMS are relatively larger than those in Matrimid® CMS. The much higher diffusion coefficients in 6FDA:BPDA-DAM CMS indicates larger ultramicropores in 6FDA:BPDA-DAM CMS than those in Matrimid® CMS, which functions as molecular sieving sites. Comparing the difference of N_2 and CH_4 diffusion coefficients in these two CMS dense films, it is observed that the difference in CH_4 diffusion coefficient is much larger than that of N_2 – while the N_2 diffusion coefficient of Matrimid® CMS is 40% of that of 6FDA:BPDA-DAM CMS, the CH_4 diffusion coefficient of Matrimid® CMS is only 7% of that of 6FDA:BPDA-DAM CMS. It is hypothesized that as shown in Figure 5.1, the ultramicropores in Matrimid® CMS are distributed at the lower value side on the horizontal axis and the pores accessible to CH_4 are at the tail of the pore distribution curve. So most of the ultramicropores in Matrimid® CMS are too small for CH_4 to pass

through, resulting in a strong molecular sieving effect reflected by the high diffusion selectivity.

Table 5.1: Permeability and permselectivity (35 ℃, 65 psia) of 800 ℃ pyrolyzed Matrimid® and 6FDA:BPDA-DAM CMS dense films. Permeabilities are in the units of Barrer.

	N_2	CH_4	N_2/CH_4
Matrimid®	6.78	0.88	7.69
6FDA:BPDA-DAM	25.0	16.7	1.50

Table 5.2: Sorption coefficient and sorption selectivity (35 ℃, 65 psia) of 800 ℃ pyrolyzed Matrimid® and 6FDA:BPDA-DAM CMS dense films. Sorption coefficients are in the units of (cm^3 (STP)/cm^3 CMS/psi).

	N_2	CH_4	N_2/CH_4
Matrimid®	0.57	1.07	0.50
6FDA:BPDA-DAM	0.85	1.46	0.58

Table 5.3: Diffusion coefficient and diffusion selectivity (35 ℃, 65 psia) of 800 ℃ pyrolyzed Matrimid® and 6FDA:BPDA-DAM CMS dense films. Diffusion coefficients are in the units of (10^{-8} cm^2/s).

	N_2	CH_4	N_2/CH_4
Matrimid®	0.62	0.04	15.3
6FDA:BPDA-DAM	1.53	0.55	2.78

Table 5.4: Langmuir isotherm parameters of 800 ℃ pyrolyzed Matrimid® and 6FDA:BPDA-DAM CMS dense films (tested at 35 ℃).

	Matrimid®		6FDA:BPDA-DAM	
	N_2	CH_4	N_2	CH_4
CH' (cm3 (STP)/cm3 CMS)	77.9	108.1	108.4	138.8
b (1/psia)	0.013	0.028	0.016	0.033

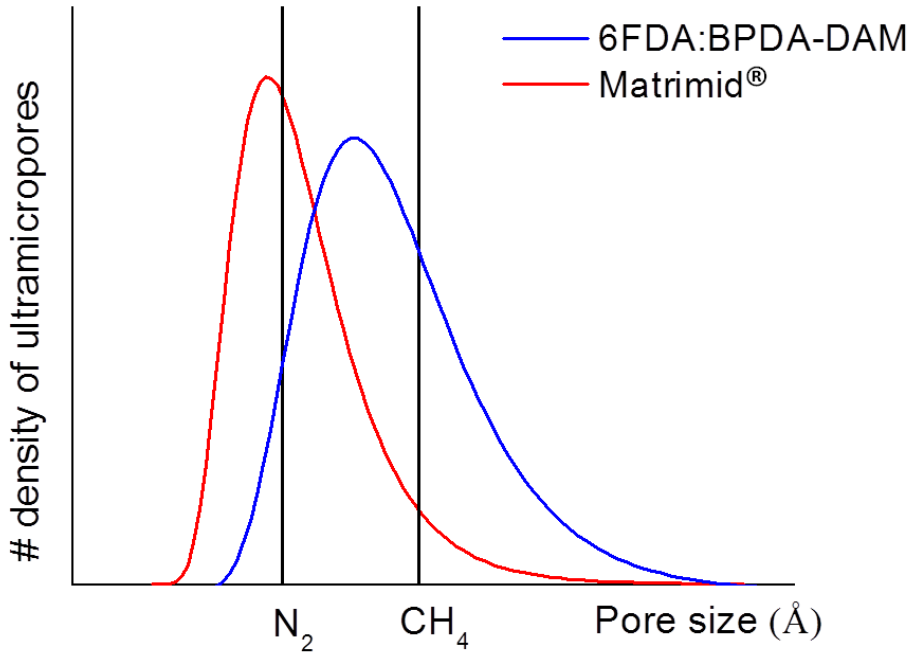

Figure 5.1: Hypothetical comparison of ultramicropore size distribution between 6FDA:BPDA-DAM and Matrimid® CMS membranes.

5.3 Separation Performance of CMS Membranes Derived from Other Precursors

As shown in the previous chapter, high pyrolysis temperature is essential for N_2/CH_4 CMS membrane separation to achieve the tight ultramicropore structure and relatively high N_2/CH_4 selectivity required. More polymer precursors were pyrolyzed at 800 ℃ for 2 hour soak time under UHP Ar, and their permeation results are shown in this section. P84® is the commercial name of BTDA-TDI/MDI developed by Evonik, which is a copolyimide and has shown attractive separation properties for CO_2/CH_4 after pyrolysis [7]. With a structure similar to Matrimid®, P84® can be easily dissolved in common solvents and processed into either dense film or hollow fiber morphologies [8, 9]. Kapton® is a biaxially oriented commercial film made from polyimide PMDA-ODA. Previous study showed that Kapton® CMS membranes can provide relatively high selecitivity but low permeability for CO_2/N_2 and O_2/N_2 gas pairs [10]. Torlon® is the commercial name of a high strength polyamide-imide (PAI) developed by Solvay. Previous study showed that CMS membranes derived from Torlon® provide relatively low permeabilities without exceptionally high selectivities for several gas pairs [6]. 6FDA-DAM was custom synthesized by Akron Polymer Systems, Inc. With a structure similar to 6FDA:BPDA-DAM, 6FDA-DAM usually provide high permeabilities but relatively low selectivities [11, 12]. 6FDA-mPDA has a similar structure compared to 6FDA-DAM. It was synthesized in-house by Wulin Qiu in the Koros group as part of a DOE Basic Energy Science study. The structures of these polymers together with Matrimid® and 6FDA:BPDA-DAM are shown in Figure 5.2.

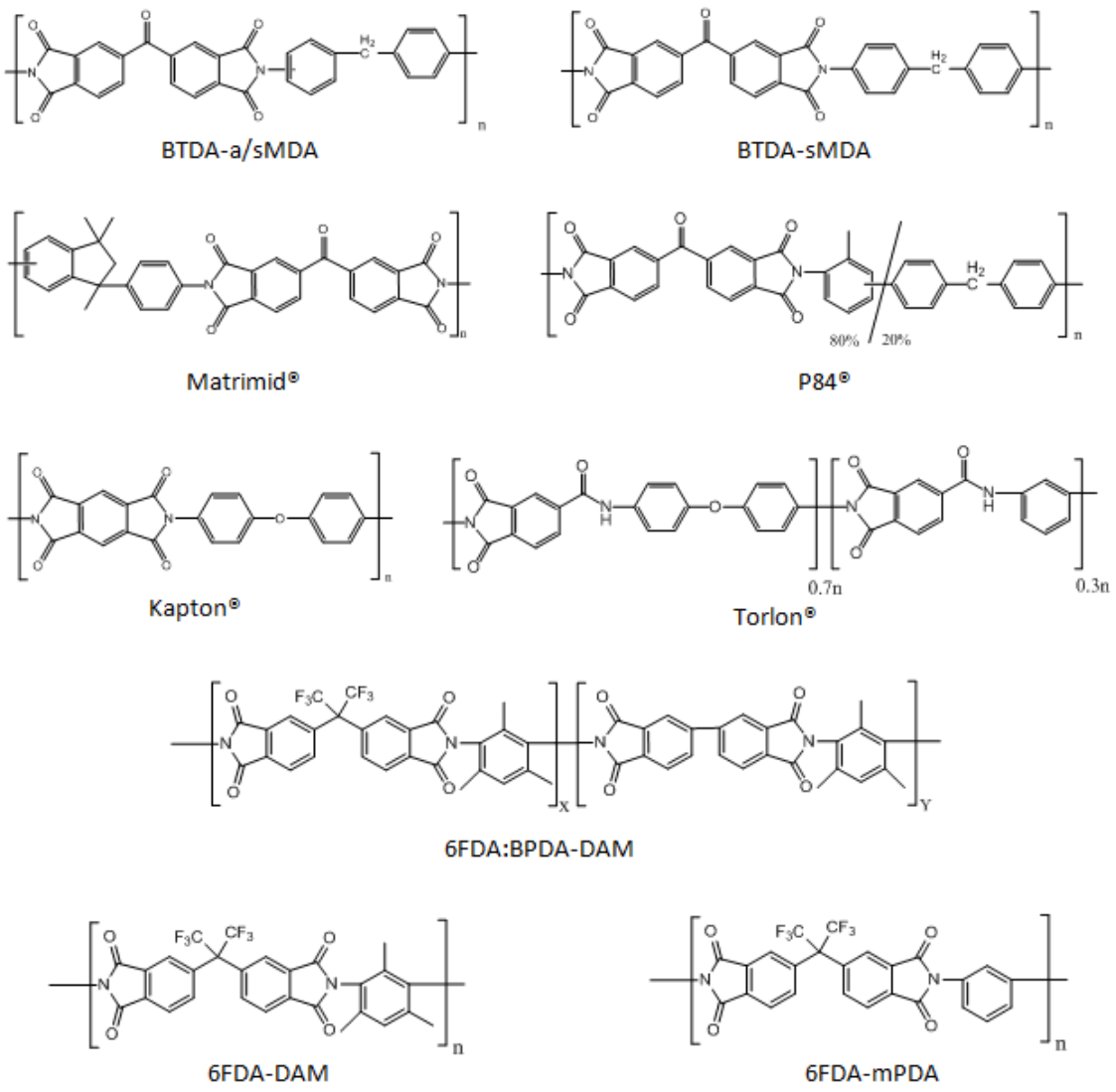

Figure 5.2: Chemical structures of studied polymer precursors.

All the polymer precursors were first dried at 110 ℃ in a convection oven for at least 12 hours before casting into dense films. Apart from Kapton®, which is already in the film morphology, all other polymer dense films were prepared by a solution casting method. Due to the poor solubility in dichloromethane (DCM), P84® and Torlon® were dissolved in Dimethylacetamide (DMAC) to prepare the polymer dope before casting. All

other polymer dopes were prepared with DCM as the solvent. Since DMAC has a higher boiling point than DCM (165.1 vs. 39.6 ℃), higher temperature during casting process is required for P84® and Torlon®. This was achieved by placing the casting set-up similar to that described in Chapter 3 on top of the convection oven. The Teflon® casting dish was replaced by a glass plate and a metal ring, which restrains the flow of polymer dope. No glove bag or solvent evaporating containers were used in this set-up. The metal ring sitting on top of the glass plate was covered by an inverted funnel with tissue paper plugging the neck. The temperature at the surface of glass plate was ~50 ℃. The casting process for other polymers was the same as described in Chapter 3. All the polymer dense films were dried in a 120 ℃ vacuum oven for 12 hours before pyrolysis. 800 ℃ temperature protocol, 2 hour soak time, and UHP Ar purge were applied to the pyrolysis of these polymer dense films. The permeation results of the CMS dense films derived from these polymer precursors are summarized in Figure 5.3.

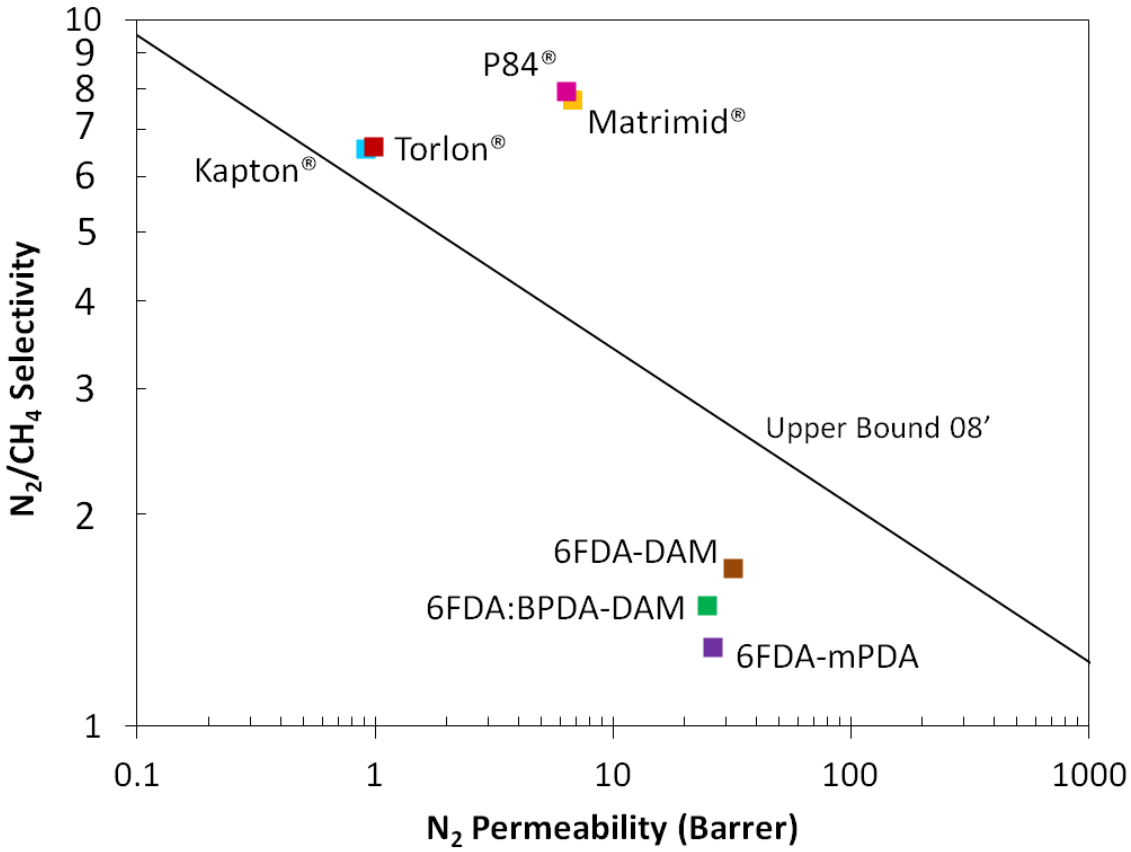

Figure 5.3: Plot of permeation results of 800 ℃ CMS dense films derived from several polymer precursors. The data points of Matrimid®/P84® and Kapton®/Torlon® are partially overlapping to each other.

The permeation results show that the CMS membranes derived from Matrimid®, P84®, Kapton® and Torlon® all surpass the upper bound line of polymer membranes and show potential for N_2 removal from CH_4. Whereas the 6FDA-related structures are preferred as precursors for most separations (e.g. O_2/N_2, CO_2/CH_4, C_2H_4/C_2H_6 and C_3H_6/C_3H_8) [2, 13-15], our discovery is that the 6FDA moiety is not attractive for the N_2/CH_4 separation. More detailed discussion regarding the precursor structure will be provided in later sections in this chapter.

5.4 Synthesis of BTDA-s/aMDA and BTDA-sMDA Polymer Precursors

As shown in the previous section, CMS membranes derived from Matrimid® and P84® provide the best separation performance for N_2/CH_4. Comparing the chemical structure of these two precursors with others, it was noticed that Matrimid® and P84® share the same dianhydride BTDA. Another similar feature between Matrimid® and P84® is that there is a random connection point between benzene ring and amine group in the diamines – the diamine used for synthesis is a mixture of meta and para diamines. These alternative connecting points are marked in Figure 5.4.

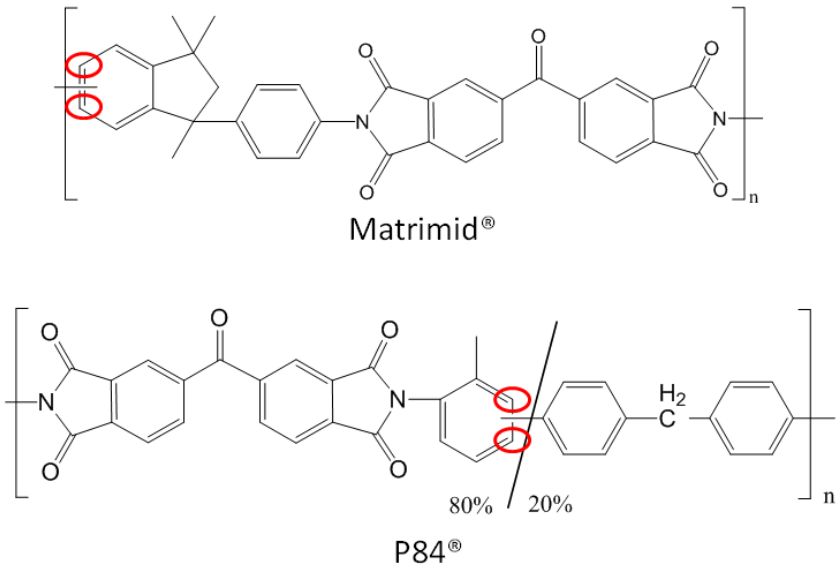

Figure 5.4: Alternative connecting points between benzene ring and amine group in the diamine part of Matrimid® and P84®.

To extend the superior separation performance of CMS membranes derived from Matrimid® and P84®, two other polyimides with similar structure, i.e. BTDA-a/sMDA and BTDA-MDA, were designed and synthesized. The "a" and "s" mean asymmetric and symmetric amine groups in the diamine, respectively. The symmetric MDA is one of the diamines used in P84® synthesis. The dianhydride BTDA is also the same as that used for the synthesis of both Matrimid® and P84®. The chemical structures of dianhydride BTDA and diamines aMDA and sMDA are shown in Figure 5.5. The reactions involved in the polyimide synthesis are shown in Figure 5.6.

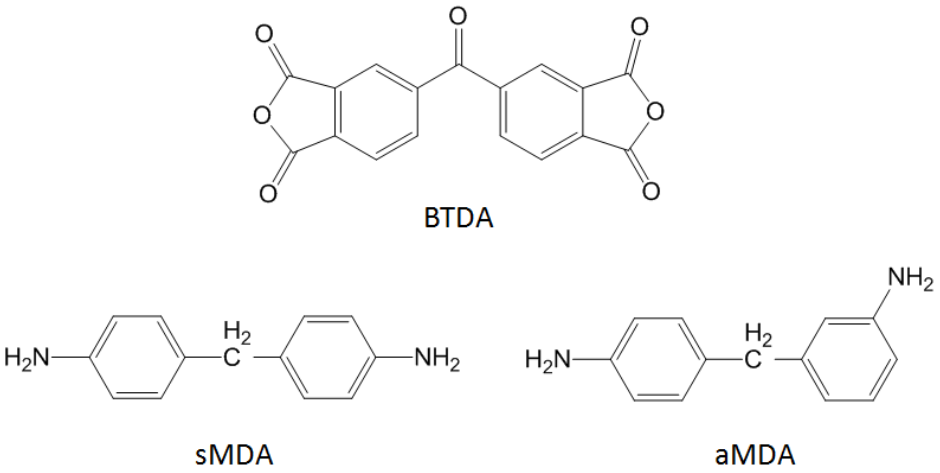

Figure 5.5: Chemical structures of dianhydride BTDA and diamines aMDA and sMDA used for polymer synthesis.

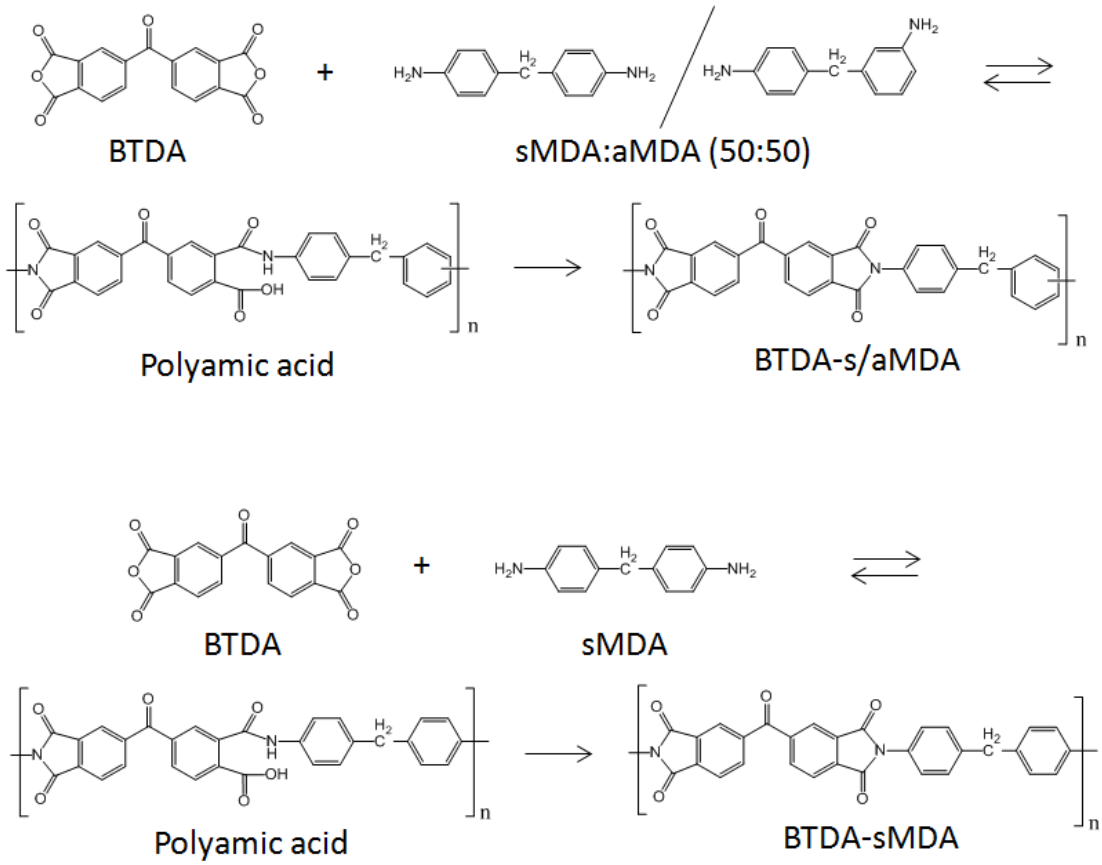

Figure 5.6: Chemical reaction process for the synthesis of BTDA-s/aMDA and BTDA-sMDA.

Before synthesis, both dianhydride and diamines were dried in a vacuum oven to remove moisture. BTDA has a melting point of 220-226 ℃. It was dried at 150 ℃ for 2 days. Diamines tend to be more unstable than dianhydrides. The melting points of sMDA and aMDA are 91.0-94.0 and 84.0-90.0 ℃, respectively. So they were dried at 50 ℃ for 2 days in vacuum oven. NMP was used as the solvent during synthesis and it was dehydrated by contacting with molecular sieves for 3 days.

The synthesis of polyimides is a two step process. The first step involves stoichiometric amounts of dianhydrides reacting with diamines to form a polyamic acid. sMDA or 50:50 sMDA/aMDA mixture were first dissolved in the dehydrated NMP in the reaction flask. The total monomer (including both dianhydride and diamine) concentration in NMP was controlled at 20 wt%. After all the diamine was dissolved under stirring at room temperature, dianhydride BTDA were added into the reaction flask in three portions to reach the final 1:1 stoichiometric ratio between dianhydride and diamine. The thick yellow transparent polymer solutions were observed during this first step. The reaction was allowed to continue for 24 hours.

The second step is the chemical imidization which involves the ring closing of amic acid with the presence of acetic anhydride (AcAn) and picoline. 5 mL picoline and 46 mL AcAn were slowly added into the reaction flask by syringe. The transparent polymer solution started to become unclear as reaction proceeded and a column of solid yellow polymer appeared as the chemical imidization proceeded for 24 hours during this step. The obtained solid pieces of polyimide were ground to powder/small flakes in a mixer. A methanol wash and vacuum filtration were applied before drying. The rinsed polyimides were first dried at room temperature in the fume hood for 24 hours and then dried at 120 ℃ in a vacuum oven. The final polyimide products were a mixture of powder and small flakes in the color yellow.

5.5 Dense Film Preparation for BTDA-s/aMDA and BTDA-sMDA

The synthesized BTDA-s/aMDA and BTDA-sMDA polyimides could not be easily dissolved in regular solvents at room temperature. Though they could be dissolved in hot NMP, the traditional solution casting method was not successful for these polymers since it was difficult to control the NMP evaporation rate to obtain flat and uniform dense films. Instead, melt pressing method was used to prepare dense films from these two polyimides.

To determine the melt pressing temperature, differential scanning calorimetry (DSC) was used to measure the glass transition temperature (T_g) of the synthesized polyimides. Heat-cool scans were recorded between -60 and 360 ℃ with a ramp rate of 10 ℃/min. The T_g was determined by the half-C_p extrapolated tangent method on the second heat cycle (Figure 5.7) to avoid noise of unrelaxed stress in the sample. The T_g's of BTDA-s/aMDA and BTDA-sMDA were determined to be 263 and 292 ℃, respectively. Thus the melt pressing temperature was chosen to be above such values.

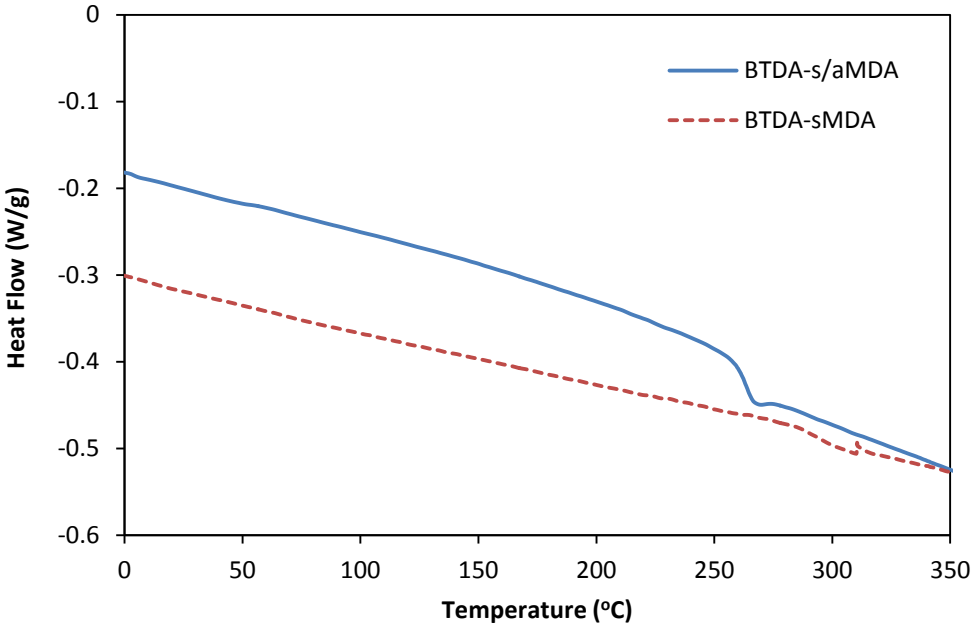

Figure 5.7: DSC scan of the second heating cycle for BTDA-s/aMDA and BTDA-sMDA.

Melt pressing temperatures between 300 and 350 ℃, preheating time between 0 to 4 min, pressing time between 30 sec and 1 min, and pressure between 20 and 35 ton were tried to make transparent and uniform dense films. High temperature, high pressure and long time resulted in polymer decomposition reflected by the color change and smell; while low temperature, low pressure and short time might not be adequate to allow the polymer chains to relax and form the film morphology. The optimized melt pressing condition was determined to be 325 ℃, 2 min preheat, and 30 sec pressing at 30 ton. The obtained film thickness was 165-175 μm, which was about twice the thickness of solution cast films.

5.6 Separation Performance of BTDA-s/aMDA and BTDA-sMDA CMS Dense Films

The obtained polymer dense films of BTDA-s/aMDA and BTDA-sMDA were pyrolyzed at 800 ℃ and soaked for 2 hours under UHP Ar. Resulting CMS dense films were tested for pure gas permeation. Since the film thickness of these two CMS membranes was about twice of the thickness of other CMS samples, much longer permeation time was required to ensure at least 6 times of time lag have passed during permeation. The permeation results of N_2, CH_4, O_2 and CO_2 are shown in Table 5.5.

Table 5.5: Permeation results of 800 ℃ CMS dense films pyrolyzed from BTDA-s/aMDA and BTDA-sMDA (tested at 35 ℃ and 65 psia feed pressure).

	Permeability (Barrer)				Selecitivity			
	N_2	CH_4	O_2	CO_2	N_2/CH_4	O_2/N_2	CO_2/CH_4	CO_2/N_2
BTDA-s/aMDA	3.85	0.64	28.6	108	5.98	7.43	169	28.3
BTDA-sMDA	5.61	1.01	53.6	209	5.59	9.55	208	37.2

It is observed that both CMS membranes provide attractive separation performance for all these gas pairs. The N_2/CH_4 separation performances of these two samples together with other 800 ℃ pyrolyzed CMS membranes studied in this work are shown in Table 5.6 and Figure 5.8. Though CMS membranes derived from BTDA-s/aMDA and BTDA-sMDA do not provide superior N_2/CH_4 separation capability vs. Matrimid® and P84® CMS, their separation performance is still much higher than all polymer membranes and all other CMS membranes studied in this work.

Table 5.6: Permeation results of 800 ℃ CMS dense films derived from several polymer precursors.

Precursor	N_2 Permeability (Barrers)	CH_4 Permeability (Barrers)	N_2/CH_4 Permselectivity
BTDA-s/aMDA	3.85	0.64	6.02
BTDA-sMDA	5.61	1.01	5.55
Matrimid®	6.78	0.88	7.70
P84®	6.42	0.81	7.93
Kapton®	0.92	0.14	6.57
Torlon®	0.99	0.15	6.60
6FDA:BPDA-DAM	25.0	16.9	1.48
6FDA-DAM	32.1	19.2	1.67
6FDA-mPDA	26.4	20.4	1.29

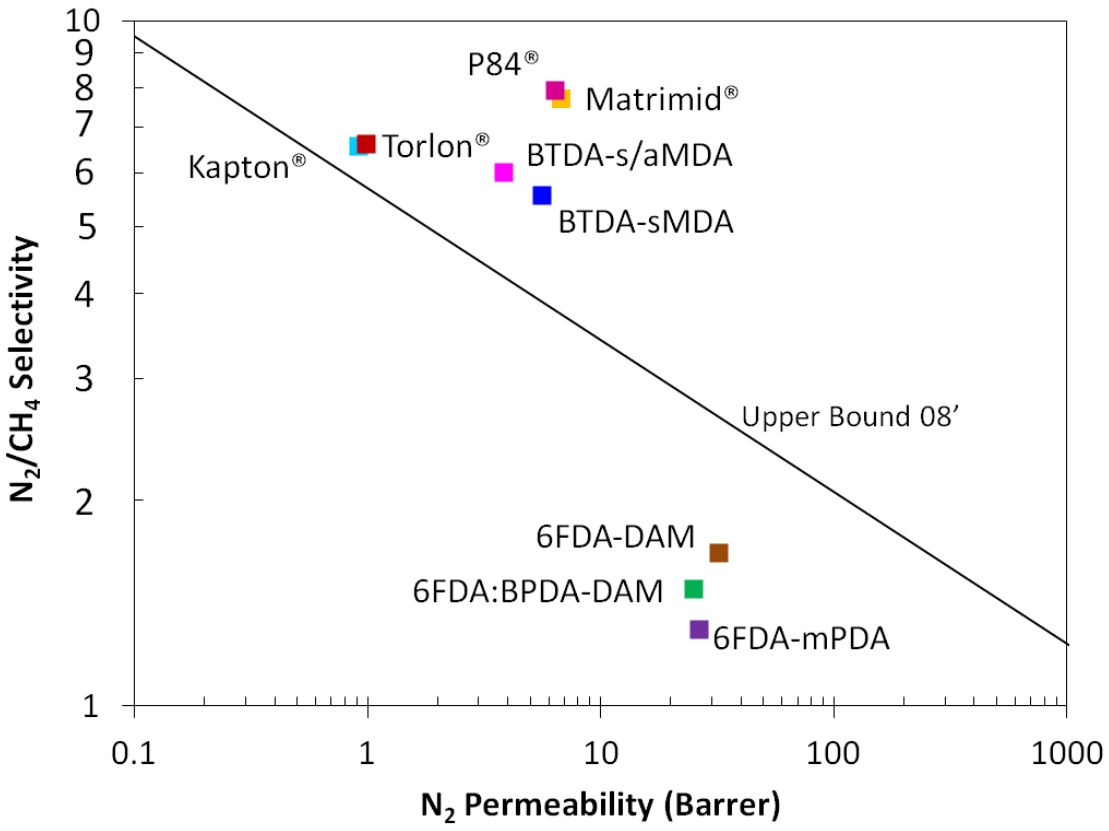

Figure 5.8: Plot of permeation results of 800 ℃ CMS dense films derived from all polymer precursors studied in this work. The data points of Matrimid®/P84® and Kapton®/Torlon® are partially overlapping to each other.

5.7 Comparison of CMS Membranes Derived from Different Polymer Precursors

Several properties of the polymer precursors studied here are characterized or cited from literature. The density, glass transition temperature (T_g), and fractional free volume (FFV) of these polymers are listed in Table 5.7. The densities of the polymer precursors were determined using a density gradient column. The T_g was determined by

DSC or cited from literature. The FFV of glass polymer membranes is the ratio of volume in the membrane that is not occupied by polymer chains. The FFV values shown in Table 5.7 were estimated by group contribution theory. This method was first presented by Bondi [16], and was further developed by van Krevelen [17] and Park and Paul [18]. In this method, the experimental specific volume of a polymer was compared with the van der Waals volume to determine the unrelaxed free volume using the following equation.

$$FFV = \frac{(V - V_0)}{V} \tag{5.1}$$

where V is the specific volume of the polymer and is calculated as the repeat unit mass divided by the polymer density, V_o is the volume occupied by the polymer chains and is calculated by the following equation.

$$V_0 = 1.3\sum V_w \tag{5.2}$$

where V_w is the van der Waals volume of a "group" comprising the repeat unit. The values of V_w for different groups are available in literature [17].

The high FFV values of the three 6FDA polymers are mainly due to the presence of bulky CF_3 groups. The van der Waals volume of a CF_3 group is about 56% more than that of a CH_3 group (21.3 vs. 13.67 cm^3/mol). The fact that two such bulky CF_3 groups are attached to the same quaternary carbon significantly increases the steric hindrance and inhibits chain packing. This leads to more unoccupied volume in the polymer matrix and high FFV value.

The exceptionally low FFV value of Torlon® presumably reflects its polyamide-imide (PAI) backbone, instead of polyimides as for other precursors. While aromatic polyimides have two heterocyclic rings in one repeat unit, there is only one heterocyclic ring in PAI, which greatly reduce the steric hindrance and FFV value. Torlon® CMS

membrane maintained the highly densely packed structure from the precursor even after pyrolysis. Though the N_2/CH_4 selecitivity is quite high, the Torlon® CMS membrane is much less permeable than most other CMS membranes.

Table 5.7: Properties of polymer precursors.

Precursor	Density (g/cm^3)	T_g (°C)	FFV
BTDA-s/aMDA	1.36	263	0.097
BTDA-sMDA	1.35	292	0.103
Matrimid®	1.25	305	0.139
P84®	1.31	315 [7]	0.141
Kapton®	1.42	385	0.098
Torlon®	1.45	275 [19]	0.067
6FDA:BPDA-DAM	1.32	425	0.152
6FDA-DAM	1.33	395	0.190
6FDA-mPDA	1.45	304 [20]	0.175

Comparing the data in Table 5.6 and 5.7, it is found that there is no strong correlation between polymer density and separation performance, or T_g and separation performance. However, there seems to be a correlation between FFV and separation performance. The three poorest performing CMS membranes derived from 6FDA polymers all have relatively high FFV values in the precursors, whereas all the other CMS membranes with performance above the upper bound line are pyrolyzed from precursors with lower FFV values. The correlation between precursor FFV and N_2/CH_4

selecitivity of resulting CMS membrane is shown in Figure 5.9. The cutoff FFV value between above upper bound CMS membranes and below upper bound CMS membranes is ~0.15. High FFV value indicates inhibition of intersegmental packing of polymer chains. And this generally results in an increase in the permeation rate of all penetrants through polymer membranes, together with a decrease in the diffusion selectivity and permselectivity [21]. The level of packing density of polymer chains can be somewhat maintained after pyrolysis, as several previous studies showed that precursors with higher permeability and lower selectivity usually result in more permeable and less selective CMS membranes [22-24].

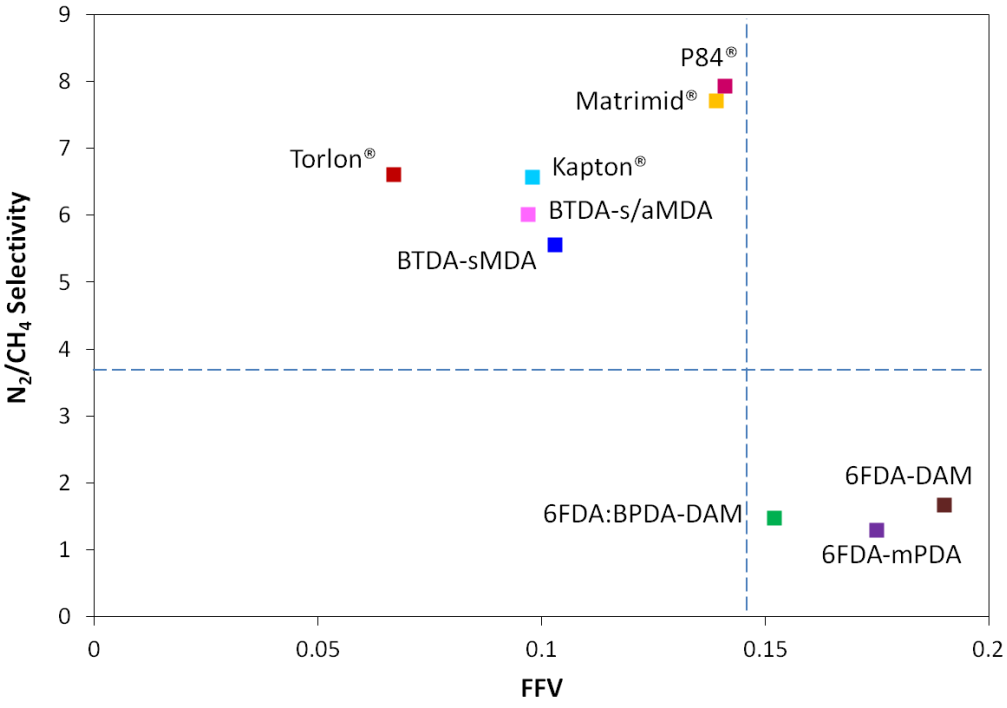

Figure 5.9: Correlation between precursor FFV and N_2/CH_4 selecitivity of resulting CMS membrane.

Though FFV reflects polymer chain packing density and is useful to provide general estimation of the separation capability of resulting CMS membranes, there is still other information that needs to be considered with regards to the structure of polymer matrix. One example is the alternating connection points within the polymer main chain and the sequence of copolymer. Matrimid®, p84®, and BTDA-s/aMDA all have mixed meta and para diamines in their structures, while P84®, Torlon®, and 6FDA:BPDA-DAM are copolymers. The sequence of isomers and copolymers can affect the shape of polymer chain and thus affect the long range chain packing. This effect is not considered by the FFV study, which only focuses on local occupied volume. Another example is the alignment of polymer chains. Since Kapton® is biaxially stretched during fabrication, the polymer chains are usually well aligned and densely packed in Kapton® films. This also explains the extremely low N_2 permeability in Kapton® CMS membrane.

The C, H, N, O and F element wt% in the polymer precursors and resulting CMS are listed in Table 5.8 and 5.9. The element wt% in polymer was calculated by the chemical repeat unit formula, and the element wt% in CMS was obtained from elemental analysis using combustion/TC, IR and Ion Chromatography. It can be seen that the C% significantly increases after pyrolysis. H%, O% and F% decreases as CO, CO_2, CH_4, H_2 and CHF_3 are released from the matrix during pyrolysis. As shown in Figure 4.10, N_2 does not start to leave until above 750 ℃. So N% does not change much after pyrolysis. For the three 6FDA polymers, the presence of bulky CF_3 groups not only increases FFV and inhibits chain packing in the precursor, but also contributes to the open structure in CMS. According to the elemental analysis, almost all F is removed during pyrolysis. While the bulky CHF_3 groups take large occupied volume in the precursor polymer, they

leave an open structure and prevent carbon lamellae packing as they are released from the matrix during pyrolysis.

Table 5.8: Element weight percentage in polymer precursors.

Precursor	C%	H%	N%	O%	F%
BTDA-s/aMDA	74.38	3.31	5.79	16.53	0.00
BTDA-sMDA	74.38	3.31	5.79	16.53	0.00
Matrimid®	76.09	4.35	5.07	14.49	0.00
P84®	71.46	3.02	6.62	18.90	0.00
Kapton®	69.11	2.62	7.33	20.94	0.00
Torlon®	70.16	3.29	8.53	18.03	0.00
6FDA:BPDA-DAM	65.84	3.31	5.80	13.25	11.80
6FDA-DAM	60.22	2.87	5.02	11.47	20.43
6FDA-mPDA	58.14	1.94	5.43	12.40	22.09

Table 5.9: Element weight percentage in 800 ℃ pyrolyzed CMS membranes.

Precursor	C%	H%	N%	O%	F%
BTDA-s/aMDA	92.80	0.95	4.88	1.37	0.00
BTDA-sMDA	94.43	0.70	3.41	1.46	0.00
Matrimid®	94.39	0.82	2.74	2.05	0.00
P84®	90.77	0.79	5.34	3.10	0.00
Kapton®	90.84	0.95	5.62	2.59	0.00
Torlon®	90.08	0.84	6.83	2.25	0.00
6FDA:BPDA-DAM	92.62	0.70	3.89	2.66	0.14
6FDA-DAM	90.25	0.97	6.13	2.37	0.28
6FDA-mPDA	89.96	0.94	6.62	2.36	0.13

5.8 Selection of Precursor for N_2/CH_4 Separation

From the above discussion, it is noticed that for the separation of similar-sized gas pair of N_2/CH_4, the 6FDA series of polymer precursors with bulky CF_3 groups and high FFV does not provide satisfying selectivity (<2) in 800 ℃ pyrolyzed CMS membranes, due to the open structure in both polymer and CMS. All other non-fluorinated precursors with lower FFV provide much higher N_2/CH_4 selecitivity (>5) after 800 ℃ pyrolysis. The Torlon® CMS cannot provide satisfying N_2 permeability due to the extremely low FFV and the too densely packed structure in the precursor. Kapton®, BTDA-s/aMDA and BTDA-sMDA have similar FFV values around 0.10. However, due to the orientation during the fabrication process, the polymer chains in Kapton® are much better aligned and more densely packed than the other two, resulting in higher N_2/CH_4 selectivity but much lower N_2 permeability in CMS. The 800 ℃ pyrolyzed P84® and Matrimid® CMS membranes provide the best separation performance for this gas pair, with the highest N_2/CH_4 selectivity and a satisfying N_2 permeability. These two precursors have similar chemical structures with the same dianhydride of BTDA. The FFV values of these two precursors are around 0.14 and lie in the middle of the FFV range of all studied precursors. While there might be other unstudied precursors with superior N_2/CH_4 separation performance after pyrolysis compared to Matrimid® and P84®, the discussion in this chapter will be a useful guidance for the initial precursor selection. A general conclusion for the N_2/CH_4 CMS membrane precursor selection is that 6FDA series polymers should be avoided, and a middle level polymer chain packing density with FFV around 0.14 might provide a good combination of permeability and selectivity.

5.9 Summary

The effect of polymer precursor on the resulting 800 ℃ pyrolyzed CMS membrane for N_2/CH_4 separation is discussed in this chapter. The permeation, sorption, and diffusion selection effects of Matrimid® and 6FDA:BPDA-DAM CMS membranes are compared in details. It is shown that the sizes of both ultramicropores and micropores in 6FDA:BPDA-DAM CMS is much larger than that in Matrimid® CMS, leading to a more permeable but poorly selective 6FDA:BPDA-DAM CMS membrane. Several other polymer precursors of P84®, Kapton®, Torlon®, 6FDA-DAM, 6FDA-mPDA and two self-synthesized polyimides BTDA-s/aMDA and BTDA-sMDA were also pyrolyzed at 800 ℃ and tested for permeation. Several properties of the polymer precursors especially FFV values were compared and correlated to the resulting CMS membrane separation performance. It is concluded that precursors with high FFV generally result in more permeable but less selective CMS membranes. While other factors affecting the polymer chain packing should also be considered, FFV value provides a relatively easy and quantifiable measurement for the estimation of CMS separation capability. Though 6FDA polymers are proved to be attractive CMS precursors for many other gas pairs, they cannot provide satisfying molecular sieving effect for the similar-sized N_2/CH_4 with its open structure. Precursors with very low FFV or too densely packed polymer chain environment like Torlon® and Kapton® are not preferred since N_2 permeability in the resulting CMS membranes is too low. CMS membranes pyrolyzed at 800 ℃ from Matrimid® and P84® that have mid-level FFV values and intermediate polymer chain packing provide the best separation performance among all the studied precursors.

5.10 References

[1] Lie JA, Hägg M-B. Carbon membranes from cellulose: Synthesis, performance and regeneration. J Membr Sci 2006;284(1–2):79-86.

[2] Steel KM, Koros WJ. An investigation of the effects of pyrolysis parameters on gas separation properties of carbon materials. Carbon 2005;43(9):1843-56.

[3] Zhou J, Jin J, Haldeman AT, Wagener EH, Husson SM. Formation and characterization of perfluorocyclobutyl polymer thin films. J Appl Polym Sci 2013;129(6):3226-36.

[4] Yoshimune M, Haraya K. Flexible carbon hollow fiber membranes derived from sulfonated poly(phenylene oxide). Sep Purif Technol 2010;75(2):193-7.

[5] Tin PS, Chung T-S. Novel approach to fabricate carbon molecular-sieve membranes based on consideration of interpenetrating networks. Macromol Rapid Commun 2004;25(13):1247-50.

[6] Hosseini SS, Chung TS. Carbon membranes from blends of pbi and polyimides for n2/ch4 and co2/ch4 separation and hydrogen purification. J Membr Sci 2009;328(1–2):174-85.

[7] Tin PS, Chung T-S, Liu Y, Wang R. Separation of co2/ch4 through carbon molecular sieve membranes derived from p84 polyimide. Carbon 2004;42(15):3123-31.

[8] Barsema JN, Kapantaidakis GC, Van Der Vegt NFA, Koops GH, Wessling M. Preparation and characterization of highly selective dense and hollow fiber asymmetric membranes based on btda-tdi/mdi co-polyimide. J Membr Sci 2003;216(1–2):195-205.

[9] Li Y, Chung T-S, Huang Z, Kulprathipanja S. Dual-layer polyethersulfone (pes)/btda-tdi/mdi co-polyimide (p84) hollow fiber membranes with a submicron pes–zeolite beta mixed matrix dense-selective layer for gas separation. J Membr Sci 2006;277(1–2):28-37.

[10] Suda H, Haraya K. Gas permeation through micropores of carbon molecular sieve membranes derived from kapton polyimide. The Journal of Physical Chemistry B 1997;101(20):3988-94.

[11] Xu L. Carbon molecular sieve hollow fiber membranes for olefin/paraffin separations. Atlanta: Georgia Institute of Technology; 2012.

[12] Rungta M. Carbon molecular sieve dense film membranes for ethylene/ethane separations. Atlanta: Georgia Institute of Technology; 2012.

[13] Kiyono M, Williams PJ, Koros WJ. Effect of pyrolysis atmosphere on separation performance of carbon molecular sieve membranes. J Membr Sci 2010;359(1–2):2-10.

[14] Kiyono M, Williams PJ, Koros WJ. Effect of polymer precursors on carbon molecular sieve structure and separation performance properties. Carbon 2010;48(15):4432-41.

[15] Xu L, Rungta M, Brayden MK, Martinez MV, Stears BA, Barbay GA, et al. Olefins-selective asymmetric carbon molecular sieve hollow fiber membranes for hybrid membrane-distillation processes for olefin/paraffin separations. J Membr Sci;423-424(15):314-23.

[16] Bondi AA. Physical properties of molecular crystals, liquids, and glasses: John Wiley & Sons; 1968.

[17] Van Krevelen DW, Te Nijenhuis K. Properties of polymers: Their correlation with chemical structure; their numerical estimation and prediction from additive group contributions: Elsevier Science; 2009.

[18] Park JY, Paul DR. Correlation and prediction of gas permeability in glassy polymer membrane materials via a modified free volume based group contribution method. J Membr Sci 1997;125(1):23-39.

[19] Wang Y, Goh SH, Chung T-S. Miscibility study of torlon< sup>®</sup> polyamide-imide with matrimid< sup>®</sup> 5218 polyimide and polybenzimidazole. Polymer 2007;48(10):2901-9.

[20] Joly C, Le Cerf D, Chappey C, Langevin D, Muller G. Residual solvent effect on the permeation properties of fluorinated polyimide films. Sep Purif Technol 1999;16(1):47-54.

[21] Koros W, Coleman M, Walker D. Controlled permeability polymer membranes. Annual Review of Materials Science 1992;22(1):47-89.

[22] Park HB, Kim YK, Lee JM, Lee SY, Lee YM. Relationship between chemical structure of aromatic polyimides and gas permeation properties of their carbon molecular sieve membranes. J Membr Sci 2004;229(1–2):117-27.

[23] Geiszler VC. Polyimide precursors for carbon molecular sieve membranes. Austin TX USA: University of Texas at Austin; 1997.

[24] Kiyono M. Carbon molecular sieve membranes for natural gas separations. Atlanta: Georgia Institute of Technology; 2010.

CHAPTER 6

DEVELOPMENT OF CMS HOLLOW FIBERS FOR N_2/CH_4 SEPARATION

6.1 Overview

The pyrolysis conditions and polymer precursors were discussed in Chapter 4 and 5 based on fundamental studies of homogeneous dense CMS membranes. Though development of CMS hollow fiber was not initially proposed for this work, with the CMS dense films studied in the previous chapters providing attractive separation performance for N_2/CH_4, efforts were also made to move the good membrane material into a hollow fiber morphology. With the combination of a thin separation skin layer on the outer surface and a microporous support layer on the core side, asymmetric hollow fiber membranes not only provide higher mechanical strength, but also yield higher flux than dense films. In addition, the high surface area to volume ratio and high packing density in hollow fiber modules make it much more favorable in industry. Matrimid® was chosen as the polymer precursor for developing N_2/CH_4 CMS hollow fibers since this material provides superior separation performance in the dense film morphology and it is also well studied for hollow fiber spinning. The permeation performance of untreated 800 ℃ pyrolyzed Matrimid® CMS hollow fiber provided by other Koros group members will be presented and compared to the performance of corresponding dense film. However, it was found that the hollow fiber asymmetry could not be well maintained after pyrolysis at high temperature, leading to a great loss in permeance. A pretreatment method was

applied to overcome such problem. Detailed description of the pretreatment will be presented and N_2/CH_4 separation performance after such treatment will be shown.

6.2 Separation Performance of Neat Matrimid® CMS Hollow Fiber Membrane

CMS hollow fiber membranes for N_2/CH_4 have not been widely studied and only a few researchers have reported separation data of N_2 and CH_4. Kusuki et al. pyrolyzed BPDA-ODA:DDM hollow fiber at 700 ℃ and 850 ℃. Their data showed that the 700 ℃ CMS hollow fiber provided N_2 permeance of 6.3 GPU and N_2/CH_4 selectivity of 1.7 at 50 ℃; while the 850 ℃ CMS hollow fiber provided N_2 permeance of 0.33 GPU and N_2/CH_4 selectivity of 3.2 at 50 ℃ [1]. Favvas et al. pyrolyzed P84® at 900 ℃ and showed that the CMS hollow fiber provided N_2 permeance of 64.5 GPU and N_2/CH_4 selectivity of 0.91 at 40 ℃, and N_2 permeance of 200 GPU and N_2/CH_4 selectivity of 2.7 at 100 ℃ [2]. Compared with the 800 ℃ P84® CMS dense film data shown in Chapter 5, it is believed that the hollow fiber studied in this reference must have defects and be controlled by Knudsen diffusion and even viscous flow, considering the low selectivity and the fact that their hollow fiber precursor only provided N_2/CH_4 and O_2/N_2 selectivities both around 1 at all tested temperatures at 40, 60, and 100 ℃. Xu et al. showed that their thin-walled Matrimid® hollow fiber pyrolyzed at 675 ℃ provided N_2 permeance of 1.07 GPU and N_2/CH_4 selectivity of 2.9 at 35 ℃.

The Matrimid® hollow fibers studied in this work were prepared by group members Liren Xu and Nitesh Bhuwania using the method called spinning. Hollow fiber spinning was conducted by first making a polymer solution, commonly called “dope”.

The dope composition was developed by previous group member and is shown in Table 6.1 [3].

Table 6.1: Dope composition of defect-free asymmetric Matrimid® hollow fiber spinning [3].

Component	wt%
Matrimid®	26.2
NMP	53
THF	5.9
Ethanol	14.9

As described in Chapter 3, dry jet/wet quench method was used to spin the dope into hollow fibers. Table 6.2 shows the spinning conditions used for defect-free fiber production. After spinning, the fibers were solvent exchanged in methanol and hexane and dried in vacuum oven at 75˚C for at least 2 hour.

Table 6.2: Spinning conditions for defect-free asymmetric Matrimid® hollow fiber membranes [3, 4].

Spinning parameter	Value
Dope flow rate	180 ml/hr
Bore fluid flow rate	60 ml/hr
Take-up rate	50 m/min
Quench bath temperature	25 ℃
Spinneret temperature	50 ℃
Air gap height	2.5-18.5 cm

Similar to CMS dense film membranes, CMS hollow fibers were also pyrolyzed under inert gas purging under controlled temperature protocol. The same 800 ℃ protocol described in Chapter 3 was used for CMS hollow fibers. The only differences for hollow fiber pyrolysis were that a three-zone temperature controlled furnace instead of the one-zone furnace was used, and the supporting quartz plate was replaced by a metal mesh plate in the quartz tube. Details of the pyrolysis setup were described in Chapter 3.

The permeation data of Matrimid® CMS hollow fiber pyrolyzed at 800 ℃ and soaked for 2 hour under UHP Ar are listed in Table 6.3, with comparison to the dense film data. The N_2 permeability of CMS hollow fiber was based on the hollow fiber wall thickness of 52.3 μm measured by SEM image (Figure 6.3) considering that the cross section of hollow fiber wall totally collapsed into a thick separation layer. The structure collapse and densification in CMS hollow fiber will be discussed in the next section. It was noticed that both the N_2 permeability and N_2/CH_4 selecitivity of CMS hollow fiber were lower than the values of CMS dense film. While the exact reason for these reductions unknown, it is believed that there might be certain small defects in the complex hollow fiber morphology. In addition, the polymer chain arrangement in hollow fibers may be different from dense films since fibers are processed through extrusion and films are prepared by solution casting. These all make the comparison of separation properties between dense film and hollow fiber complicated. Further investigation needs to be conducted. Nevertheless, the achieved N_2/CH_4 selectivity is still attractive and higher than other reported hollow fiber membranes. However, the N_2 permeance needs to be largely improved to enable economic industrial application.

Table 6.3: Permeation data of Matrimid® CMS hollow fiber pyrolyzed at 800 ℃ and soaked for 2 hour under UHP Ar. Tested at 35 ℃ 65 psia feed pressure.

	N_2 Permeance (GPU)	N_2 Permeability (Barrer)	N_2/CH_4 Selecitivity
Hollow Fiber	0.091	4.81	5.8
Dense Film	-	6.78	7.7

The 800 ℃ Matrimid® CMS hollow fiber was also tested with higher feed pressures up to 700 psia. The N_2 permeance and N_2/CH_4 selectivity trend with feed pressure are shown in Figure 6.1 and 6.2. It was noticed that neither permeance nor selectivity changed significantly at higher pressures. In polymer membranes, plasticization sometime occurs when sorbed penetrants reach a certain concentration and dilates the polymer matrix. This can result in an increase in chain mobility and gas permeance but reduction in selectivity. With the rigid structure, carbon lamellae do not dilate in CMS membranes and no plasticization has been observed in CMS hollow fibers. Also, the results proved that CMS hollow fibers have quite good mechanical strength and can withstand quite high feed pressure, which is important for natural gas processing since the wellhead pressure is usually several hundred psia and may reach above 1000 psia.

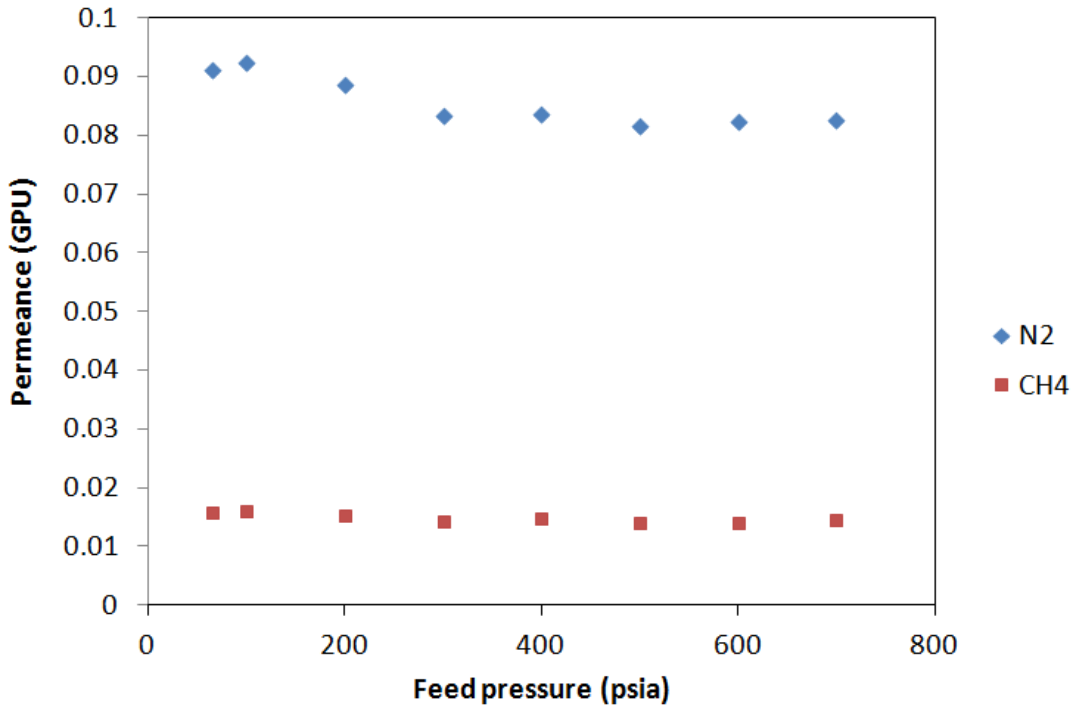

Figure 6.1: N_2 and CH_4 permeance of Matrimid® CMS hollow fiber pyrolyzed at 800 ℃ and soaked for 2 hour under UHP Ar, tested at 35 ℃ with feed pressure from 65 to 700 psia.

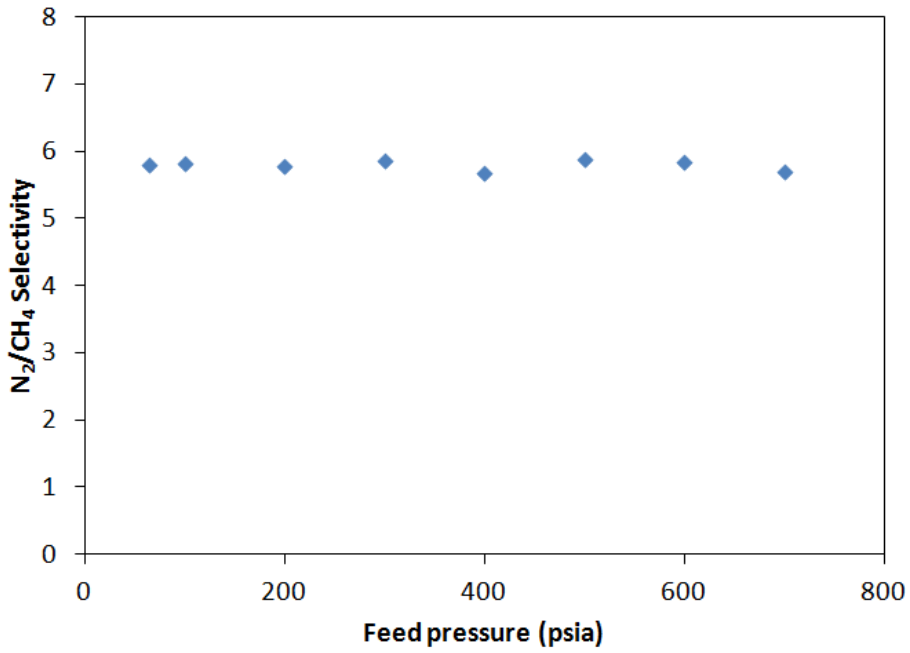

Figure 6.2: N_2/ CH_4 selecitivity of Matrimid® CMS hollow fiber pyrolyzed at 800 ℃ and soaked for 2 hour under UHP Ar, tested at 35 ℃ with feed pressure from 65 to 700 psia.

6.3 Substructure Collapse in Asymmetric CMS Hollow Fiber Membrane

The previous section showed that though the 800 ℃ Matrimid® CMS hollow fiber provided high N_2/CH_4 selectivity, the N_2 permeance was far from satisfying for industrial application. To explain the extremely low permeance, SEM images of Matrimid® polymer hollow fiber and Matrimid® CMS hollow fiber are compared in Figure 6.3. From Figure 6.3 (a), it is clearly observed that the thickness of the dense skin layer is less than 1 μm and most part of the fiber wall is porous supporting substructure. However, after pyrolysis, the asymmetry of cross-sectional structure is totally lost and the whole cross-section of CMS fiber is dense and smooth, as indicated by Figure 6.3 (b).

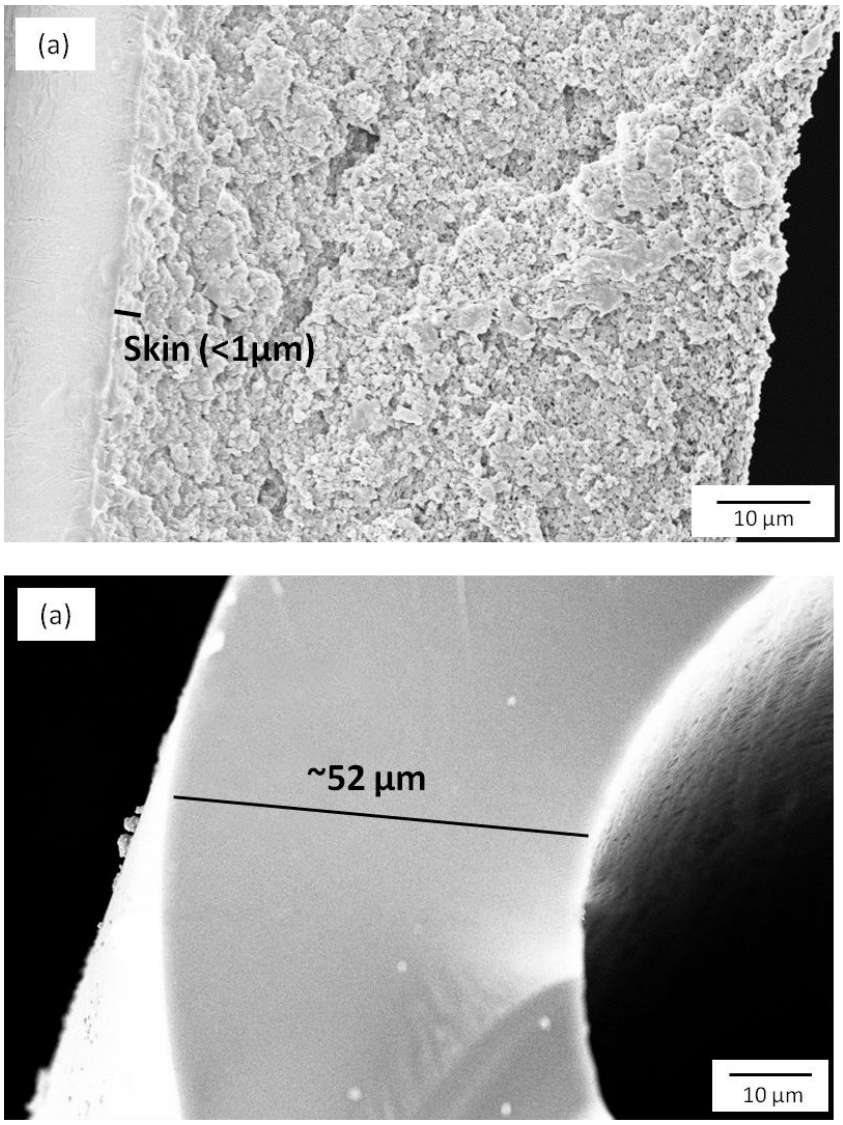

Figure 6.3: SEM images of (a) Matrimid® polymer hollow fiber, and (b) Matrimid® CMS hollow fiber pyrolyzed at 800 ℃ and soaked for 2 hour under UHP Ar.

Based on gas permeation data and the microscopic morphology obtained from SEM images, it is clear that the whole porous substructure on the bore side of hollow fiber precursor collapsed into a dense separation layer during pyrolysis. Such a large increase in the separation layer thickness greatly reduced the permeance of all gas penetrants. This kind of substructure collapse and densification were also observed in

lower temperature pyrolyzed Matrimid® CMS hollow fibers [5-7]. Xu et al. observed that 6FDA series polymers also exhibited substructure collapse but to a lower degree than Matrimid® due to their higher degree of rigidity. It is believed that the substructure collapse is triggered by polymer chain relaxation above glass transition temperature (T_g). As the temperature reached above T_g during pyrolysis, the polymer backbone segments were able to overcome the steric hindrance and enter a soft viscous state. Polymer chains started to move closer to each other to get more densely packed, resulting in the substructure morphology collapse before carbonization happens.

6.4 V-treatment of Matrimid® CMS Hollow Fiber for N_2/CH_4 Separation

6.4.1 V-treatment

To overcome the substructure collapse during the pyrolysis of Matrimid® hollow fiber, vinyltrimethoxy silane (VTMS) was applied as a "morphology stabilizer" to the precursor before pyrolysis. Bhuwania developed the so-called VTMS treatment (V-treatment) method for pyrolysis pretreatment and showed that it could effectively restrict substructure collapse and significantly improve CMS hollow fiber permeance for Matrimid® and 6FDA:BPDA-DAM CMS hollow fibers pyrolyzed at 550 and 650 ℃. In this work, the V-treatment was applied for 800 ℃ Matrimid® CMS hollow fiber and its effect of improving N_2/CH_4 separation performance is presented and discussed below.

VTMS is an organic alkoxy silane in the appearance of light yellow liquid. It can react with moisture at room temperature and undergo a sol-gel reaction to form a network of siloxane via hydrolysis and condensation of methoxy groups, as shown in Figure 6.4.

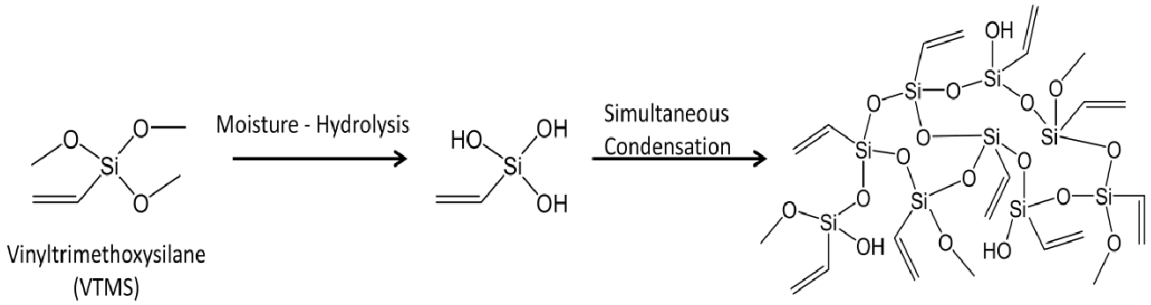

Figure 6.4: Sol-gel crosslinking reaction of VTMS in presence of moisture [7].

Before pyrolysis, the Matrimid® hollow fibers were first saturated with 100% VTMS liquid or 10% VTMS in hexane, and then exposed to ambient moisture (~30-40 %RH) at 25 ℃ for 24 hour. A layer of siloxane network was formed on the wall of pores in the fiber via the sol-gel reaction. The treated fibers were dried in vacuum oven at 150 ℃ for 12 hour before pyrolysis to remove unreacted VTMS (b.p.: 123 ℃) and moisture. There was no significant mechanical or appearance change after the V-treatment. The V-treated Matrimid® hollow fibers were pyrolyzed under the same conditions as the untreated fibers.

Compared to untreated Matrimid® CMS hollow fiber, both 100% and 10% V-treated Matrimid® CMS hollow fibers exhibited much better asymmetry, as shown in Figure 6.5. The thickness of separation layer suggested on the SEM images reduced from

52 μm in the untreated fiber to 8 and 7 μm in the 100% V-treated and 10% V-treated fibers, respectively. While densification still happened in the transition region under the skin layer and the outer side of the porous supporting layer due to the smaller pore sizes and shorter distances between polymer chains in those regions, the collapse and densification in most inner part of the porous supporting layer were significantly restricted.

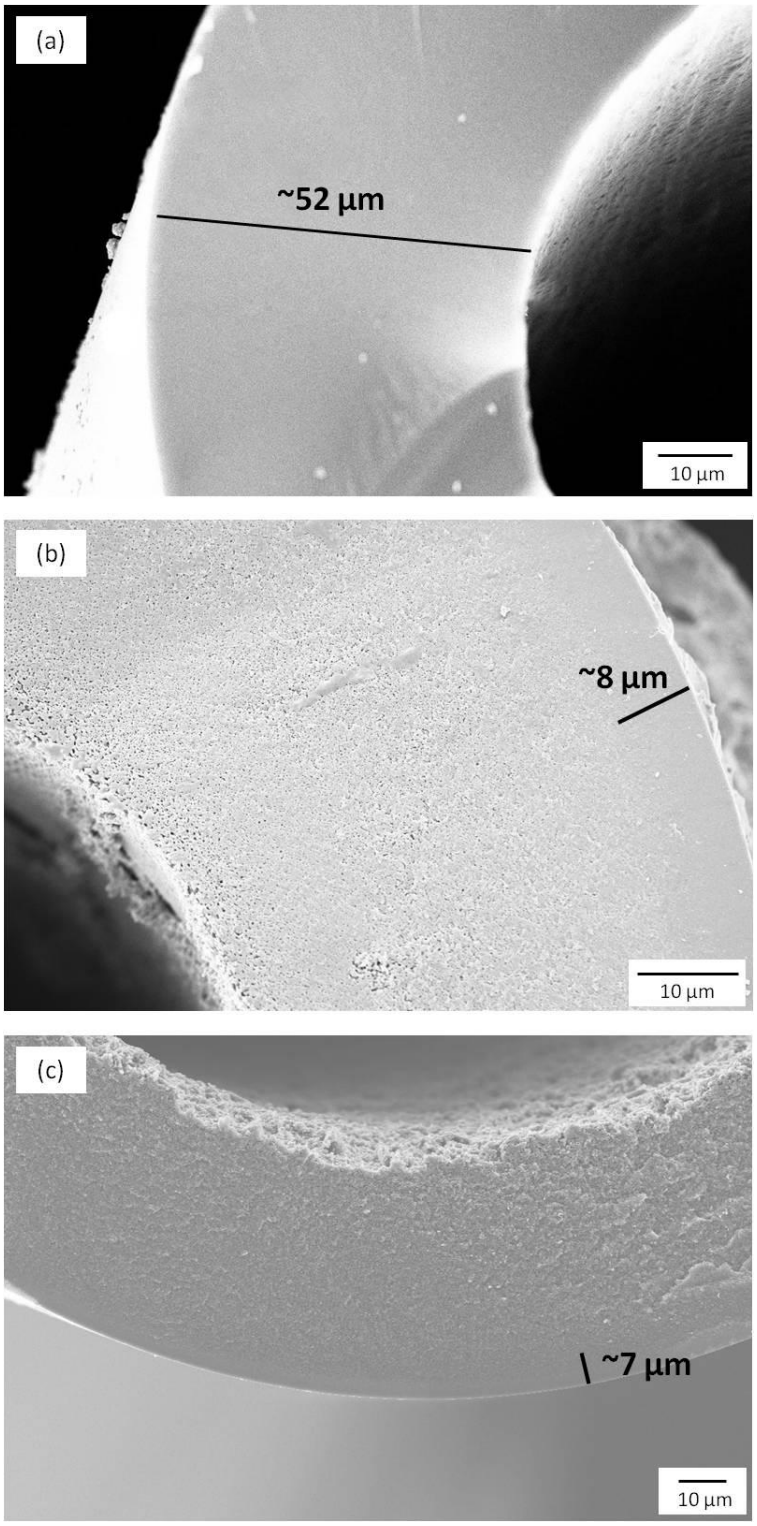

Figure 6.5: SEM images of (a) untreated 800 ℃ Matrimid® CMS hollow fiber, (b) 100% VTMS treated 800 ℃ Matrimid® CMS hollow fiber, and (c) 10% VTMS treated 800 ℃ Matrimid® CMS hollow fiber.

6.4.2 Separation Performance of V-treated Matrimid® CMS Hollow Fiber

Permeation tests for the 100% and 10% V-treated Matrimid® CMS hollow fibers were performed, and results are shown with comparison to untreated Matrimid® CMS hollow fiber in Table 6.4. It is observed that the permeance of both N_2 and CH_4 increased after V-treatment; however, the N_2/CH_4 selectivity was greatly reduced, especially for the 100% V-treatment. This result indicates that while the V-treatment effectively restricted the substructure collapse, the intrinsic separation property at the separation layer was also largely affected. As shown in Figure 6.6, N_2 permeance reached highest value at 10% V-treatment and CH_4 permeance monotonically increased with VTMS% in treatment. Since the permeance percentage increase for CH_4 was larger than that of N_2 at both V-treatment concentrations, the N_2/CH_4 selecitivity decreased with VTMS% in treatment, as shown in Figure 6.7.

Table 6.4: Permeation data of untreated, 10% V-treated and 100% V-treated Matrimid® CMS hollow fibers pyrolyzed at 800 ℃ and soaked for 2 hour under UHP Ar. Tested at 35 ℃ and 100 psia feed pressure.

	N_2 Permeance (GPU)	CH_4 Permeance (GPU)	N_2/CH_4 Selecitivity
Untreated CMS	0.091	0.016	5.8
10% V-treated CMS	0.153	0.037	4.1
100% V-treated CMS	0.108	0.083	1.3

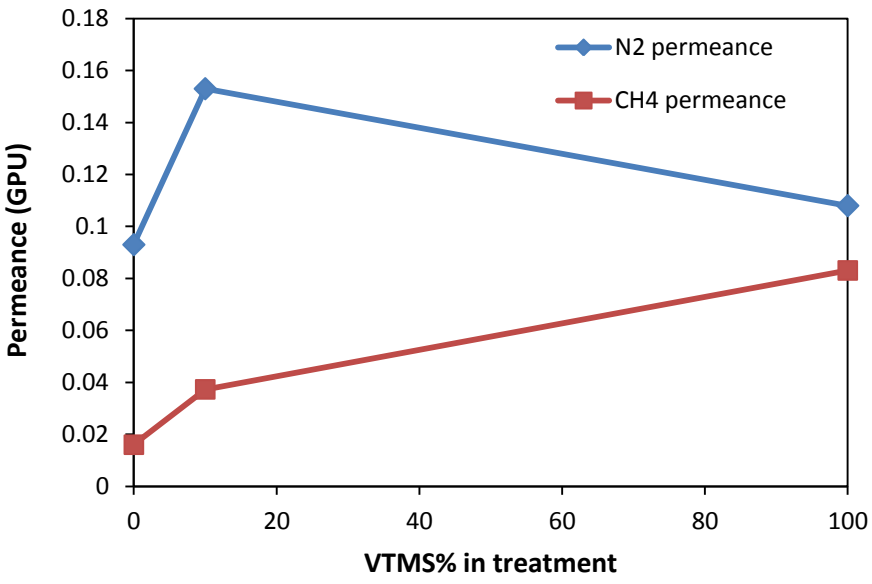

Figure 6.6: Effect of VTMS% on permeance for 800 ℃ Matrimid® CMS hollow fiber membrane (permeation was tested at 35 ℃ and 100 psia feed pressure; 0% VTMS represents untreated CMS hollow fiber).

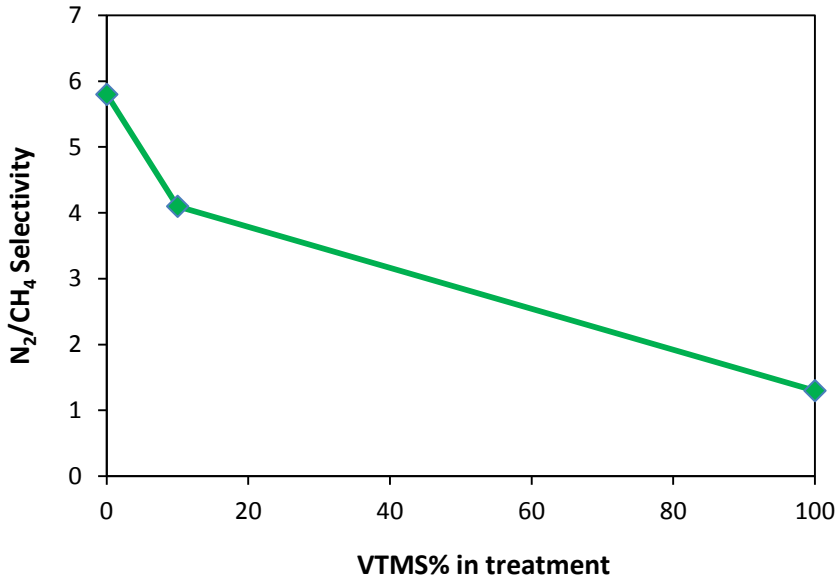

Figure 6.7: Effect of VTMS% on N_2/CH_4 selectivity for 800 ℃ Matrimid® CMS hollow fiber membrane (permeation was tested at 35 ℃ and 100 psia feed pressure; 0% VTMS represents untreated CMS hollow fiber).

To understand the property change in the separation layer, permeabilities of the CMS hollow fibers were estimated based on the separation layer thickness measured on the SEM images, and are shown in Table 6.5. As shown in Figure 6.8, both N_2 and CH_4 permeability decreased after V-treatment. While this figure shows that N_2 permeability monotonically decreased with VTMS% and CH_4 permeability reached a lowest value at 10% VTMS, it should be noted that the separation layer thickness measured by SEM may not accurately reflect the real thickness due to the complicated cross-sectional morphology and unclear boundary of separation layer. Nevertheless, it is quite clear that V-treatment reduced the permeability value, especially for N_2. It is concluded that V-treatment can not only improve substructure morphology, but also contribute adverse effect on the separation layer. The anti-collapse capability of V-treatment was undermined by its side effect on intrinsic separation property.

Table 6.5: Estimated permeability data of untreated, 10% V-treated and 100% V-treated Matrimid® CMS hollow fibers pyrolyzed at 800 ℃ and soaked for 2 hour under UHP Ar. Tested at 35 ℃ 100 psia feed pressure.

	Separation layer thickness (μm)	N_2 Permeability (Barrer)	CH_4 Permeability (Barrer)	N_2/CH_4 Selecitivity
Untreated CMS	52.3	4.86	0.83	5.8
10% V-treated CMS	7	1.07	0.26	4.1
100% V-treated CMS	8	0.86	0.66	1.3

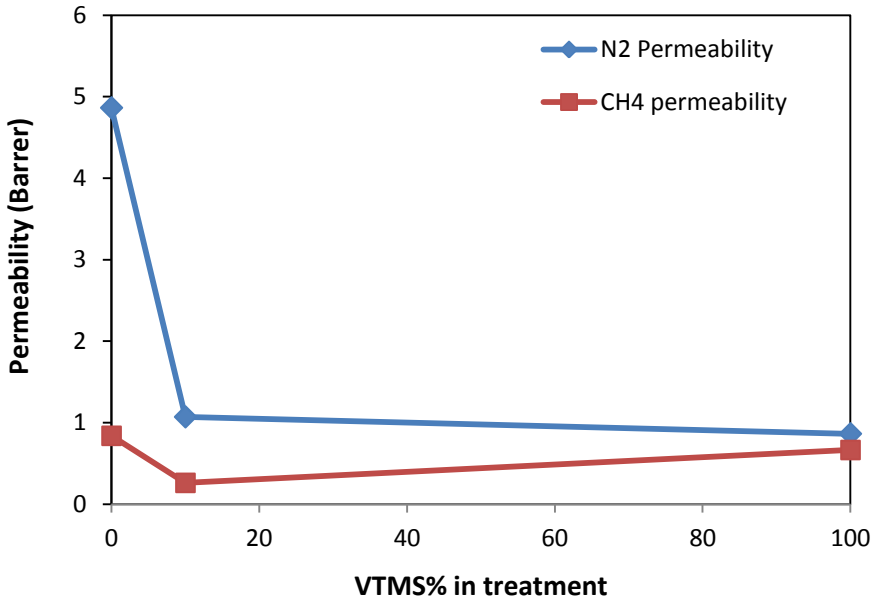

Figure 6.8: Effect of VTMS% on permeability for 800 ℃ Matrimid® CMS hollow fiber membrane (permeation was tested at 35 ℃ and 100 psia feed pressure; permeability was estimated by SEM measured separation layer thickness; 0% VTMS represents untreated CMS hollow fiber).

Previous study by Bhuwania showed that large amount of silica is accumulated on the outmost CMS skin and the silica concentration drops quickly from the surface to the inner layer of Matrimid® CMS hollow fiber pyrolyzed at 550 ℃ under UHP Ar, as shown in Figure 6.9 [7]. This figure also indicates that the silica concentration at the outmost layer of 10% V-treated CMS fiber is much less than the value of 100% VTMS treated CMS fiber. With the silica at% as high as 35 % at the fiber surface, it is hypothesized that the hollow fiber surface is fully covered by the siloxane network after V-treatment, especially for 100% VTMS treatment. The Si does not leave the fiber during pyrolysis and forms an additional layer of silica structure at elevated temperature. As a result, the separation performance of the CMS hollow fiber skin layer is significantly modified. It is hypothesized that the silica at the CMS hollow fiber surface has a relatively dense

structure and greatly reduces the permeation rate of all gas penetrants. The permeation of smaller sized and more permeable N_2 was more inhibited. So N_2 permeability drops more than CH_4 and N_2/CH_4 selectivity decreases after V-treatment. Since the silica concentration is lower for the 10% V-treated CMS hollow fiber, this adverse effect on intrinsic separation property is lower than the 100% V-treated hollow fiber.

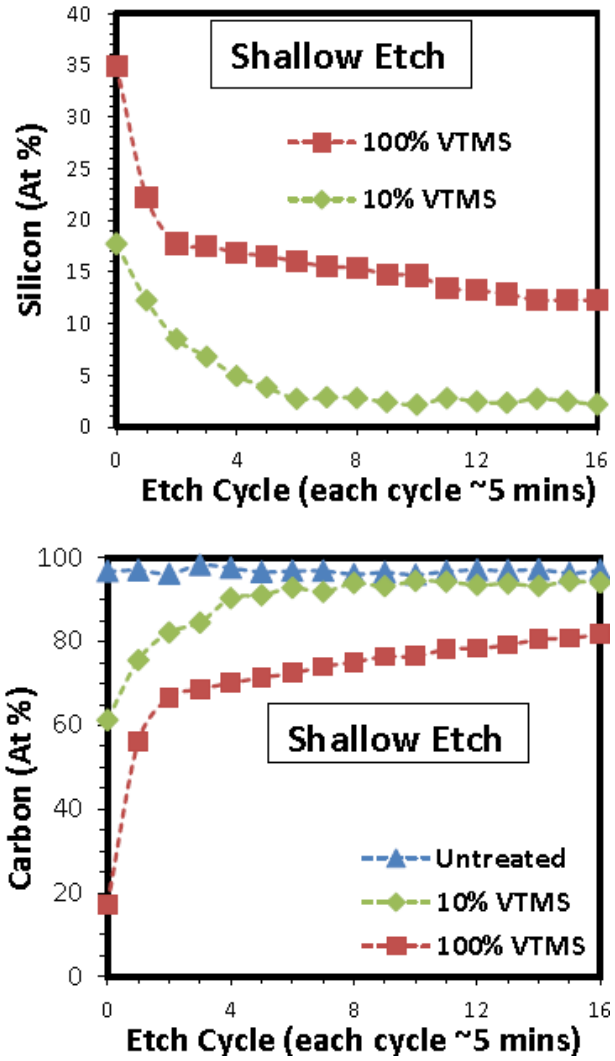

Figure 6.9: XPS surface composition profile for Si 2p and C1 as a function of sputter etch depth profiling time for Matrimid Effect of VTMS% on permeability for Matrimid® CMS hollow fiber pyrolyzed at 550 ℃ under UHP Ar. The etching depth is approximately less than 1 μm [7].

6.5 Summary

This chapter investigated the possibility of extending the good separation performance obtained from 800 ℃ pyrolyzed Matrimid® CMS dense film into hollow fiber morphology. The neat 800 ℃ Matrimid® CMS hollow fiber showed attractive N_2/CH_4 selectivity and the capability to withstand high feed pressure up to 700 psia without big loss in performance. However, the N_2 permeance of this CMS fiber was extremely low and is far from satisfying for industrial application. SEM images suggested that the Matrimid® hollow fiber lost all of it cross-sectional asymmetry during pyrolysis and the separation layer thickness greatly increased to the whole thickness of fiber wall. V-treatment was applied to the Matrimid® hollow fiber precursor as a pre-treatment to inhibit substructure collapse during pyrolysis. SEM images revealed that the hollow fiber asymmetry was much better maintained after this treatment and permeation tests showed that permeance was improved by the treatment. However, due to the adverse effect of silica on the surface of separation layer, N_2/CH_4 selectivity was reduced by the V-treatment at the same time. Using the separation layer thickness measured by SEM images, permeabilities of the separation layer were estimated. It was found that the adverse effect on the intrinsic separation performance in the skin layer was lower for the 10% VTMS treatment than the 100% VTMS treatment. Also, this adverse effect was surprisingly stronger for the smaller-sized N_2. As a result, the permeability decrease in N_2 was more than that in CH_4 and N_2/CH_4 selectivity was reduced after V-treatment.

6.6 References

[1] Kusuki Y, Shimazaki H, Tanihara N, Nakanishi S, Yoshinaga T. Gas permeation properties and characterization of asymmetric carbon membranes prepared by pyrolyzing asymmetric polyimide hollow fiber membrane. J Membr Sci 1997;134(2):245-53.

[2] Favvas EP, Kouvelos EP, Romanos GE, Pilatos GI, Mitropoulos AC, Kanellopoulos NK. Characterization of highly selective microporous carbon hollow fiber membranes prepared from a commercial co-polyimide precursor. J Porous Mater 2008;15(6):625-33.

[3] Clausi DT, Koros WJ. Formation of defect-free polyimide hollow fiber membranes for gas separations. J Membr Sci 2000;167(1):79-89.

[4] Xu L. Carbon molecular sieve hollow fiber membranes for olefin/paraffin separations. Atlanta: Georgia Institute of Technology; 2012.

[5] Kiyono M. Carbon molecular sieve membranes for natural gas separations. Atlanta: Georgia Institute of Technology; 2010.

[6] Xu L, Rungta M, Koros WJ. Matrimid® derived carbon molecular sieve hollow fiber membranes for ethylene/ethane separation. J Membr Sci 2011;380(1–2):138-47.

[7] Bhuwania N. Engineering the morphologhy of carbon molecular sieve (cms) hollow fiber membranes. Atlanta: Georgia Institute of Technology; 2013.

CHAPTER 7

CONCLUSIONS AND RECOMMENDATIONS

7.1 Summary and Conclusions

Nitrogen/methane separation using N_2-selective membranes is challenging and has not been widely studied. However, the N_2/CH_4 membrane separation is very attractive compared to the traditional cryogenic distillation and PSA processes due to its high energy efficiency and several other benefits, especially for the highly N_2-contaminated gas reserves. The bottleneck of N_2/CH_4 membrane separation is the lack of high-performing material to overcome the small size difference between N_2 and CH_4 and the competition effect between diffusion and sorption. The overarching goal of this project was to develop high-performing CMS membrane materials for N_2/CH_4 separation, interpret the separation mechanism, and provide guidance for future membrane development. The objectives described in Chapter 1 are summarized and the progress toward these objectives is reviewed below.

1. Analyze the effects of pyrolysis conditions to achieve high-performing CMS membranes for N_2/CH_4 separation.

The effects of pyrolysis conditions including pyrolysis temperature, soak time, oxygen/hydrogen doping were studied based on Matrimid® and 6FDA:BPDA-DAM CMS membranes. It was shown that pyrolysis temperature and oxygen doping were the two most effective factors to optimize CMS membrane separation performance. High pyrolysis temperature usually results in more densely packed carbon structure with tight

micropores and ultramicropores. Due to the small size difference between N_2 and CH_4, it was concluded that high pyrolysis temperature is essential to achieve high-performing N_2-selective CMS membranes. Oxygen doping was proved to be useful to fine tune the ultramicropore structure without a significant loss in permeability. The other two factors of soak time and hydrogen doping was less effective in tuning CMS pore structure and separation properties. Longer soak time resulted in reduced permeability but no obvious improvement in selectivity. Hydrogen doping did not show significant separation property change due to the poor hydrogen chemisorption onto carbon. While 6FDA:BPDA-DAM CMS membranes previously showed attractive separation performance for many other gas pairs, their performance for N_2/CH_4 was not satisfying and was below the polymer upper bound even at high pyrolysis temperature or after oxygen doping. On the other hand, Matrimid® CMS membranes provided better separation performance with much higher N_2/CH_4 selectivity though lower N_2 permeability. The 800 ℃ Matrimid® CMS membrane provided attractive separation performance well above the upper bound. Detailed permeation and sorption measurements revealed that the diffusion selection effect solely contributed to the high permselectivity. The diffusion selectivity was then further deconvoluted into an energetic factor and an entropic factor. Results showed that the entropic diffusion selectivity was extremely high in this high performing membrane sample. Transition state theory was applied to theoretically interpret this unique entropic contribution in CMS membranes with tight ultramicropore structure.

2. Analyze different polymers as precursors to CMS dense film membranes for N_2/CH_4 separation

The effect of polymer precursor was studied on CMS dense films pyrolyzed at 800 ℃ for 2 hour soak under UHP Ar. A series of different polymer precursors, including Matrimid®, P84®, Kapton®, Torlon®, BTDA-s/aMDA and BTDA-sMDA, 6FDA:BPDA-DAM, 6FDA-DAM, and 6FDA-mPDA were pyrolyzed and tested for N_2/CH_4 permeation. BTDA-s/aMDA and BTDA-sMDA were successfully synthesized and made into CMS dense films for performance evaluation and hypothesis development. Results showed that all CMS membranes derived from non-6FDA polymers gave separation performance above the upper bound, and the three 6FDA polymers gave poor separation performance below the upper bound with N_2/CH_4 selectivity below 2. The CMS membrane separation performance for N_2/CH_4 was correlated with the free fractional volume (FFV) of the polymer precursor. It was found that 6FDA polymers with high FFV values cannot provide strong molecular sieving effect due to the open structure both before and after pyrolysis. The void space left from bulky CF_3 groups in 6FDA polymers inhibits carbon lamellae packing. On the other hand, polymers with too low FFV values or too densely packed polymer matrix like Torlon® and Kapton® resulted in extremely low permeability but good N_2/CH_4 selectivity. Among all the precursors studied, CMS dense film pyrolyzed from Matrimid® and P84® exhibited best combination of N_2 permeability and N_2/CH_4 selectivity.

3. Extend the high performance obtained from CMS dense films to CMS hollow fiber morphology for N_2/CH_4 separation.

Asymmetric hollow fiber is the most desirable morphology for industrial applications due to its high flux and compact and robust nature. Efforts were made to extend the good separation performance obtained from 800 ℃ Matrimid® CMS dense film into 800 ℃ Matrimid® hollow fiber. While the 800 ℃ Matrimid® hollow fiber provided attractive N_2/CH_4 selectivity, the N_2 permeance was extremely low and is far from satisfying for industrial application. It was found that the cross-sectional asymmetry in Matrimid® hollow fiber was totally lost after pyrolysis according to SEM images. The separation layer expanded from the thin skin layer to the entire hollow fiber wall and led to a large drop in N_2 permeance. V-treatment was applied to inhibit substructure collapse during pyrolysis. SEM images revealed that the asymmetry in V-treated CMS hollow fibers was significantly enhanced compared to untreated fibers. Permeation results also showed an increase in permeance. However, due to the deposition of silica onto fiber surface during V-treatment, the intrinsic separation property of the skin layer in CMS hollow fiber was adversely affected, resulting in the decrease of N_2/CH_4 selectivity. Results showed that while 10% V-treatment was as effective to restrict substructure collapse as 100% V-treatment, the adverse effect on skin layer for the 10% V-treatment was much lower than the 100% V-treatment.

7.2 Recommendations

7.2.1 Further Detailed Study on Doping Methods

Chapter 4 discussed that O_2-doping method is expected to "clog" the ultramicropores in Matrimid® CMS membranes due to the already tight pore structure, especially when it is pyrolyzed at 800 ℃. However, it is recommended that such expectation to be verified by experiments. Oxygen levels between 1 ppm and 100 ppm with balance Ar are suggested to be applied as the pyrolysis atmosphere during the pyrolysis of Matrimid® at 550 ℃, 675 ℃, and 800 ℃. The permeation results of these CMS membranes can provide valuable insights to the capability of controlling ultramicropores for similar-sized gas pairs like N_2/CH_4 using O_2-doping method. For the H_2-doping method applied to Matrimid®, elemental analysis may not reveal much H% difference beyond experimental error for the undoped and doped samples, due to the small amount of H presence. However, ^{1}H solid-state NMR might reveal the bonding between C and H by showing peaks at different chemical shifts. While H is mostly removed at high temperature pyrolysis, low temperature H_2-doping allows H to be rebonded to C, especially at the most reactive sites of the carbon lamellae edges. The chemical shifts of NMR peaks will also be useful to indicate what type of C (either sp^2 or sp^3) and the chemical environment of C that is bonded with H in the H_2-doping method.

7.2.2 Further Study on P84® CMS Membranes

Chapter 5 showed that P84® CMS dense film pyrolyzed at 800 ℃ provided attractive and similar separation performance with 800 ℃ Matrimid® CMS dense film. The FFV and chemical structure of P84® was also shown to be similar to those of Matrimid®. It is suggested to perform permeation and sorption measurements at different temperatures to better understand the separation mechanism of this membrane. Similar analysis of energetic and entropic contributions in diffusion selectivity as applied to Matrimid® CMS dense film can be performed on P84® CMS dense film. This can provide a better comparison between the pore structures of these two CMS membranes and give insights to any possible improvement regarding the pore structure. In addition, mixed gas permeation test is suggested to be performed on P84® CMS membrane to provide better evaluation of separation performance in real case.

It is also suggested that P84® can be spun into hollow fibers and pyrolyzed at 800 ℃ to obtain P84® CMS hollow fiber membranes. With the good separation performance shown in 800 ℃ CMS dense film, P84® CMS hollow fiber is expected to be high performing. Barsema et al. showed that P84® could be spun into asymmetric hollow fibers [1] and also pyrolyzed them into CMS hollow fibers [2]. However, their P84® polymer hollow fibers were very porous and non-selective, thus it is believed that there were defects on the skin layer. Favvas et al. also pyrolyzed non-selective P84® hollow fibers at 900 ℃ and showed that N_2/CH_4 selectivity was increased from 0.8 to 2.7 after pyrolysis when tested at 100 ℃. It is believed that defects on the separation layer were partially cured during pyrolysis so the N_2/CH_4 selectivity was much improved. If defect-free P84® hollow fibers could be spun and pyrolyzed into CMS hollow fibers, high

separation performance is expected and this CMS hollow fiber would be a good alternative to Matrimid® CMS hollow fibers. Then the problem of substructure collapse during pyrolysis will also need to be investigated and efforts to avoid such collapse should be made, considering Matrimid® and P84® have similar decomposition temperatures and glass transition temperatures.

7.2.3 Relationship between Precursor and CMS Membrane Separation Performance

Chapter 5 discussed the effect of precursor on 800 ℃ CMS dense film separation performance based on 9 polymers. It was discovered that CMS membranes derived from precursors with highly open structure like 6FDA polyimides could not provide strong molecular sieving effect for N_2/CH_4 and only gave low selectivity; while CMS membranes derived from precursors with too densely packed polymer chains could not provide satisfying N_2 permeability. It is suggested to perform sorption measurements on these CMS dense films pyrolyzed from different precursors to build a correlation between precursor structure and diffusion coefficient. This can provide good insight to optimize ultramicropore structure, which provides molecular sieving function.

Apart from the FFV analysis, more characterizations like TGA-FTIR and WAXR are suggested to be performed on CMS membranes pyrolyzed from different precursors. These can provide better comparison between different precursors regarding the degradation of polymers during pyrolysis and pore structure in the resulting carbon membranes. With the guidance of FFV for precursor selection shown in Chapter 5, more

precursors with intermediate polymer chain density and without pore-forming bulky chemical groups like CF_3 can be studied for N_2/CH_4 separation.

7.2.4 Further Study on V-treatment on Matrimid® CMS Hollow Fiber

Chapter 6 discussed the V-treatment effect on restricting substructure collapse in 800 ℃ Matrimid® hollow fiber and its side effect of changing intrinsic separation property in the skin layer based on 100% and 10% VTMS treatment. Results showed that while V-treatment could form a layer of siloxane on the wall of pores in hollow fiber to inhibit polymer chain relaxation and maintain the asymmetric structure in hollow fiber, a large amount of silica was also accumulated on the hollow fiber skin. It is hypothesized that the silica can form a relatively dense structure on the CMS hollow fiber surface after pyrolysis and greatly change the intrinsic separation property. The VTMS concentration during V-treatment is suggested to be further optimized to reduce such side effect while still effectively restricting the substructure collapse. While 10% VTMS was shown to be an optimized value in V-treatment for 650 ℃ Matrimid® CMS hollow fiber [3], it might not be the best value for 800 ℃ Matrimid® CMS hollow fiber. In addition, since the silane on fiber surface might form a dense structure after pyrolysis and block pathways that were accessible to the smaller sized N_2, lower temperature pyrolyzed V-treated Matrimid® CMS hollow fiber might provide better separation performance with higher N_2/CH_4 selectivity. From the data of Bhuwania, it is calculated that the 650 ℃ Matrimid® CMS hollow fiber with 100% V-treatment provide N_2 permeance of 1.8 GPU and N_2/CH_4 selectivity of 4.5; while the 650 ℃ Matrimid® CMS hollow fiber with 10% V-treatment

provide N_2 permeance of 2.6 GPU and N_2/CH_4 selectivity of 3.3, as shown in Figure 7.1. It is suggested that by V-treating Matrimid® hollow fibers at different VTMS% and pyrolyzing the V-treated fibers at 700 ℃ and 750 ℃, higher N_2/CH_4 selectivity with a good N_2 permeance (preferably above 1 GPU) might be achieved.

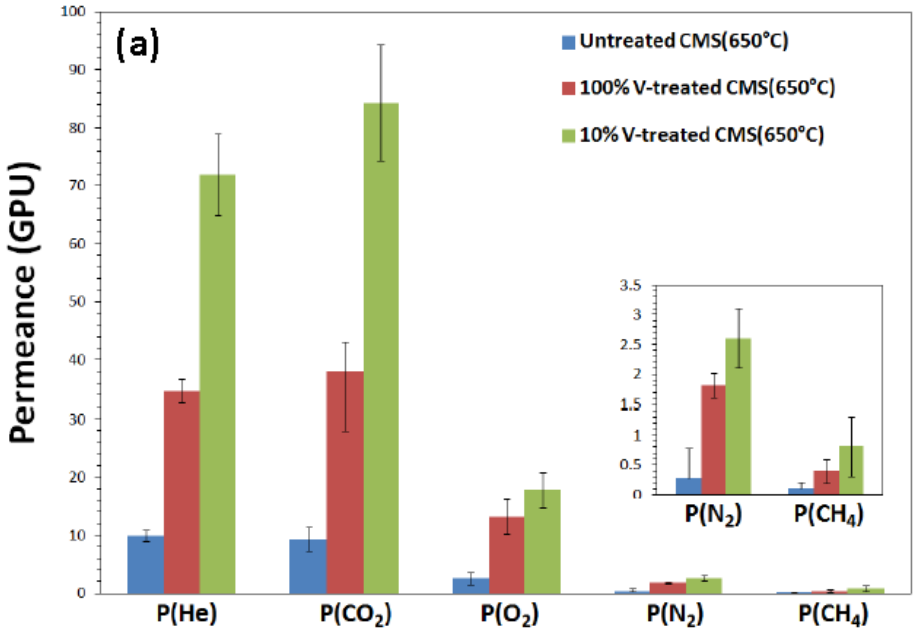

Figure 7.1: Permeance of different gas penetrants for the untreated, 10% V-treated and 100% V-treated CMS hollow fibers pyrolyzed from Matrimid® at 650 ℃ under UHP Ar, tested at 35 ℃ and 100 psia feed pressure [3].

7.2.5 Aging Stability of CMS Hollow Fibers

After CMS hollow fibers with satisfying N_2/CH_4 selectivity and N_2 permeance are achieved, one of the next concerns will be the aging stability of CMS hollow fibers. Previous study showed that physical aging exist in CMS membranes, where permeability decreases and selectivity might increase with time [4]. It was also shown that the aging in less permeable CMS hollow fibers made from more densely packed polymer precursors like Matrimid® or pyrolyzed at higher temperatures exhibited less aging problem [4]. It is hypothesized that re-alignment of carbon lamellae might be the reason of physical aging. Aging study on CMS hollow fibers can provide better evaluation of the membrane separation performance on the long term, and can also provide guidance regarding proper storage of CMS hollow fiber modules when they are not in use. The V-treatment may make the aging of CMS hollow fibers more complicated. As silica is prone to react with moisture, detailed study on V-treated CMS hollow fibers should be performed.

7.2.6 Realistic Testing and Scale up of CMS Hollow Fibers

Another concern for CMS membranes is the separation performance under realistic conditions. Results in Chapter 4 showed that 20% N_2/80% CH_4 mixed gas tests exhibited lower N_2/CH_4 selectivity and lower N_2 permeability compared to pure gas permeation due to the competition effect between N_2 and CH_4 sorption. Results in Chapter 6 showed that the separation performance of Matrimid® CMS did not change much at higher feed pressures up to 700 psia. As CMS hollow fibers can withstand much higher feed pressure and their permeation measurement is much faster than CMS dense

films, more mixed gas permeation measurements at high feed pressures should be performed on good performing CMS hollow fibers. Effects of several operational parameters including temperature, feed pressure, feed concentration, stage-cut, etc. are also important for real application. The scale-up of pyrolysis process to fabricate larger amount of CMS hollow fibers in one pyrolysis batch and realistic CMS hollow fiber module construction are all important areas for future study.

7.3 References

[1] Barsema JN, Kapantaidakis GC, Van Der Vegt NFA, Koops GH, Wessling M. Preparation and characterization of highly selective dense and hollow fiber asymmetric membranes based on btda-tdi/mdi co-polyimide. J Membr Sci 2003;216(1–2):195-205.

[2] Barsema JN, Van Der Vegt NFA, Koops GH, Wessling M. Carbon molecular sieve membranes prepared from porous fiber precursor. J Membr Sci 2002;205(1–2):239-46.

[3] Bhuwania N. Engineering the morphologhy of carbon molecular sieve (cms) hollow fiber membranes. Atlanta: Georgia Institute of Technology; 2013.

[4] Xu L. Carbon molecular sieve hollow fiber membranes for olefin/paraffin separations. Atlanta: Georgia Institute of Technology; 2012.

APPENDIX A

METAL ORGANIC COMPLEX TO IMPROVE N_2 SORPPTION

At the beginning of this project, an initial study of applying iron-phosphine complex into polymer membranes was performed to improve the sorption coefficient of N_2 and overcome the adverse effect of sorption selectivity in the N_2/CH_4 separation. This effort was inspired by a previous study where iron-phosphine complex was dissolved in a polar solvent to improve the liquid absorption of N_2 [1, 2]. It was shown that N_2 can reversibly bind to the iron-phosphine complex by forming an unstable complexing molecule. The ligand used for the metal-organic complex synthesis was diethylphosphinoethane (DEPE), which is liquid at room temperature. The chemical structure of DEPE is shown in Figure A.1. The synthesis followed previous described procedures [3, 4]. And all reactions were carried out in a 100 mL 3 neck flask.

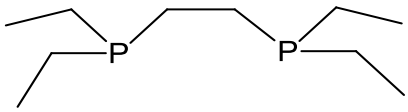

Figure A.1: Chemical structures of diethylphosphinoethane (DEPE).

DEPE in the amount of 24.2 mmol was first dissolved in 40 mL THF and reacted with 12.1 mmol of anhydrous $FeCl_2$ under stirring at room temperature to form the ferrous complex of $FeCl_2(DEPE)_2$, as shown in Figure A.2.

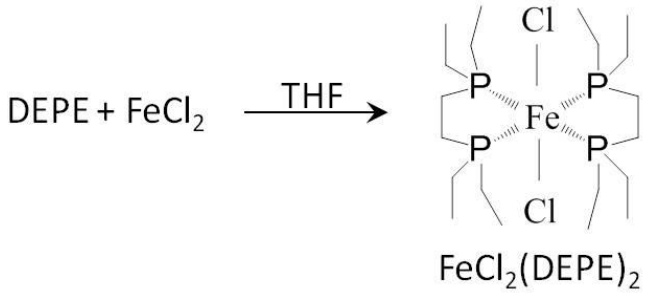

Figure A.2: Reaction of DEPE and $FeCl_2$ to form ferrous complex $FeCl_2(DEPE)_2$.

The reaction was allowed to proceed for 48 hour and a green-brownish solution was obtained. The solvent was evaporated and green microcrystalline solid was obtained. The yield was 85%. According to previous work, $FeCl_2(DEPE)_2$ can react with $LiAlH_4$ to form hydrido-complex, which can further react with N_2 to form N_2-complex [1, 4], as shown in Figure A.3.

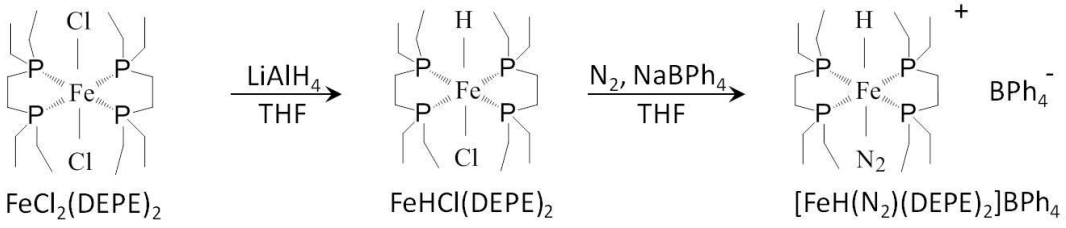

Figure A.3: Reaction of $FeCl_2(DEPE)_2$ to form hydrido-complex and N_2-complex.

The second reaction shown in Figure A.3 is the mechanism of selective N_2 absorption in liquid made of hydrido-complex and polar solvent like water. Since such an ion reaction is not available in the membrane matrix, the metal-organic complex

synthesis was stopped at $FeCl_2(DEPE)_2$ and it was dissolved in THF together with Ultem® polyimide to form a membrane dope for solution casting. It was hypothesized that the interaction between Fe and the lone pair of electrons in N_2 might improve the N_2 sorption coefficient. However, although both Ultem® and $FeCl_2(DEPE)_2$ can be dissolved in THF, initial study showed that they were not totally miscible in the membrane dope. The dope was not fully transparent and floccules were observed. The film cast from this dope was also not fully transparent and tiny particles were present in the film. As a result, only Knudsen diffusion was observed in permeation test. Another problem with this metal organic complex is that it was chemically unstable when exposed to moisture. This iron-phosphine complex changed color from green to brown within 48 hours after it is exposed to moisture in air. It is obvious that such instability is not suitable for natural gas separation, since water usually exists in raw gas. The expensive synthesis and difficulty in mixing with polymer also make the application of this metal-organic compound in membrane matrix undesirable.

References

[1] Friesen DT, Babcock WC, Edlund DJ, Lyon DK, Miller WK, inventors; Liquid absorbent solutions for separating nitrogen from natural gas patent US 6,077,457. 2000.

[2] Friesen DT, Babcock WC, Edlund DJ, Miller WK, inventors; Nitrogen sorption patent US 5,225,174. 1993.

[3] Chatt J, Hayter RG. 1079. Some hydrido-complexes of iron(ii). Journal of the Chemical Society (Resumed) 1961(0):5507-11.

[4] Bancroft GM, Mays MJ, Prater BE, Stefanini FP. Cationic hydride complexes of iron, ruthenium, and osmium, including a triad of molecular nitrogen complexes. Journal of the Chemical Society A: Inorganic, Physical, Theoretical 1970(0):2146-9.

APPENDIX B

THEORETICAL CALCULATIONS OF ENTROPIC FACTOR

As discussed in Chapter 4, according to Transition State Theory, the N_2/CH_4 entropic diffusion selectivity can be written as

$$\left(\frac{D_{N_2}}{D_{CH_4}}\right)_{entropic} = \frac{(F^{\neq}/F)_{N_2}}{(F^{\neq}/F)_{CH_4}} \tag{B.1}$$

where $F^{\neq}$ represents the partition function for the gas penetrant in the transition state as it passes through the constricted ultramicropore window, and F is the partition function for the same molecule in the normal state when it resides in the micropore cavities [1, 2]. The partition function consists of translational, rotational, and vibrational contributions, as shown below.

$$F = F_{trans} \cdot F_{rot} \cdot F_{vib} \tag{B.2}$$

So the entropic diffusion selectivity can be written as

$$\left(\frac{D_{N_2}}{D_{CH_4}}\right)_{entropic} = \left(\frac{F_{N_2,trans}^{\neq}}{F_{CH_4,trans}^{\neq}} / \frac{F_{N_2,trans}}{F_{CH_4,trans}}\right) \cdot \left(\frac{F_{N_2,rot}^{\neq}}{F_{CH_4,rot}^{\neq}} / \frac{F_{N_2,rot}}{F_{CH_4,rot}}\right) \cdot \left(\frac{F_{N_2,vib}^{\neq}}{F_{CH_4,vib}^{\neq}} / \frac{F_{N_2,vib}}{F_{CH_4,vib}}\right) \tag{B.3}$$

The calculation of partition function value changes for N_2 and CH_4 during the diffusion jump from a micropore into a 3.8 Å sized ultramicropore is presented below. The gas penetrants' initial position in micropores corresponds to the normal state, and the position in ultramicropores corresponds to the activated state. During this diffusion jump,

it is assumed that the vibration of both penetrants is unrestricted in both normal and activated state. Thus there is no change in the value of vibrational partition function from normal state to activated state, and Equation B.3 can be reduced to Equation B.4, as shown below.

$$\left(\frac{D_{N_2}}{D_{CH_4}}\right)_{entropic} = \left(\frac{F_{N_2,trans}^{\neq}}{F_{CH_4,trans}^{\neq}} / \frac{F_{N_2,trans}}{F_{CH_4,trans}}\right) \cdot \left(\frac{F_{N_2,rot}^{\neq}}{F_{CH_4,rot}^{\neq}} / \frac{F_{N_2,rot}}{F_{CH_4,rot}}\right) \quad \text{(B.4)}$$

The translational partition function can be calculated using the following equation

$$F_{trans} = \left(\frac{2\pi\ m\ k\ T}{h^2}\right)^{n/2} a^n \quad \text{(B.5)}$$

where *n* is the number of translational degree of freedom, *m* is the mass of the molecule, *k* is Boltzmann constant, *T* is temperature, *h* is Planck constant, and *a* is the length or height of the cubic cavity in which the penetrant is confined.

In the normal state, both penetrants can freely translate in x, y and z directions, as shown in Figure B.1. So the translational degree of freedom *n* is 3 for both penetrants, and the cavity length *a* for both penetrants is assumed to be 3.8 Å. It should be noted that although the exact value of cavity length *a* is dependent on the size of micropores, this value does not affect the calculation since when cavity length *a* is considered the same for both penetrants and when both penetrants have the same translational degree of freedom, the cavity length *a* will be ruled out in the $\frac{F_{N_2,trans}}{F_{CH_4,trans}}$ term in Equation B.4. A detailed calculation example for the translational partition function of N_2 in the normal state is exhibited below, using Equation B.5.

In Equation B.5., m_{N_2} is 28 times proton mass:

$$m_{N_2} = 28 \times m_H = 28 \times 1.6726 \times 10^{-27} kg = 4.683 \times 10^{-26} kg \quad \text{(B.6)}$$

The Bolzman constant *k*, temperature *T*, Planck constant *h*, cavity length *a*, and translational degree of freedom *n* are listed below.

$$k = 1.381 \times 10^{-23} m^2 kg\ s^{-2} K^{-1} \quad \text{(B.7)}$$

$$T = 35^{\circ} C = 308 K \quad \text{(B.8)}$$

$$h = 6.626 \times 10^{-34} m^2 kg\ s^{-1} \quad \text{(B.9)}$$

$$a = 3.8 \times 10^{-10} m \quad \text{(B.10)}$$

$$n = 3 \quad \text{(B.11)}$$

So the translational partition function of N_2 in the normal state is:

$$F_{N_2,trans} = \left(\frac{2\pi\ m\ k\ T}{h^2} \right)^{n/2} a^n$$

$$= \left(\frac{2\pi \times 4.683 \times 10^{-26} kg \times 1.381 \times 10^{-23} m^2 kg\ s^{-2} K^{-1} \times 308 K}{(6.626 \times 10^{-34} m^2 kg\ s^{-1})^2} \right)^{3/2} \times (3.8 \times 10^{-10} m)^3$$

$$= 8351 \quad \text{(B.12)}$$

In the activated state, the partition function $F^{\neq}$ does not contain the translational partition function in the direction of gas diffusion (x direction in Figure B.1) for either penetrant, since the factor $\frac{kT}{h}$ in Eq. (4.4) accounts for this degree of freedom [2]. The 'slimmer' N_2 has two translational degrees of freedom in the y and z directions. The cavity height *a* is considered to be 0.7 Å, which is the difference between N_2 molecule

height 3.09 Å and the pore size 3.8 Å. In contrast, CH_4 can only have one translational degree of freedom in the z direction with the same cavity length *a* when it is in Configuration 1, as shown in Figure B.1. When CH_4 is in Configuration 2, the projected height is larger and disables its translational movement in the z direction. So the translational degree of freedom is 0. Similar to the calculation example shown for N_2 in the normal state, the translational partition functions of N_2 and CH_4 in the activated state can be calculated using Equation B.5, and the values with comparison to normal state values are summarized in Table B.1. The translational contribution in the entropic diffusion selectivity in Equation B.4 is shown in Table B.2. A calculation example for the Configuration 1 of CH_4 is shown below.

$$\left(\frac{F_{N_2,trans}^{\neq}}{F_{CH_4,trans}^{\neq}} / \frac{F_{N_2,trans}}{F_{CH_4,trans}}\right) = \left(\frac{3582}{2.81} / \frac{8351}{3852}\right) = 2.13 \tag{B.13}$$

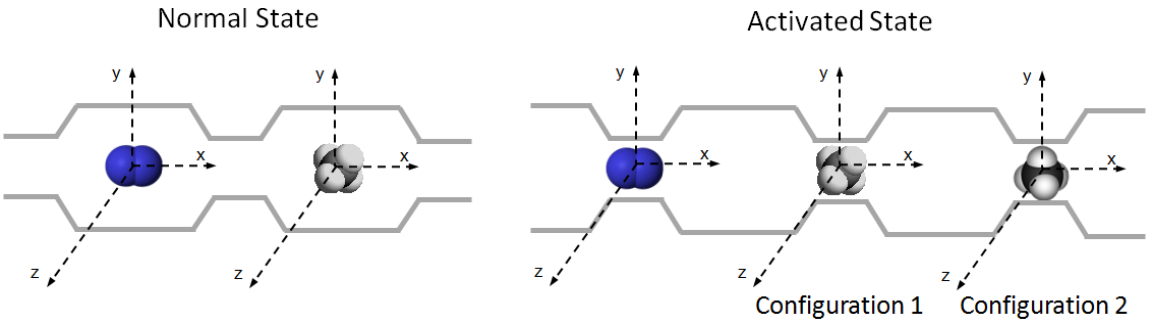

Figure B.1: Translational movement of N_2 and CH_4 in the normal and activated states.

Table B.1: Translational partition functions of N_2 and CH_4 in the normal and activated states, calculated at 35 ℃.

	N_2	CH_4	
		Configuration 1	Configuration 2
Normal state, F	8351	3582	3582
Activated sate, $F^{\neq}$	13.97	2.81	1

Table B.2: Translational contribution in the entropic diffusion selectivity, calculated at 35 ℃.

	Configuration 1	Configuration 2
$\frac{F_{N_2,trans}^{\neq}}{F_{CH_4,trans}^{\neq}} / \frac{F_{N_2,trans}}{F_{CH_4,trans}}$	2.13	5.99

The rotational partition function can be calculated using the following equations

$$\text{Diatomic: } F_{rot} = \left(\frac{T}{\sigma\ \Theta_r} \right)^{n/2} \tag{B.14}$$

$$\text{Polyatomic: } F_{rot} = \frac{\pi^{n/6}}{\sigma^{n/3}} \left(\frac{T^3}{\Theta_{rA}\ \Theta_{rB}\ \Theta_{rC}} \right)^{n/6} \tag{B.15}$$

where n is the number of rotational degree of freedom, σ is the symmetry number of the molecule, Θ_r, Θ_{rA}, Θ_{rB}, and Θ_{rC} are the characteristic rotational temperatures. The characteristic rotational temperature Θ_r is used to simplify the partition function, and is defined as below [3].

$$\Theta_r = \frac{h^2}{8\pi^2 Ik} \tag{B.16}$$

where I is the moment of inertia. The values of symmetry number σ and characteristic rotational temperatures Θ_r for N_2 and CH_4 can be found in Table 4.9.

In the normal state, N_2 can freely rotate around y and z axes, and has a full rotational degree of freedom of 2; CH_4 can freely rotate around x, y and z axes, and has a full rotational degree of freedom of 3, as shown in Figure B.2. A detailed calculation example for the rotational partition function of N_2 in the normal state is exhibited below, using Equation B.14.

$$F_{N_2,rot} = \left(\frac{T}{\sigma\ \Theta_r}\right)^{n/2} = \left(\frac{308K}{2\times 2.88}\right)^{2/2} = 53.47 \tag{B.17}$$

In the activated state, the 'slimmer' N_2 can freely rotate around the y axis, and can rotate ~90◦ around the z axis. Thus the rotational degree of freedom for N_2 in the activated state is considered to be 1 ¼. On the other hand, CH_4 can only have one translational degree of freedom around y axis in Configuration 1, which gives the minimum projected height in the ultramicropore window. In Configuration 2, since CH_4 has a larger projected height and can just get into the ultramicropore, it is believed that CH_4 cannot freely rotate around any axis and its rotational degree of freedom is 0, as shown in Figure B.2. Similar to the calculation example shown for N_2 in the normal state, the rotational partition functions of N_2 and CH_4 in the activated state can be calculated using Equation B.6 and B.7, and the values with comparison to normal state values are summarized in Table B.3. The rotational contribution in the entropic diffusion selectivity

in Equation B.4 is shown in Table B.4. A calculation example for the Configuration 1 of CH_4 is shown below.

$$\left(\frac{F_{N_2,rot}^{\neq}}{F_{CH_4,rot}^{\neq}} / \frac{F_{N_2,rot}}{F_{CH_4,rot}}\right) = \left(\frac{12.02}{3.37} / \frac{53.47}{38.56}\right) = 2.57 \tag{B.18}$$

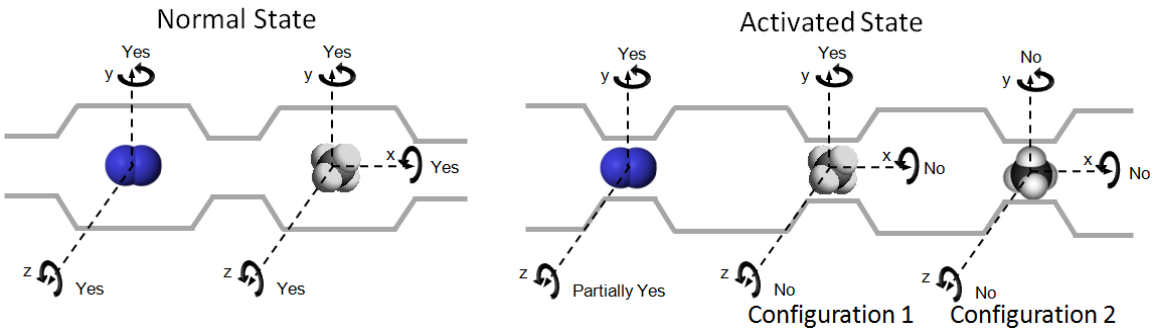

Figure B.2: Rotational movement of N_2 and CH_4 in the normal and activated states.

Table B.3: Rotational partition functions of N_2 and CH_4 in the normal and activated states, calculated at 35 ℃.

	N_2	CH_4	
		Configuration 1	Configuration 2
Normal state, F	53.47	38.56	38.56
Activated sate, $F^{\neq}$	12.02	3.37	1

Table B.4: Rotational contribution in the entropic diffusion selectivity, calculated at 35 ℃.

	Configuration 1	Configuration 2
$\frac{F_{N_2,rot}^{\neq}}{F_{CH_4,rot}^{\neq}} / \frac{F_{N_2,rot}}{F_{CH_4,rot}}$	2.57	8.68

Based on the calculated results in Table B.2 and Table B.4, the entropic diffusion selectivity can be calculated using Equation B.4, and results are shown in Table B.5. A calculation example for the Configuration 1 of CH_4 is shown below.

$$\left(\frac{D_{N_2}}{D_{CH_4}}\right)_{entropic} = \left(\frac{F_{N_2,trans}^{\neq}}{F_{CH_4,trans}^{\neq}} / \frac{F_{N_2,trans}}{F_{CH_4,trans}}\right) \cdot \left(\frac{F_{N_2,rot}^{\neq}}{F_{CH_4,rot}^{\neq}} / \frac{F_{N_2,rot}}{F_{CH_4,rot}}\right) = 2.13 \times 2.57 = 5.5 \quad \text{(B.19)}$$

Table B.5: Entropic diffusion selectivity, calculated at 35 ℃.

	Configuration 1	Configuration 2
$\left(\frac{D_{N_2}}{D_{CH_4}}\right)_{entropic}$	5.5	51.9

The above discussion for the Configuration 2 of CH_4 is based on the assumption that CH_4 cannot rotate at all in the activated state, and the entropic diffusion selectivity based on such assumption is calculated to be 51.9. If CH_4 could freely rotate around y axis and has one rotational degree of freedom in the activated state as for Configuration 1,

then the rotational contribution in the entropic diffusion selectivity would be 2.57 instead of 8.68, and the entropic diffusion selectivity would be 15.4 instead of 51.9. In the real case, CH_4 in Configuration 2 might rotate to some extent but cannot have the full rotational degree of freedom due to its large projected height relative to the ultramicropore size. The level of rotational capability of CH_4 in this configuration is complicated since it depends on not only the distribution of ultramicropore sizes but also the shape of ultramicropores. While the exact value of entropic diffusion selectivity in this configuration in the real case cannot be accurately determined, it is believed that this value should be between 51.9 and 15.4, which correspond to the rotational degrees of freedom of 0 and 1. Then, the overall entropic diffusion selectivity for CH_4 in both Configuration 1 and Configuration 2 would be in a range with lower limit of 5.5 and higher limit between 15.4 and 51.9. Our experimental results showed that the entropic diffusion selectivity in 800 ℃ Matrimid® CMS was 23.6. This indicates that the rotation of CH_4 in the activated state was significantly inhibited.

Reference

[1] Glasstone S, Laidler KJ, Eyring H. The theory of rate processes: The kinetics of chemical reactions, viscosity, diffusion and electrochemical phenomena. New York: McGraw-Hill Book Company, Incorporated; 1941.

[2] Singh A, Koros WJ. Significance of entropic selectivity for advanced gas separation membranes. Ind Eng Chem Res 1996;35(4):1231-4.

[3] Mcquarrie DA. Statistical thermodynamics. Sausalito CA: University Science Books; 1973.